The molecular origin of fast fluid transport in carbon nanotubes : theoretical and molecular dynamics study of liquid/solid friction in graphitic nanopores

Kerstin Falk

To cite this version:

Kerstin Falk. The molecular origin of fast fluid transport in carbon nanotubes : theoretical and molecular dynamics study of liquid/solid friction in graphitic nanopores. Other [cond-mat.other]. Université Claude Bernard - Lyon I; Friedrich-Alexander-Universität Erlangen-Nürnberg, 2011. English. NNT : 2011LYO10167 . tel-00755026

HAL Id: tel-00755026
https://theses.hal.science/tel-00755026

Submitted on 20 Nov 2012

N d'ordre : 167 - 2011

Université Claude Bernard Lyon I
Laboratoire de Physique de la Matière Condensée et Nanostructures
et/und
Friedrich-Alexander Universität Erlangen-Nürnberg
Lehrstuhl für Theoretische Physik I
(Cotutelle/Doppelpromotion)

The molecular origin of fast fluid transport in carbon nanotubes: theoretical and molecular dynamics study of liquid/solid friction in graphitic nanopores

---

Diplôme de Doctorat / Dissertation

Spécialité Physique / Fachrichtung Physik

présentée par / vorgelegt von

Kerstin FALK

soutenue publiquement le / mündliche Prüfung am

23-09-2011

devant la commission d'examen formée de / vor der Prüfungskommission

Monsieur Lydéric BOCQUET
Monsieur Jean-François DUFRÊCHE
Monsieur Laurent JOLY
Madame Pascale LAUNOIS
Monsieur Klaus MECKE
Monsieur Emmanuel TRIZAC

(arrêté du 7 août 2006 / arrêté du 6 janvier 2005)

Etude théorique et simulations de dynamique moléculaire du frottement liquide/solide dans des nanopores à base de graphite : rôle de la courbure dans le transport rapide des fluides à l'intérieur des nanotubes de carbone

Ce manuscrit présente une description théorique des propriétés de transport exceptionnelles des liquides dans les nanotubes de carbone (CNT pour *Carbon NanoTubes*). La perméabilité de ces canaux, qui possèdent un diamètre de quelques nanomètres, dépasse largement ce qui est prévu par les équations de l'hydrodynamique et la condition limite de non-glissement. Au cours des dernières années, plusieurs groupes ont effectué des expériences d'écoulement de l'eau et d'autres liquides dans des membranes de CNT. Ces groupes ont observé une perméabilité très supérieure (jusqu'à quatre ordres de grandeur) à l'attente classique. D'autres groupes ont conduit des simulations de dynamique moléculaire (MD pour *Molecular Dynamics*) de l'eau dans des CNT, qui ont confirmé en partie les résultats expérimentaux. Cet écoulement rapide a été attribué aux particularités de la dynamique des fluides dans les nanosystèmes. D'une part, la description hydrodynamique, qui est une théorie continue, atteint ses limites quand la taille des systèmes considérés est comparable au diamètre moléculaire (en dessous d'un nanomètre environ pour l'eau). D'autre part, lorsque le volume du système diminue, les effets de surface deviennent importants. En particulier, après une vingtaine d'années de recherche dans le domaine de la micro/nano-fluidique, il est maintenant largement accepté qu'une discontinuité de vitesse peut apparaître à l'interface entre un liquide et un solide, quantifiée par la longueur de glissement. Cependant, les longueurs de glissement nécessaires pour expliquer les débits mesurés dans les CNT sont beaucoup plus grands que celles qui ont été prédites et mesurées auparavant pour d'autres interfaces lisses. Ce glissement exceptionnel – équivalent à un frottement liquide/solide très réduit – ouvrirait la voie à des applications prometteuses, par exemple une désalinisation de l'eau plus efficace par osmose inverse. Cependant l'origine aussi bien que l'ampleur de la perméabilité accrue des CNT restaient incertains lorsque nous avons débuté ce travail.

Dans ce contexte, nous avons mené une étude exhaustive du frottement liquide/solide qui apparaît pendant l'écoulement d'un fluide dans un CNT, à l'aide de simulations de dynamique moléculaire. Une attention particulière a été portée à l'eau, étant donné son importance pour les applications envisagées. Néanmoins d'autres liquides ont été considérés (décane, éthanol, octaméthylcyclotétrasiloxane), et les points forts présentés par la suite sont essentiellement vrais pour tous ces liquides. Afin de distinguer l'influence du confinement et de la courbure, plusieurs systèmes avec des géométries différentes ont été simulés : des CNT de rayons variés, remplis ou entourés par de l'eau, ainsi que de l'eau confinée entre deux plans de graphène parallèles séparés d'une distance variable. Dans ces systèmes, le coefficient de frottement $\lambda = -F/\mathcal{A}v_{slip}$ a été mesuré en utilisant plusieurs méthodes indépendantes. Ce coefficient λ contrôle la force (par unité de surface) $F/\mathcal{A}$ subie par un fluide qui glisse avec une vitesse v_{slip} sur une paroi. Les simulations de l'eau entre deux plans de graphène ont montré que le coefficient de frottement était indépendant du confinement tant que celui-ci restait supérieur à 3-4 fois la taille d'une molécule.

Par contre, la courbure du mur a une influence considérable sur le coefficient de frottement. Celui-ci diminue avec le rayon lorsque l'eau est à l'intérieur du tube, et il augmente lorsque l'eau est à l'extérieur du tube (courbure négative). Pour des rayons supérieurs à 10 nm environ, on retrouve la même valeur de λ (tant à l'intérieur qu'à l'extérieur) que pour l'eau sur le graphène.

Ensuite, nous avons établi une expression approximative du coefficient de frottement qui le relie avec des propriétés microscopiques de l'interface entre le liquide et la paroi. Cette expression reproduit la dépendance du coefficient de frottement avec la courbure, et elle permet de l'expliquer à partir des trois paramètres statiques suivants : tout d'abord la densité de surface de l'eau, puis la rugosité de la paroi (caractérisée par l'amplitude du potentiel subit par l'eau au contact de la paroi), et finalement la commensurabilité entre la structure de la paroi et la structure de la première couche d'eau à l'interface. Par exemple, le faible frottement entre l'eau et le graphène est dû à la rugosité extrêmement faible du potentiel. Dans les CNT, les trois paramètres mentionnés ci-dessus varient avec la courbure, ce qui modifie le coefficient de frottement. Il est important de noter que le sens et l'ampleur du changement sont très spécifiques aux structures moléculaires du nanotube de carbone et de de l'eau à l'interface. En particulier, nous avons observé numériquement une influence de la chiralité du tube sur le coefficient de frottement, cohérente avec le modèle proposé.

En résumé, la combinaison de simulations de dynamique moléculaire et d'une modélisation théorique a mené à une compréhension détaillée du frottement de l'eau dans les nanotubes de carbone. Notre étude confirme le transport rapide des liquides dans ces tubes et donne une description microscopique du frottement qui explique quantitativement l'origine de sa valeur extrêmement basse.

mots clés: nanofluidique, glissement, coefficient de frottement liquide/solide, nanotube de carbone, simulations de dynamique moléculaire

Molekulardynamik-Studie zur flüssig/fest Grenzflächenreibung: Krümmungsabhängiger Ursprung schnellen Flüssigkeitstransports in Kohlenstoffnanoröhrchen

Diese Arbeit gibt eine theoretische Beschreibung der speziellen Eigenschaften des Flüssigkeitstransports in Kohlenstoffnanoröhrchen (CNT - carbon nanotube). Diese mikroskopischen Kanäle, die einen Durchmesser von wenigen Nanometern haben, sind wesentlich durchlässiger für Fluide, als man es im Rahmen der klassischen hydrodynamischen Beschreibung und unter Annahme der no-slip Randbedingung erwarten würde. Experimentelle Messungen der Permeabilität von Membranen aus CNT, die von verschiedenen Forschergruppen innerhalb der letzten Jahre durchgeführt wurden, ergaben für mehrere Flüssigkeiten – insbesondere auch für Wasser – einen Durchfluss, der bis zu vier Größenordnungen über den Erwartungen lag. Im gleichen Zeitraum führten andere Gruppen Molekulardynamik (MD) Simulationen von Wasser in CNT durch, in denen die erhöhte Durchlässigkeit der CNT bestätigt und auf die Besonderheiten der Fluiddynamik auf Nanometer-Längenskalen zurückgeführt wurden: Zum einen stößt die hydrodynamische Kontinuumsbeschreibung bei Systemgrößen, die mit einem Moleküldurchmesser vergleichbar sind (für Wasser unter einem Nanometer), auf die Grenze ihrer Gültigkeit. Zum anderen werden mit schwindendem Volumen Oberflächeneffekte dominant. Tatsächlich hat die intensive Forschung im Bereich der Mikro- und Nanofluidik in den letzten zwei Jahrzehnten ergeben, dass in manchen Systemen an der Grenzfläche zwischen Flüssigkeit und Wand eine Diskontinuität der Geschwindigkeit auftritt. Dieser Geschwindigkeitssprung wird durch die Slip-Länge charakterisiert. Um die gemessenen Flussraten zu erklären, muss man jedoch für CNT von deutlich größeren Slip-Längen ausgehen, als man es auf Grundlage des aktuellen Verständnisses erwarten würde. Dieser außergewöhnlich große Slip ist gleichbedeutend mit einer extrem kleinen Reibung zwischen der Flüssigkeit und der Wand. Ein solcher reibungsarmer Transport von Flüssigkeiten in Nanokanälen würde vielversprechende Anwendungsmöglichkeiten bieten, wie zum Beispiel eine effizientere Trinkwassergewinnung aus Salzwasser durch Umkehr-Osmose. Allerdings waren die Ursache sowie das Ausmaß der erhöhten CNT-Permeabilität zu Beginn dieser Studie weitestgehend unklar.

Vor diesem Hintergrund wurde in der vorliegenden Arbeit mittels Molekulardynamik Simulationen die Reibung untersucht, die beim laminaren Fluss eines Fluids durch ein CNT an der flüssig-fest Grenzfläche auftritt. Ziel dieser Studie war es, zunächst Parameter zu identifizieren, die diese Reibung beeinflussen, und dann mittels einer theoretischen Modellierung zu einem quantitativen Verständnis zu gelangen. Auf Grund seiner besonderen Bedeutung für potentielle Anwendungen von CNT-Membranen, wurde das Hauptaugenmerk zunächst auf Wasser gelegt. Zusätzlich wurde jedoch auch das Fließ-Verhalten von Decan, Ethanol und Octamethylcyclotetrasiloxan (OMCTS) untersucht, und die folgenden Erläuterungen für Wasser gelten im Wesentlichen auch für die anderen Flüssigkeiten. Um den Einfluss der räumlichen Beschränkung (Confinement) und der Wandkrümmung unabhängig voneinander untersuchen zu können, wurden verschiedene Geometrien betrachtet: Wassergefüllte CNT und von Wasser umgebene CNT sowie Wasser in einem Spalt zwischen zwei parallelen Graphen-Platten. In diesen Systemen wurde mit mehreren Methoden der Reibungskoeffizient $\lambda = -F/\mathcal{A}v_{slip}$ gemessen, der angibt welche Reibkraft (pro Flächeneinheit) $F/\mathcal{A}$ auf ein Fluid wirkt, das mit einer Geschwindigkeit v_{slip} über eine feste Wand gleitet. Die Messungen ergaben, dass der Reibungskoeffizienten unabhängig vom Confinement ist, solange der Kanal-Querschnitt nicht unter weniger als etwa 3-4 Moleküldurchmesser fällt. Die Wandkrümmung hat dagegen einen erheblichen Einfluss auf die Reibkraft: Der Reibungskoeffizient ist für Wasser an der CNT-Innenseite für kleinere CNT-Radien (größere Krümmung) kleiner und umgekehrt für Wasser an der CNT-Außenseite (negative Krümmung) größer. Für große CNT-Radien über ca. 10 nm, findet man innen und außen den gleichen Wert für den Reibungskoeffizienten wie an einer ebenen Graphen-Wand.

Im weiteren Verlauf der Arbeit wurde analytisch ein näherungsweiser Ausdruck für den Reibungskoeffizienten hergeleitet, der die Reibung mit mikroskopischen Eigenschaften der Grenzschicht verknüpft. Dieser Ausdruck gibt die Krümmungsabhängigkeit des Reibungskoeffizienten qualitativ wieder und ermöglicht es, sie durch eine Variation der folgenden drei statischen Größen zu erklären: Erstens die Oberflächendichte des Wassers, zweitens die Rauigkeit der Wand, quantifiziert durch die Amplitude des lateralen Wasser-Wand Potentials, und drittens das Verhältnis zwischen der Wand- und der Wasserstruktur an der Grenzfläche. Die geringe Reibung von Wasser auf Graphen ist demnach auf die glatte Beschaffenheit der Graphen-Oberfläche zurückzuführen. In CNT ändern sich die drei oben genannten Größen auf Grund der Krümmung, wobei die molekulare Struktur sowohl des Kohlenstoffnanoröhrchens als auch der Wasser-Grenzschicht eine entscheidende Rolle für das Ausmaß und die Richtung der Veränderung spielen: In den MD Simulationen wurde ein Unterschied zwischen den Reibungskoeffizienten für CNT verschiedener Chiralität ('armchair' und 'zigzag') nachgewiesen, der mit dem Model konsistent ist.

Alles in allem führte die Kombination aus MD Simulationen und theoretischer Modellierung zu einem detaillierten Verständnis der Wasser-CNT Reibung. Diese Arbeit bestätigt die Existenz eines schnellen, nahezu reibungslosen Flüssigkeitstransports in Kohlenstoffnanoröhrchen. Desweiteren konnte die mikroskopische Ursache der geringen Reibung ermittelt und quantitativ beschrieben werden.

Schlüsselwörter: Nanofluidik, Slip, Kohlenstoffnanoröhrchen, Reibungskoeffizient flüssig/fest, Molekulardynamiksimulation

Acknowledgements

I would like to thank my supervisors L. Bocquet, L. Joly and K. Mecke for offering me the possibility to work on this project and for their extensive support during this work. Many thanks for the time you invested on scientific discussions, as well as on administrative tasks, in particular the organization of the co-supervision agreement, and also for the financial support that facilitated not only this co-supervision but also my participation at several schools and conferences.

Further, I would like to thank F. Sedlmeier for carrying out the GROMACS simulations, B. Mantisi for providing the silica glass configurations, and the whole IT service groupe of the LPMCN, especially R. Mascart, for IT-support.

Sincere thanks are also given to W. Mickel, S. Kapfer, B. Geraud, H. Lastakowski, I. Theurkauff and to all other people in both groups that directly or indirectly contributed to this work by helpful discussions or by providing a pleasant and welcoming atmosphere.

Last but not least, I thank my familly for their continuous support.

Introduction

Nanofluidics deals with the behavior of fluids in systems with nanometric sizes [90, 8]. At such scales fluid properties may be expected to strongly depart from what the frameworks of continuum approaches –*e.g.* hydrodynamics – would predict, therefore allowing to bypass their limitations and open a broad range of novel perspectives. In this context recent experimental works have put forward the potentially exceptional properties of carbon nanotube membranes in terms of water transport [38, 67, 110]. These membranes, made of a macroscopic collection of hollow aligned carbon nanotubes (CNT) [43] with diameters as less as 2 nm, were claimed to exhibit water flow up to four orders of magnitude faster than predicted by the hydrodynamic framework. This furthermore echoes the reported 'soft dynamics' of water measured by inelastic neutron scattering in single wall CNT with 1.4 nm diameter [53]. The reported fast water transport has raised great hopes to develop membranes with both high selectivity and high flux – reaching the efficiency of biological pores such as aquaporins [91] –, with application for ultra-filtration or energy conversion [72, 82, 76].

However up to now these results remain unexplained and their interpretation is controversial within state-of-the-art understanding [98]. Indeed, while low friction of water has been predicted and measured experimentally at hydrophobic surfaces [7, 8], the performances reached by the CNT membranes are *orders of magnitude* above the results measured up to now for 'usual' (chemically modified) interfaces. This can be quantified in terms of the so-called *slip length* b measuring the liquid-solid friction: while b is on the order of tens of nanometers for water on hydrophobic surfaces [8], the corresponding slip length for the CNT membranes would reach *microns* [38], *i.e.* far above usual expectations for slippage of water on hydrophobic surfaces. Furthermore, from the theoretical side, a number of works have specifically explored fluid flows in CNT using molecular dynamics simulations [1, 29, 34, 41, 48, 89, 98, 99]. However numerical estimates of the slip lengths for water, extracted from velocity profiles, remain rather scattered, and depend on the molecular model used for water, so that no systematic conclusion or clear-cut interpretation could be drawn to explain the experimental results [98]. As an alternative explanation, one could also invoke the breakdown of continuum hydrodynamics at such scales as the origin of low friction, as is expected for single-file water transport in CNT [5, 41, 99]. However the experimental results for CNT membranes in references [38, 67, 110], were obtained for tubes with diameters above one nanometer, in which deviations to continuum hydrodynamics are *a priori* expected to be minimal [8, 99]. The physical mechanisms at the origin of the reported fast flows thus remains fully open within the state-of-the-art understanding of slippage, leaving uncertain the potential applications at stake.

Our aim of this work is therefore to assess on theoretical grounds the properties of CNT membranes for water transport and to give a general framework for the specific water transport in CNT that either allows to convincingly refute or to explain the previously reported experimental results.

To this end, we carried out a systematic exploration of the liquid/solid friction of water as well as other liquids in various nanometric graphitic systems, using both molecular dynamics simulations and theoretical analysis. Altogether, our results do indeed confirm that CNT act as fast water transporters, pointing to an unforeseen mechanism at the origin of the ultra low water-carbon friction.

The manuscript at hand gives a detailed description of this work, starting in part I with a short introduction to the field of nanofluidics, followed by a recapitulation of the work on water flow through CNT that has been performed so far by others. Part II describes the molecular dynamic simulations that we performed to check up on the high experimental flow rates. Thereafter, the theoretical analysis leading to an understanding of the water/graphite friction on a molecular level, is presented in part III. The last section of this part is dedicated to complementary MD simulations that were performed to check the accuracy of this understanding. Finally, in part IV the range of applicability of our results is broadened by studying other liquids than water.

Contents

I Framework (literature) 9

1 Fluid flow at the nanoscale 11
- 1.1 Introduction to 'nanofluidics' 11
- 1.2 Confinement effects and breakdown of hydrodynamic theory 12
- 1.3 Liquid/solid boundary condition at the micro- and nanoscale 13

2 Fluid flow in carbon nanotube membranes 18
- 2.1 Molecular dynamics simulation studies of fluid dynamics in carbon nanotubes 19
- 2.2 Experimental measurements of carbon nanopore membrane permeability 24
- 2.3 Discussion of open questions and formulation of the aim of the presented study 29

II Molecular dynamics simulation study of water in confined graphitic systems 31

3 MD simulation of water/graphite systems 33
- 3.1 Introduction and motivation to use molecular dynamics simulation 33
- 3.2 Empirical potentials to model water 35
- 3.3 Confined water in graphitic systems 36
- 3.4 Summary: Interaction potentials employed in the study at hand 37

4 Equilibrium and flow measurement of water/graphite friction 39
- 4.1 Measuring the friction coefficient - a new approach to determine the liquid/solid boundary condition 39
- 4.2 Geometry of the considered systems 40
- 4.3 Equilibration process (temperature and pressure control) 42
- 4.4 Flow measurement of the friction coefficient 43
- 4.5 Equilibrium measurement of the friction coefficient 45
- 4.6 Discussion of results: Curvature dependent friction 46
- 4.7 Testing the robustness of the main outcome 47

5 Comparison to literature: Linking friction, slip, shear viscosity and diffusion 50
- 5.1 Further studies of water confined in the graphene slab geometry: viscosity and diffusion 50
- 5.2 Comparison to other groups' results 53

6 Incompatibility with the common slip models 56
- 6.1 Normal pressure 56
- 6.2 Wetting behavior: depletion and contact angle 58
- 6.3 Interface water structure 59

6.4 Conclusion 62

III Theoretical understanding of the curvature dependent friction coefficient 63

7 Approximative expression for the friction coefficient 65
7.1 Distinction of 'static' and 'dynamic' part in the Green-Kubo expression 65
7.2 Approximating the random mean squared force 65

8 Comparison of theory and simulations 70
8.1 Static origin of the curvature dependent friction (validation of the theory) 70
8.2 Microscopic origin of the curvature dependence: understanding friction on a molecular level 71

9 Testing predictions 75
9.1 Changing wall structure without curvature - variations of the graphene lattice parameter 75
9.2 Changing the carbon nanotube structure - zigzag chirality 77
9.3 Non-linear behavior for large slip velocities 83

10 Quantitative agreement between the rms force and its approximation 84
10.1 Neglect of second water layer 84
10.2 Truncation of the force field Fourier expansion 84
10.3 Projection of the first water layer 86

IV Investigation of other liquid/solid combinations 89

11 Introduction and motivation 91

12 Water flow in a silica pore 93
12.1 System setup 93
12.2 Equilibrium measurement of the friction 94
12.3 Poiseuille flow simulation to determine the slip length 95

13 Fast fluid flow in CNT - other liquids 97
13.1 Model parameters: molecule geometries and interaction potentials . . 97
13.2 Considered systems and their equilibrium density profiles 99
13.3 Liquid/graphite friction for larger molecules 102
13.4 Summary and outlook 109

Conclusion and Outlook 111

Appendix 115

A Structure factor of a one dimensional bead-spring chain 115

B Lateral force field for different oxygen-to-wall distances 116

C Geometry and dihedral potential for ethanol and decane 117

D Contributions to rms force for OMCTS, decane, ethanol 118

Bibliography 119

List of Figures

1 Microscopic view of slip length . . . 14
2 Slip length vs. contact angle . . . 17
3 Osmotic transport of water through sub-nanometer CNT . . . 19
4 CNT membrane . . . 26
5 Carbon nanopipe membrane . . . 28
6 TIP3P and SPCE water molecule . . . 36
7 System geometries . . . 41
8 System equilibration with reservoirs . . . 42
9 Example for plug flow profiles . . . 43
10 Friction force vs. slip velocity . . . 44
11 Integrated force autocorrelation function . . . 45
12 Friction coefficient vs. confinement . . . 46
13 Square tube . . . 47
14 Friction coefficient vs. confinement for SPC-E water model . . . 49
15 Couette flow geometry . . . 51
16 Viscosity, slip length and friction coefficient in graphene slab geometry 52
17 Pressure independence of friction coefficient . . . 57
18 Radial density profile and potential for water in CNT . . . 57
19 Depletion length for water in CNT and graphene slab . . . 59
20 Coordinates first water layer . . . 60
21 Bead-spring model of single file water . . . 60
22 Static structure factor of the water interface layer . . . 61
23 Static rms force and decorrelation time vs. confinement . . . 66
24 Friction coefficient vs. static rms force . . . 66
25 Potential energy landscape for the interface water layer . . . 68
26 Static rms force and its theoretical approximation . . . 71
27 Contributions to the rms force in armchair CNT (low confinement) . 72
28 Radius dependent interaction energy landscape for the first water layer 73
29 Radius dependence of the q-vector . . . 73
30 Contributions to the rms force in armchair CNT (all radii) . . . 74
31 Water density profile for different graphene lattice spacings . . . 76
32 Snapshot of water in zigzag CNT . . . 77
33 Friction coefficient vs. confinement (for armchair and zigzag CNT) . 78
34 Friction coefficient vs. rms force for zigzag CNT . . . 78
35 Friction coefficient vs. theoretical rms force for all geometries . . . 80
36 Contributions to the rms force in zigzag CNT (low confinement) . . . 82
37 Fourier transform of the force field . . . 85
38 Radial dependence of the force field roughness . . . 86
39 Integrated force autocorrelation for water in silica tube . . . 94
40 Poiseuille flow profile of water in silica tube . . . 95
41 Sketch of decane and ethanol molecule . . . 97
42 Sketch of OMCTS molecule . . . 98
43 Density profiles for decane, ethanol, OMCTS in low confinement . . 100

44 Friction coefficient vs. confinement (for decane, ethanol, OMCTS) . 103
45 Friction coefficient, rms force and its approximation for decane, ethanol and OMCTS 105
46 Structure factor decane 108
47 Force field for water molecule in proximity of an armchair CNT . . . 116
48 Dihedral angle 117
49 Geometry decane and ethanol molecule 117
50 Contributions to rms force for OMCTS, decane, ethanol 118

Part I

Framework (literature)

In this first part, we lay the groundwork for the later discussion of our investigation of liquid flow through graphitic nanopores, and at the same time, set our studies into context of active research.

To begin with, a short introduction to nanofluidics is given in section 1. We highlight some characteristics of fluid flow at the nanoscale, which open promising perspectives for various nanotechnological applications and thus give an idea why an important effort is currently taken in the research community to progress in this field. As part of this introduction, we put a large focus on the effect of liquid/solid slip, which is an important factor concerning small-scale fluid dynamics. The question which fluid or solid surface properties determine the amount of slip is still under debate. Nevertheless, some key points about slippage that are now mostly agreed upon, are presented. In short, for liquid flow over flat and atomically smooth surfaces, slip was found to be directly related to the wetting properties: Wetting systems are thought to be accurately described by the no-slip boundary condition, while for very non-wetting situations, the slip length can attain tenth of nanometers. This view is supported by experimental and numerical results as well as by theoretical considerations. However, not all investigations of liquid/solid slip are in accordance with these findings. Especially the case of carbon nanotubes has attracted lots of attention: Although water in CNT was found to form a low contact angle [28], numerous studies of water flow through CNT suggest much larger slip length than they were found for other – even for highly non-wetting – materials. The reasons for this large slippage are so far obscure. This lack of clarity motivates us to undertake a detailed investigation of water flow through CNT; a motivation which is further backed up by the new technological applications in view. The second section is thus dedicated to the presentation of the most-noticed experimental and numerical studies of liquid flow through CNT, whose results present the starting point for our work.

Contents

1 Fluid flow at the nanoscale **11**

1.1 Introduction to ’nanofluidics’ 11

1.2 Confinement effects and breakdown of hydrodynamic theory 12

1.3 Liquid/solid boundary condition at the micro- and nanoscale . . . 13

1.3.1 Navier slip boundary condition and its consequences on fluid flow 13

1.3.2 Current knowledge about slippage - microscopic pictures and macroscopic parameters to explain liquid/solid slip . . 13

1.3.3 Theoretical prediction for intrinsic slip 15

2 Fluid flow in carbon nanotube membranes **18**

2.1 Molecular dynamics simulation studies of fluid dynamics in carbon nanotubes 19

2.1.1 Breakdown of hydrodynamic theory and frictionless flow of single file water in sub-nanometer carbon nanotubes 19

2.1.2 First indications for fast continuum liquid flow in carbon nanotubes: rapid decane imbibition 20

2.1.3 Water flow enhancement: low friction leading to plug flow . 21

2.1.4 Curvature dependent flow enhancement 22

2.1.5 Comparative summary of molecular dynamics simulation results 23

2.2 Experimental measurements of carbon nanopore membrane permeability 24

2.2.1 Outperforming permeability of 7 nm-carbon nanotube membranes 24

2.2.2 Large flow enhancement for 2 nm carbon nanotube membranes 27

2.2.3 Important flow enhancement for 44 nm carbon nanopipe array 27

2.2.4 Summary and comparison to the simulation outcomes . . . 28

2.3 Discussion of open questions and formulation of the aim of the presented study 29

1 Fluid flow at the nanoscale - more than just smaller

1.1 Introduction to 'nanofluidics'

The concept of 'Nanofluidics' as its own research area developed only in the last years, by downsizing further and further the scales at which fluid transport can be studied [8, 20, 90]. Advances in this evolving field are closely related to progress in nanotechnology – the design and development of devices to observe and manipulate objects at the nanoscale. Moreover, it is also directly connected to the increasing computational power that is available, since numerical studies of multi-particle systems, e.g. molecular dynamics simulations, have evolved as a complementary way to study small-scale systems. In both areas, remarkable progress has been made over the last decades [20].

Motivation to strive for ever smaller realizations of fluid technology arise from different fields: It includes, for example, biochemistry, with the aim to develop highly sensitive analytic techniques to isolate and study individual macromolecules [96], or bio-medicine technology, striving for precision drug delivery [95]. Conceptually, these applications require first of all a down-scaling of fluid devices (channels, pumps, filters, mixers, etc.). From this point of view, nanofluidics is just a logical extension of microfluidics, pushing down the size of the investigated systems. According to the predictions from the classical hydrodynamics framework, however, along with the miniaturization of fluid devices come great problems concerning efficiency: We consider a simple liquid that is pushed through a cylindrical pipe with radius R by an external force, e.g. a pressure gradient. For large radii, the flow dynamics are accurately described by the Navier-Stokes equation and a boundary condition of zero velocity at the wall. The solution is the parabolic Poiseuille flow profile $v_{\text{no-slip}}(r) = \frac{1}{4\eta}(R^2 - r^2)(-\partial_z P)$, and the volumetric flow rate is $Q_{\text{no-slip}} = \frac{\pi}{8\eta} R^4(-\partial_z P)$. Comparing now, for example, two membranes with identical flow area, but different pore sizes, we find that the pressure that is needed to achieve the same flow rate depends quadratically on the inverse ratio of the pore radii. In other words, for a 10 times smaller radius, the pressure has to be 100 times higher [1].

Then again, performances of biological nanopores strongly challenge these theoretical limitations: The trans-membrane protein aquaporine-1, for example, which serves as a water filtering channel in many biological processes, is at once highly selective in blocking all types of ions, and still extremely permeable for water. Concretely, the permeability of aquaporine pores, which have an effective diameter of $\sim 0.4\,\text{nm}$, was found to be three orders of magnitude larger than the permeability of a cylindrical channel of equivalent size as predicted from the Navier-Stokes equations [74, 91, 111]. These findings suggest that expectations which are based on classical hydrodynamics not necessarily hold true on the nanoscale. Actually, this observation does not come as a surprise, since continuum descriptions, like hydrodynamics, are expected to break down if the key assumption – scale-separation between typical

---

[1] Consider two membranes $i = 1, 2$ with n_i pores of radius R_i; flow area = total cross section $A_i = n_i R_i^2 \pi$; flow rate $Q_i \propto n_i R_i^4 \Delta P_i$. For $A_1 = A_2$ and $Q_1 = Q_2$ we find $\frac{\Delta P_1}{\Delta P_2} = \left(\frac{R_2}{R_1}\right)^2$.

time- and length scales of the macroscopic fluid flow and the underlying molecular dynamics – fails. It is at this point where novel aspects come to play that distinguish 'nano' from 'micro'. Fluid transport at the smallest scales follows unforeseen principles, as the incredible efficiency of functional bio-molecules as channels, filters, etc., demonstrates. Specific nanofluidic phenomena offer thus new promising possibilities, if they could be exploited for technological applications, like water desalination [72] or energy conversion [82, 76]. These perspectives present a great motivation to continue the path towards fabrication of nanoscale fluid devices and to work on the fundamental understanding of fluid dynamics on these scales.

1.2 Confinement effects and breakdown of hydrodynamic theory

The classical hydrodynamics framework is based on a continuum view of fluid media. Originally, it was developed to predict fluid behavior at 'human' length- and timescales that are orders of magnitude larger than the characteristic length- and timescales defined by the particle interactions. This approach is overlooking the atomic nature of matter, hiding the complexity of a 10^{23}-particle system in a few phenomenological coefficients, like viscosity, compressibility, etc. One can thus not expect hydrodynamic equations to hold true for systems where characteristic length- and timescales are comparable to those of the underlying molecular dynamics. Still, predictions from hydrodynamics have been found to be accurate for surprisingly small systems. For simple liquids, the expected breakdown of continuum theory occurs only when the liquid is confined to systems as small as $1\,\mathrm{nm}$ [14, 26, 18].

However, stating the validity of hydrodynamic theory is not equivalent to claiming, that the finite system size does not have any influence on fluid dynamics in restricted geometries. These confinement effects are reflected in deviations of the mentioned transport coefficients from their respective bulk values. It is thus worth emphasizing, that in the case of water, the viscosity also seems to keep its bulk value all over the range of applicability of hydrodynamic theory [40, 60, 81]. That this is generally not the case, can be seen on the example of the diffusion coefficient. Under confinement, the bulk Stokes-Einstein relation between viscosity and diffusion $D = k_\mathrm{B}T/(3\pi\eta a)$ (a particle diameter) is not exact; Diffusion depends not only on the fluid viscosity, but also on the system size and geometry. To give an idea, corrections due to confinement are expected to be on the order of the particle size over the channel width. Furthermore, diffusion in a confined system is also sensitive to the boundary conditions at the interface [85]. The last point leads directly to the second type of finite-size effects: The smaller the system, the larger is the ratio of interface region to bulk region and the more important are the interface properties for the overall systems behavior. If we are interested in fluid flow through a channel, this concerns the boundary condition for the velocity field at the solid wall. In fact, with increasing performance of micro-technological apparatus and computational power, it became apparent that the macroscopic no-slip boundary condition does not hold true for all interfaces. Instead, a difference between the tangential components of the wall and the fluid velocities at the interface can occur: the fluid 'slips' over the surface.

1.3 Liquid/solid boundary condition at the micro- and nanoscale

In the following, we introduce the Navier slip boundary condition which is commonly used to describe the phenomenon of slippage. Afterwards, the up-to-date knowledge about slippage will be outlined. The focus will thereby lie on ’intrinsic’ slip at the molecular scale – a velocity discontinuity at a two-phase interface, where the liquid and the solid are in direct contact. Based on this discussion, we can then formulate an expectation for the systems we are interested in, namely water/graphite interfaces.

1.3.1 Navier slip boundary condition and its consequences on fluid flow

The effect of slippage is usually quantified with the slip length b. This length denotes the distance from the interface to the point where the linearly extrapolated velocity profile reaches the wall velocity; see Fig. 1(a). The boundary condition for the velocity field reads accordingly

$$b\,\partial_n v_t = v_{\text{slip}} \tag{1}$$

Although the concept of slip boundary condition already exists as long as the Navier-Stokes equations themselves, the phenomenon only started to be intensively investigated in the last two decades. The reason for this can easily be understood from a look at the solution for the above example of driven fluid flow through a cylindrical tube *with* the slip boundary condition. The resulting velocity profile is shifted with respect to the no-slip case $v(r) = v_{\text{no-slip}} + \frac{Rb}{2\eta}(-\partial_z P)$, and the flow rate becomes

$$Q = \frac{\pi}{8\eta} R^4 \left(1 + 4\frac{b}{R}\right)(-\partial_z P). \tag{2}$$

Slippage has no perceivable influence, when the slip length is small compared to the system size $b \ll R$, as it is certainly the case for macroscopic systems, thereby justifying the use of the no-slip boundary condition. If both the system size and the slip length would be of comparable magnitude, on the other side, slippage becomes of paramount importance, and would indeed allow to overcome some of the limitations for small-scale fluid devices that were discussed above. So how big is the slip length for realistic liquid/solid interfaces? This question was subject to debate for about the last ten years [8, 107]. The state of affairs in this controversy is summarized in the following.

1.3.2 Current knowledge about slippage - microscopic pictures and macroscopic parameters to explain liquid/solid slip

Experimental results for the slip length of simple liquids range from ’no slip’ to over one micron [8, 56, 107]. These results were obtained for a multitude of different systems with various interface properties (for a list of the considered liquid/surface combinations and applied measurement techniques see for example [12]). A division in three categories was proposed for the systems which were found to feature slip [107]. These categories distinguish themselves in the microscopic image of the

Definition of slip length

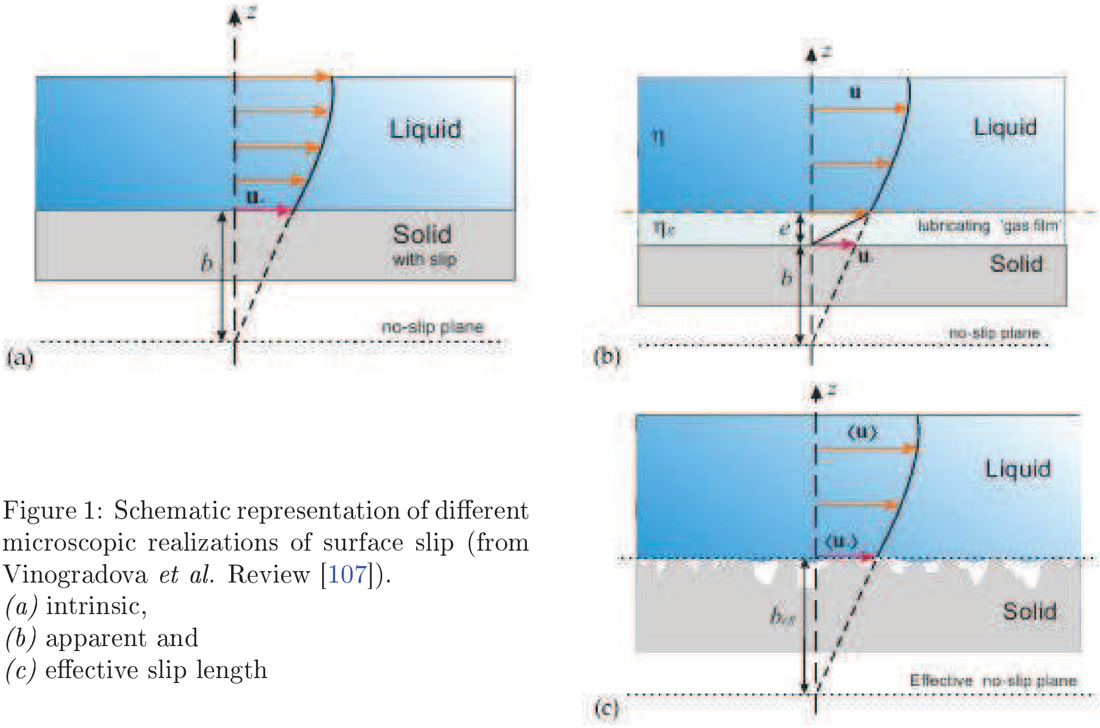

Figure 1: Schematic representation of different microscopic realizations of surface slip (from Vinogradova *et al.* Review [107]).
(a) intrinsic,
(b) apparent and
(c) effective slip length

interface area as sketched in Fig. 1: The first case represents 'intrinsic slip', where the liquid molecules in contact with the wall really have a non-zero mean velocity – they slip over the surface. The second case is so-called 'apparent slip': The flow velocity in the bulk region is enhanced in accordance with a slip boundary condition. But close to the wall, the fluid velocity actually deviates from the macroscopic profile and decreases to zero in a small zone of reduced density (depletion zone). The depictions of both, intrinsic and apparent slip, assume atomically smooth surfaces. Contrariwise, 'effective slip' is observed on rough surfaces, where the liquid is only partially in contact with the solid structure. The latter case includes so-called superhydrophobic surfaces – nano- or micro-structured hydrophobic surfaces that can lead to huge slippage [47, 58]. This phenomenon is responsible for the high end of the measured slip length in the micrometer range, and it is therefore very promising in view of possible flow enhancement. Still, we only mention this interesting effect for the sake of completeness when talking about slippage. In the following, the discussion will be restricted to atomically smooth surfaces, since this is the case for the graphite-based nanopores that will be in the focus later on.

For these smooth surfaces, it is agreed upon that wetting properties are a crucial control parameter for the slip length [8, 12, 107]. Generally speaking, liquids wetting a surface are expected to stick to the wall, while non-wetting situations were found to result in slip lengths of tenth of nanometers. This findings were also confirmed in molecular dynamics simulation studies [3, 40]. More precisely, Huang *et al.* showed, that a dependence $b \propto (1 + \cos\theta)^{-2}$ between slip length b and contact angle θ

reproduces well simulation results for water on different hydrophobic surfaces (Fig. 2). This relation comes out from a rough theoretical estimate of the slip length, which will be introduced below.

Before that, continuing to focus on the liquid/wall interaction, we mention that the same authors also successfully related the slip length to the depletion length δ as $b \propto \delta^4$. The depletion length is defined as $\delta = \int_{-\infty}^{\infty} \mathrm{d}z \left(1 - \rho^{\mathrm{s}}(z)/\rho^{\mathrm{s}}_{\mathrm{bulk}} - \rho^{\mathrm{l}}(z)/\rho^{\mathrm{l}}_{\mathrm{bulk}}\right)$ with the liquid and solid densities $\rho^{\mathrm{l,s}}(z)$ and their bulk values $\rho^{\mathrm{l,s}}_{\mathrm{bulk}}$. It is a measure for the width of the depletion layer, a zone of reduced density at the interface. Thinking of slip as a consequence of an interface depletion zone is reminiscent of the image of apparent slip. The scaling with the forth power of δ, however, is in disagreement with an alternative estimate usually applied to the apparent slip picture. It is based on the following idea: Gas that is dissolved in the liquid under normal conditions, accumulates at the interface under confinement, and builds an "air cushion" that reduces the friction with the wall. Assuming a gas layer of thickness δ (gas viscosity η^g) is sandwiched between the solid surface and the liquid bulk (viscosity η^l), the apparent slip length is expected to depend linearly on the gas layer thickness: $b = \delta\left(\eta^l/\eta^g - 1\right)$ [19, 106, 107]. The main difference between the depletion zone of a one-component and the gas layer in a two-component fluid lies in the thickness of the interface layer. The typical thickness of a depletion layer is about one molecular diameter. This is too small to reasonably define a 'gas' viscosity for the interface region and therefore the 'apparent slip' picture fails to describe the dependence of the slip length on the depletion length.

Finally, as a last parameter that was found to influence slip, we mention the hydrostatic pressure. In MD simulations with simple Lennard-Jones liquids on non-wetting surfaces, slip was found to increase for decreasing pressure [2].

1.3.3 Theoretical prediction for intrinsic slip

While the slip length gives a clear geometric image of slippage (Fig. 1), its physical meaning in terms of system properties remains somewhat obscure without further clarifications. For this, it is instructive to consider the acting forces at the interface: At the one hand, for a Newtonian liquid the tangential stress on a plane solid wall is $\sigma_t = \eta \partial_n v_t$ according to the Navier-Stokes equation, where t, n denote the directions tangential and normal to the surface. On the other hand, assuming a linear response, the wall (area $\mathcal{A}$) exerts a friction force on the liquid that is proportional to the slip velocity

$$F = -\mathcal{A}\,\lambda\, v_{\mathrm{slip}} \tag{3}$$

Linearity has been found for shear rates that are accessible in experiments [16]. In a stationary state, the two forces balance each other, which leads to the expression $\frac{\eta}{\lambda}\partial_n v_t = v_{\mathrm{slip}}$ for the slip velocity. Comparing this to the slip boundary condition Eq. (1) reveals that the slip length is in fact the quotient of fluid viscosity and the friction coefficient:

$$b = \frac{\eta}{\lambda} \tag{4}$$

A large slip length b is thus equivalent to low interface friction. The friction coefficient λ, in turn, can be expressed via linear response theory in terms of a Green-Kubo relationship, relating λ to a correlation function of a fluctuating microscopic variable at equilibrium [6]:

$$\lambda = \frac{1}{\mathcal{A}k_{\mathrm{B}}T}\int_0^{\infty}\langle F(t)F(0)\rangle_{\mathrm{equ}}\;\mathrm{d}t \tag{5}$$

where $F(t)$ is the total tangential force acting on the surface with area $\mathcal{A}$ and the average runs over equilibrium configurations. An approximation of this expression leads to the following expression for the slip length (see [2, 7] for a derivation):

$$b = \frac{\eta}{\lambda} \approx \frac{\eta k_{\mathrm{B}}TD}{S(q_{||})C_{\perp}\rho\sigma\epsilon^2} \tag{6}$$

According to this estimation, the slip length scales linearly with the product ηD (D an effective diffusion coefficient), and inversely with the molecular size σ, and the square of a typical fluid-solid interaction energy ϵ. Furthermore, $C_{\perp}$ is a geometric factor that accounts for roughness effects (large $C_{\perp}$ corresponds to a large atomic roughness[2]) and $S(q_{||})$ which is the static structure factor of the liquid, evaluated at a characteristic wave vector of the solid surface, measures the commensurability of liquid and solid structure. The dependance of the slip length on ϵ^{-2} reflects the observed influence of the wetting properties: With the interaction energy being related to the contact angle as $\epsilon \propto 1+\cos\theta$ [83, 86] [3] the scaling $b \propto (1+\cos\theta)^{-2}$ is recovered.

It is in no small part due to this success to theoretically link both effects, that hydrophobicity seems now generally thought to be a precondition for intrinsic slip. In other words, one assumes the no-slip boundary condition to hold true for wetting surfaces. However, some results persistently escape this picture . One exception that has attracted lots of attention are carbon nanotubes (CNT). It was shown that CNT can be filled with water, and that water droplets inside CNT form a wetting contact angle [28]. Based on the demonstrated relation between contact angle and slippage, one logically assumes a no-slip situation for water flow through CNT. Contrary to this expectation, the work of several people suggests a different behavior: CNT, which are already known to have outstanding mechanical and electrical properties [101], exhibit an exceptional ability for fast fluid transport. In fact, the outcome of experimental flow measurements through CNT membranes implies not only the existence of slip, but slip length of $> 10^2$ nm and even up to 50 μm [38, 67, 110] – far above what one expects even for very hydrophobic materials. These results are partly backed by predictions from MD simulations [34, 41, 48, 89, 98]. These studies will be presented in the following.

---

[2] In this context 'roughness' refers to the surface corrugation due to the atomic structure of the solid, depending on the atom size and lattice form; not to confuse with the 'roughness' of super-hydrophobic surfaces that are structured on a much larger scale.

[3] This relation results from a combination of Young's equation $\cos\theta = \frac{\gamma_{\mathrm{sv}}-\gamma_{\mathrm{ls}}}{\gamma_{\mathrm{lv}}}$ with the Laplace estimate of the interface tension as the work that is necessary to separate a liquid and a solid slab $H = \gamma_{\mathrm{sv}} + \gamma_{\mathrm{lv}} - \gamma_{\mathrm{ls}}$, where H is proportional to the interaction energy ϵ_{ls} between a liquid and a solid [107] particle.

Slip length and contact angle

Huang *et al.*, *PRL* **2008**, 101

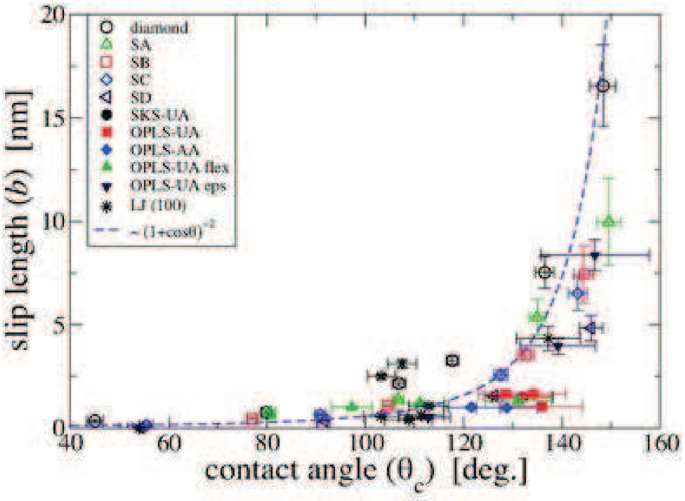

Bocquet and Charlaix, *Chem.Soc.Rev.* **2008** 39 (Review)

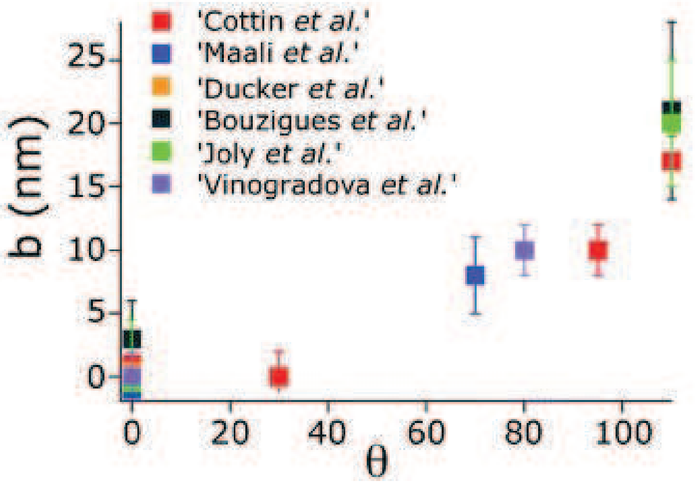

Figure 2: Slip length b of water on various smooth surfaces in dependence of the contact angle θ. *Top*: Results from Molecular Dynamics simulations by Huang *et al.* [40]. The dashed line is a theoretical fit scaling like $b \propto (1 + \cos\theta)^{-2}$. *Bottom*: Compilation of various experimental results (see Review [8] for details)

2 Pushing the limits - fluid flow in carbon nanotube membranes

This section contains a synthesis of experimental and numerical work predicting ultra-fast liquid flow through carbon nanotube (CNT) membranes. The main focus will lie on a handful of numerical and three major experimental studies whose results are the starting point for our investigations. Molecular dynamics (MD) simulations performed by Hummer *et al.* [41, 49] constitute such a cornerstone for the development of the scientific interest in the emerging field of nanofluidics. Their study of osmotically driven water flow through CNT membranes suggests that the high water permeability of biological pores can be reproduced with CNT of sub-nanometer size. In fact, they observed flow rates comparable to the ones measured for the trans-membrane protein aquaporine-1 [111, 91]. Since then, the prospect to engineer nanofluidic devices that work with the efficiency of biological systems, motivates further research on fluid flow through CNT membranes. In particular, it also initiated several groups to measure experimentally the permeability of graphitic nanopore membranes. This chronological order is the reason why, first, we start with discussing numerical studies, which are without exception using the means of MD simulations [41, 49, 54, 34, 48, 98, 99]. In parallel to the numerical studies, other groups seized the challenging task to measure flow rates through CNT membranes experimentally [38, 67, 110]. The discussion of these experiments will follow in the next subsection. At this point, we just want to mention that the existing experimental results have been quantitatively discussed in the nanofluidic community in terms of the so called enhancement factor. This factor is the ratio of measured to expected flow rate, where the expectation is based on the validity of the hydrodynamic equations and the no-slip boundary condition. If the fluid flow is correctly described by assuming a slip boundary condition, the enhancement factor for a cylindrical pore geometry reads

$$\frac{Q}{Q_{\text{no-slip}}} = \frac{\eta_{\text{bulk}}}{\eta}\left(1 + 4\frac{b}{R}\right) \tag{7}$$

with η_{bulk} and η the bulk water viscosity and the effective viscosity in the confined system, respectively. This focus on a macroscopic variable – the flux – is a direct consequence of the difficulty to handle real objects of nanometric size. Experimental techniques did not yet allow to investigate fluid flow through a single CNT. Control of the CNT radius and structure (chirality, defects, ...) is limited. Visualizing flow profiles inside a CNT with well-defined properties is infeasible with state-of-the-art technology. In simulations, however, a direct observation of the flow geometry is possible and most studies performed by means of MD simulations focus on this task. Still, in order to compare experimental and numerical results, the latter are also discussed in view of the flow enhancement factor as it is defined above. A comparative summary shows that results of the various investigations disagree to a large extend. This directly leads to the motivation for and the aim of the work that is presented in this manuscript, and which will be outlined in 2.3.

Kalra *et al.*, *PNAS* **2003**, 100 ©by the National Academy of Sciences

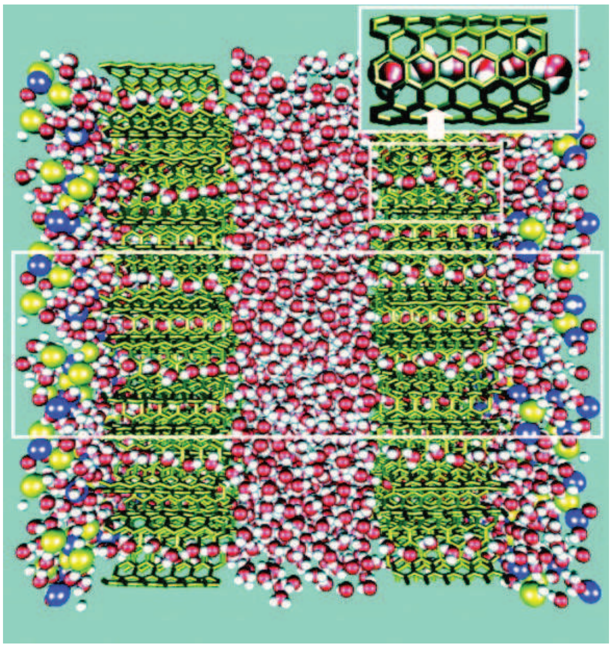

Figure 3: Snapshot of the simulation system studied by Hummer *et al.*. The pure-water compartment at the center is separated from the salt-solution compartments (left and right) by two water-permeable membranes of hexagonally packed CNT (blue, Na+; yellow, Cl-; red, oxygen; white, hydrogen). Periodic boundary conditions are applied in all three directions. The periodically replicated simulation box is indicated as a white rectangle in the middle. *Inset*: Enlarged image of a carbon nanotube filled with a hydrogen-bonded water wire.

2.1 Molecular dynamics simulation studies of fluid dynamics in carbon nanotubes

In the following paragraphs, we present a number of MD simulations of fluids in CNT which have been carried out in the last decade. Both liquid and gas transport have been investigated, though the discussion will be limited to liquids, and more precisely mostly to water. Even with this restriction, we certainly can not include all work that has been done on the subject, but we will focus on some contributions, that have attracted our attention.

2.1.1 Breakdown of hydrodynamic theory and frictionless flow of single file water in sub-nanometer carbon nanotubes

The system Hummer *et al.* investigated [49] contained two CNT membranes that separated different water compartments: The region between both membranes is initially filled with pure water, the two outside reservoirs contain salt solutions (NaCl). The membranes are built of parallelly aligned (6,6) armchair CNT with diameter 0.81 nm that are hexagonally stacked. This membrane is semipermeable; The hydrated Na^+ and Cl^- ions are confined to the outside regions. Individual water molecules, however, can enter the CNT (but not the space between CNT) and pass through the membrane to a neighboring compartment. CNT were found to be filled with water molecules arranged in single file.

The osmotic pressure leads to a net flux of water from the pure water to the salt solution reservoirs, draining the pure water compartment in the process. The amount of flux was stated to be quantitatively in agreement with measurements on the biological water channel aquaporine and it is thus much larger than what could be expected from continuous hydrodynamic theory for a cylindrical tube with the given dimensions. Furthermore, the flux was found to be independent of the CNT length, which implies that the water molecules move quasi without friction in the tube. The limiting factor for the amount of water flow is not the water dynamics *in* the pores, but the entrance and exit events of single water molecules at the open tube *ends*. The entering of a molecule in a tube is highly correlated with the exit of another one at the other side; both events come along with a collective motion of the whole water chain in the CNT. Although the net flux is directed towards the salt solution compartments, back-flow against the osmotic gradient also occurs. Hummer *et al.* state that water flow through sub-nanometer pores is not governed by the macroscopic hydrodynamic equations, but is a stochastic process driven by thermal fluctuations. They show that the characteristics of this single file water transport can be explained with a one dimensional continuous time random walk model. In this model, the flux is a sum of discrete hopping events, happening after exponentially distributed waiting times. A hopping event can be either in backward or forward direction and the possibilities p and $q = 1 - p$ are linked to the difference in chemical potential between the compartments via $p/q = \exp(-\beta\Delta\mu)$.

2.1.2 First indications for fast continuum liquid flow in carbon nanotubes: rapid decane imbibition

The investigation of flow in CNT was not limited to water. Alongside to Hummer, Quirke *et al.* performed steady state Poiseuille flow simulations of simple Lennard-Jones fluids, e.g. methane, in graphene slits [88] and in armchair CNT [89]. The slit size was about 7 nm (distance between the carbon positions of two parallel graphene sheets) and CNT diameters varied between $1-3$ nm. The fluid-solid interactions were also of Lennard-Jones type and the interaction strength was varied to investigate several different wetting situations. Interactions between the sp2 hybridized carbon atoms from the same graphene sheet or CNT, were modeled with a realistic many-body bond-order potential that has been found to accurately reproduce graphene structure and dynamics (Tersoff-Brenner, [97, 11]). Fluid flow was imposed by a constant acceleration, and after equilibration, both the methane shear viscosity and the slip length [4] were extracted from the parabolic velocity profiles. We want to emphasize two interesting points emerging from this study: First, slip length are

---

[4] Quirke *et al.* use another less common definition of slip length, namely 'the distance from the wall at the point where the *extrapolated* streaming velocity vanishes'. This length (lets call it l) is only equal to the slip length b as defined in Eq. (1) when the velocity profile is linear. For Poiseuille flow it can be readily converted according to $b = \left((R+l)^2 - R^2\right)/2R$.

$20-50\,\mathrm{nm}$, which is surprisingly large, given the fact that methane wets the graphene surface and slippage has so far been assumed to be zero for wetting systems. The occurrence of this large slip is attributed by Quirke *et al.* to the smoothness of the liquid-wall potential. This view is supported by comparative simulations with high wall corrugation, that result indeed in zero slippage. The second point concerns the modeling of the wall dynamics and to what extend it influences the fluid flow. Comparing simulations of systems with realistically modeled walls (CNT as well as graphene) and with rigid walls, it was found that fixing the carbon positions leads to lower flow velocities. The amount of the decrease is $10-20\%$. This finding justifies to a certain extend the usage of rigid walls in following studies (by this and other groups).

Later on, investigation of decane imbibition in graphitic nanopores (graphene slab and armchair CNT with diameter $0.58-2.62\,\mathrm{nm}$) showed again characteristics of low liquid-solid friction [93]: a CNT in contact with a decane reservoir was imbibed very rapidly – filling speed was of the order of $10^2-10^3\,\frac{\mathrm{m}}{\mathrm{s}}$ – and the time evolution of the penetration length does not comply with the Lucas-Washburn law [63, 108] as expected for a contact angle 180°. Instead, the imbibition velocity is constant over the probed times (~ 1 ns). Furthermore, the filling speed depends crucially on the tube radius, with a difference of one order of magnitude between the smallest and the largest CNT radius considered.

2.1.3 Water flow enhancement: low friction leading to plug flow

Following the intriguing predictions for single-file water flow in sub-nanometric CNT and oil imbibition in larger CNT, several studies of water in CNT with larger radii were conducted by different groups, in order to investigate the water/CNT boundary condition. Kassinos *et al.* reported on slip of the order of $10\,\mathrm{nm}$ for tube radii about $2-6\,\mathrm{nm}$ [50, 54]. They further suggested a curvature dependence in claiming that slip increases with the tube diameter. However, these statements were based on the alternative definition for the slip length that was also used by Quirke *et al.* (Footnote on page 20): the distance l from the wall where the extrapolated velocity profile vanishes $v(R+l)=0$. Transforming their results according to the proper definition of slip length gives $b\sim 50\,\mathrm{nm}$ for all radii. Hanasaki and Nakatani performed pressure driven flow simulations in CNT with radii between $0.8-3\,\mathrm{nm}$ and found that for flow velocities on the order of 100 m/s, velocity profiles are flat, not parabolic [34]. No values for the slip length or the flow rate are given. But, since plug flow occurs in the limit of disappearing liquid/wall friction, which means diverging slip length, slip has to be much larger than the tube radius $b\gg R\sim 1\,\mathrm{nm}$. Joseph and Aluru found the same plug-like velocity profile for gravity driven water flow in CNT with diameter $2.17\,\mathrm{nm}$ at a flow velocity of 200 m/s [48]. They measured a flow rate over 2000 times larger than the hydrodynamic no-slip expectation. At this point, we have to mention a subtlety concerning the calculation of the available flow area (tube cross section): The flux entering Eq. (7) for the enhancement factor, is calculated from the theoretical Poiseuille flow profile by integration over the tube's cross section, where the tube radius R is taken to be equal to the position of the carbon atoms. However, this overestimates the available flow area, since the repulsive water/wall interaction limits the water molecules' positions to radii smaller $\sim R - \sigma$. To take this into account, a reduced radius is sometimes used to calculate the flux. While for large radii $R \gg \sigma$, the difference is negligible, it can produce big changes for small CNT diameter. Such a reduced radius was used in [48], resulting in an enhancement factor > 2000 for a tube diameter $R = 2.17\,\mathrm{nm}$, while a calculation with the CNT radius gives an enhancement of only ~ 460. The reduced area is actually more realistic, since it has been shown, that for a typical wetting case without slip, the hydrodynamic position of the boundary – that means the location where the velocity profile becomes zero – is about one σ away from the atomic position of the boundary 'inside' the liquid [3].

2.1.4 Curvature dependent flow enhancement

Studies performed by Thomas and McGaughey investigate systematically the influence of CNT curvature on slippage. To this aim, they simulated pressure driven water flow through armchair CNT with infinite length and diameters between 1.5 and 5 nm [98]. The pressure gradient was tuned to give mean flow velocities $< 15\,\frac{\mathrm{m}}{\mathrm{s}}$ which is much lower than in the studies presented just before. Still, Thomas and McGaughey were able to identify a parabolic velocity profile in agreement with the macroscopic Navier-Stokes equations and slip boundary condition. However, the measured flow could not be explained with one and the same value for b for all CNT radii. They report on an increase of the slip length with smaller radii, accompanied by a decrease of the water viscosity. The predicted values range from 30 nm for slippage on a flat graphene sheet to about 110 nm in a CNT with diameter 1.66 nm, and from 0.80 to 0.66 mPa s for the viscosity in the same systems. The slip length was extracted from the velocity profile with a parabolic fit function. This requires large statistics, because as it was discussed just above, the extremely low fluid/wall friction leads to very flat velocity profiles, and the signal-to-noise ratio is large due to thermal fluctuations. To reduce the uncertainty, McGaughey *et al.* measured independently the water self-diffusion in order to determine $k_{\mathrm{B}}T/(3\pi a D)$ with a an estimated water molecule diameter. This quantity was then introduced into the velocity function as the viscosity η, which limits the number of fit parameters for the velocity profile to only one, namely the slip length b. It should be noted at this point, that this approach is insofar problematic as the Stokes-Einstein relation $\eta = k_{\mathrm{B}}T/(3\pi a D)$ is only valid for bulk water. In pores of finite size, the relation of viscosity and diffusion coefficient is modified by the confinement. In particular, the boundary condition at the confining walls – e.g. the slip length – enters into this relation [85]. That is why some caution concerning the quantitative significance of the values for the slip length is advisable. Nevertheless, the curvature dependence of the slip length that McGaughey *et al.* observed is very interesting and adds to the open questions about water/CNT friction.

In a subsequent publication, the same authors present results for water flow through CNT with diameter 1.66 nm down to 0.83, with finite length and connected to water reservoirs at both open ends [99]. The authors report on a transition to sub-continuum transport, where the water flow can not be explained anymore with hydrodynamic equations. This transition – interpreted as breakdown of the continuum description – coincidences with the appearance of ordered water structures. For the narrowest CNT, the confined water molecules arrange in ordered structures [100]. Depending on the tube radius, the water throughput was found to be $2-3$ orders of magnitudes higher than expected for a continuous model without slippage. We note that the appearance of strong deviations from hydrodynamic theory at confinements under 1 nm is in agreement with a scaling argument by Bocquet and Charlaix [8] comparing the system size to a typical 'viscous' length scale associated with the stress-stress decorrelation time.

2.1.5 Comparative summary of molecular dynamics simulation results

Before discussing experimental work, we want to sum up the presented results for fluid transport in graphitic nanopores obtained by molecular dynamics simulations from various groups during the last ten years. We note that they all agree upon the fact that these nanopores, like CNT for example, exhibit special properties allowing for extremely large throughput. Fluid flow through CNT is governed by very low interface friction, characterized by large slip length that lead to flat, almost plug-like velocity profiles. For CNT diameter around $\sim 1\,\mathrm{nm}$, confinement effects lead to a transition to a sub-continuum regime, where the hydrodynamic description fails to describe fluid flow. In all cases, considerable higher flow rates were observed than expected from the hydrodynamic no-slip description. To quantitatively compare the measured augmented flow rates, we look at the enhancement factor $Q/Q_{\text{no-slip}}$ (Eq. (7)), summarized in Tab. 1. Since most authors use the full radius to calculate the enhancement, we give all results according to this definition for better comparability. Still, even when the different definitions are properly taken into account, no coherent image for the amount of flow enhancement emerges. For tube diameter $\sim 2.7\,\mathrm{nm}$, outcomes for the enhancement factor vary between 40 and 500. In case of sub-continuum transport, the flow enhancement is even more impressive, up to over 1000. Furthermore, Kassinos *et al.* found a constant slip length for different CNT radii, in contrary to Thomas *et al.*, who report on increasing slippage for smaller CNT diameter.

A probable cause for discrepancies are the different potential energy functions that have been used to model the particle-particle interactions. In fact, the applied combinations of water model and water/wall interaction are different for every group, whose work was just presented. But the choice of the liquid/solid interaction strength, that also determines the wetting properties, is supposed to be crucial for the interface friction. A more elaborate discussion of water models and the water/graphite interaction, is deferred to section 3.2.

Finally, while the thermodynamic properties of the studied systems are comparable (hydrostatic pressure and temperature were always kept at 1 bar or 1 atm and 298 or 300 K, respectively [5]), geometries are somewhat different. In particular, some flow rate measurements were performed in infinitely long tubes (periodic boundary conditions), while others looked at tubes with finite length, usually connecting two

---

[5] with the possible exception of references [50, 54] where the systems are not equilibrated at well-defined pressure

water reservoirs. In the second case, dynamics at the tube openings may play a big role for the permeability, making it difficult to compare results with flow in closed tubes.

2.2 Experimental measurements of carbon nanopore membrane permeability

Having discussed the predictions for water flow in CNT obtained by means of MD simulations, we now turn to the corresponding experiments. Of course, investigating setups with one single CNT of well controlled diameter would be the ultimate goal in order to directly compare reality, simulations and theory on a fundamental level. However, this purpose requires a degree of precision in the control of nanoscopic objects that has not been reached so far. The three experimental setups that have been realized, used membranes of a multitude of parallel aligned cylindrical pores: First, in 2005, Majumder *et al.* performed flow measurements for a variety of liquids through a carbon nanotube membrane made of aligned multiwalled CNT with 7 nm inner diameter [67]. In the following year, 2006, Holt *et al.* presented studies of water and gas permeability of membranes made of double walled CNT with inner diameters less than 2 nm [38]. Finally, in 2008, Whitby *et al.* measured water, decane and ethanol flow rates through membranes perforated by 44 nm wide nanopipes, made of an amorphous carbon structure deposited inside alumina templates [110]. All three groups report on considerable flow enhancements that, in some cases, are stated to reach magnitudes up to 10^4.

The biggest challenge in these experiments lies in the production and characterization of the membrane. Pores should be straight and fully open with a constant inner diameter along the whole length. Gaps between the individual pores have to be filled since liquid is supposed to pass the membrane only inside the CNT or carbon pipes. Pore diameters, pore density and membrane thickness have to be determined accurately to calculate the flux and flow enhancement. The mentioned groups tackled this problem in different ways, leading to the investigation of different types of carbon channels. In the following, all three experiment will be shortly presented, so that afterwards the results can be compared with each other and the before mentioned simulations.

2.2.1 Outperforming permeability of 7 nm-carbon nanotube membranes

The membrane fabricated by Majumder *et al.* was an array of aligned multi walled CNT with inner diameter of ~ 7 nm, embedded in polystyrene [67]. The production of this membrane consisted of several steps [37]. First, CNT are grown by catalytic chemical vapor deposition (CVD) to a dense array of aligned CNT on a quartz substrate. The inner tube diameter can be tuned by the size of the catalyst particles. In the second step, the surface of CNT tips is spin-coated with a polystyrene-toluene solution. Polystyrene, which exhibits a highly wetting behavior on CNT, was then sucked into the space between the tubes. After drying in vacuum, the polystyrene-CNT film was removed from the substrate by etching . Finally, the CNT were uncapped with plasma oxidation. In two independent ways (by transmission electron

Compilation of water flow measurements in carbon nanopores...

...MD simulation

water model	O-C interaction	CNT diameter (nm)	slip length (nm)	flow enhancement	reference
TIP3P	AMBER	0.81^*	sub-continuum flow		[41, 49]
SPC-E	Werder[109]	2.71 4.07 5.42	56 55 57	(84) (55) (43)	[54]
SPC-E	?	0.81 to 2.71	plug flow		[34]
SPC-E	?	2.17	(249)	460	[48]
TIP5P	Werder[109]	1.66 2.22 2.77 3.33 3.88 4.44 4.99	105 70 40 37 29 31 30	433 193 106 82 53 49 47	[98]
		0.83^* 0.96^* 1.10^* 1.39^*	sub-continuum flow	$O(10^3)$ $O(10^3)$ $O(10^2)$ $O(10^2)$	[99]

Table 1: Results from MD simulation studies of water flow through carbon nanotubes that have been performed by different authors during the last 10 years. The water flux is quantified by enhancement factor (see Eq. (7)) and slip length (Eq. (1)). Tubes with starred (*) diameter have finite length, in all other cases, periodic boundary conditions have been applied; (?) quantity not specified by the authors; values given in brackets () were not specifically given in the references and are calculated assuming water keeps its bulk viscosity.

...and experiment

pore type (diameter)	slip length (nm)			flow enhancement (nm)			reference
	water	decane	ethanol	water	decane	ethanol	
CNT ($\sim 7\,\text{nm}$)	53728	3448	28124	61404	3941	32143	[67]
CNT ($< 2\,\text{nm}$)	560 to 8400	-	-	140 to 1400	-	-	[38]
nanopipe (44 nm)	35 ± 3	41 ± 2	29 ± 2	34 ± 3	45 ± 2	25 ± 2	[110]

Table 2: Experimental results for flow measurements of water, ethanol and decane through carbon nanopores with diameter $< 50\,\text{nm}$.

Holt *et al.*, *Science* **2006**, 312. Reprinted with permission from AAAS

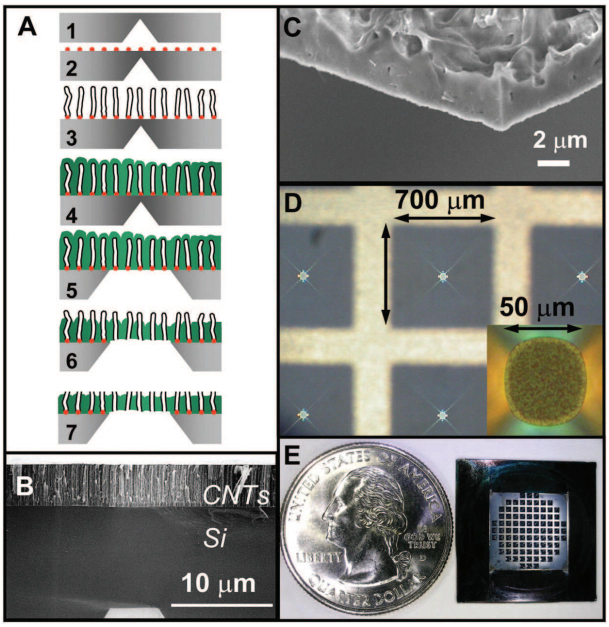

Figure 4: (A) Schematic of the fabrication process. Step 1: micro scale pit formation (by KOH etching). Step 2: catalyst deposition/annealing. Step 3: nanotube growth. Step 4: gap filling with low-pressure chemical vapor–deposited Si_3N_4. Step 5: membrane area definition (by XeF_2 isotropic Si etching). Step 6: silicon nitride etch to expose nanotubes and remove catalyst nanoparticles (by Ar ion milling); the membrane is still impermeable at this step. Step 7: nanotube uncapping (reactive ion etching); the membrane begins to exhibit gas permeability at this step. (B) SEM cross section of the as-grown CNTs. (C) SEM cross section of the membrane, illustrating the excellent gap filling by silicon nitride. (D) Photograph of the open membrane areas; inset shows a close-up of one membrane. (E) Photograph of the membrane chip that contains 89 open windows; each window is 50 μm in diameter.

microscopy (TEM) and by N_2 desorption measurement) the Inner tube diameters were confirmed to lie between $6-10$ nm with a mean value 7.5 nm. The pore density was estimated from ion diffusion measurements using the Knudsen diffusion model [51].

Majumder *et al.* performed flow measurements with water, alcohols (ethanol and iso-propanol) and hydrocarbons (hexane and decane). Their results suggest a permeability of the described membrane that is 3 to 4 orders of magnitude above the continuum no-slip expectation for all considered liquids. The slip length that have been calculated from the flux reach tenth of micrometers, with decane on the lower end with ~ 3 μm and water on the upper end with $40-70$ μm.

2.2.2 Large flow enhancement for 2 nm carbon nanotube membranes

Holt *et al.* carried out water and gas flow measurements through membranes made of double walled CNT with diameters between 1.3 and 2.0 nm [38]. As shown in Fig. 4, the membrane was again produced in multiple steps, following the same basic ideas as just described above. CNT are grown by catalytic CVD, this time on a silicon substrate and with smaller catalyst particles. In the following, the gaps between the tubes had to be filled. For this, the authors use low-pressure CVD of silicon nitride (Si_3Ni_4) that readily encapsulates the CNT. Afterwards, the excess silicon nitride is removed by ion milling to re-expose the still closed CNT ends. The same technique is used to remove the substrate on the other side, but only in a small pre-defined area, which leaves a supporting base that reduces the risk of damaging the membrane. After this step, the membrane was found to be still impermeable, proving that the silicon nitride matrix effectively closes the space outside the tubes and no micro-cracks occurred afterwards. In a final step the CNT tips were removed by reactive ion etching to open the membrane pores.

The tubes inner diameter were determined with size exclusion measurements: Test particles with 1.3 nm size were found to pass the membrane, but larger sized gold colloids (2 nm) were blocked. Further evidence for CNT diameters of 1.3 to 2.0 nm was found by transmission electron microscopy (TEM). In addition, the number of pores per area was found from the TEM images. The authors point out that this estimation of the pore density presents the largest uncertainty for the calculation of the flux. They further state that the flow enhancement factors that are reported in the following, are lower boundary estimates.

Holt *et al.* measured water flow through the described membranes and obtained flow rates that are three orders of magnitude higher than the hydrodynamic continuum expectation. This corresponds to slip length of several hundred nanometers. For comparison, the same measurement was performed with a commercial polycarbonate membrane with pore size 15 nm, resulting in an enhancement factor of less than 4 and slip length ~ 5 nm.

2.2.3 Important flow enhancement for 44 nm carbon nanopipe array

The latest experiment concerning water flow through nanometric graphitic pores was realized by Whitby *et al.* [110] with carbon membranes that were slightly different from the CNT membranes used by the other groups. Instead of growing first a CNT array and embedding the tubes subsequently in a surrounding matrix, they first produced an anodic aluminum oxide template and then used CVD to built up a carbon layer on the surface of the existing pores. The templates consisted of hexagonally ordered pores of 62 ± 4 nm diameter. The carbon nanopipes grown inside these pores had a diameter of 43 ± 3 nm, which is considerably larger than the CNT diameters investigated by Majumder *et al.* (7 nm) and Holt *et al.* (< 2 nm). Apart from the size, the nanopipes differ from carbon nanotubes by the structure: While CNT are built of atomically smooth sheets of hexagonally arranged carbon atoms, the carbon layer building the nanopipe wall has an amorphous structure. Advantages of the nanopipe membrane are, firstly, the well-characterized geometry which allows

Whitby *et al.*, *Nano Lett.* **2008**, 8. Reprinted with permission from American Chemical Society

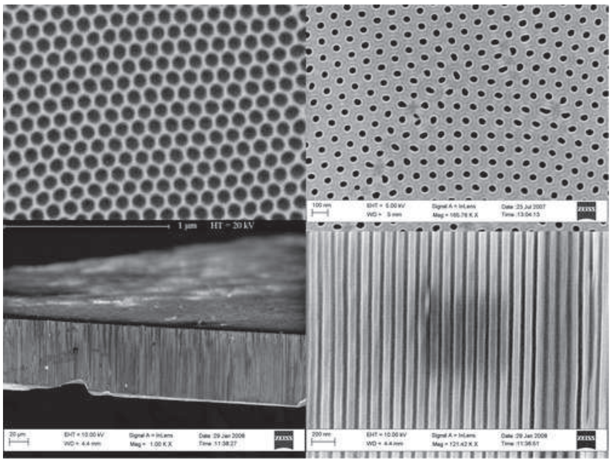

Figure 5: Figure 1. SEM images showing (a; top left) surface of porous alumina template prior to CVD treatment; (b; top right) template after CVD now covered in a layer of amorphous carbon which has reduced the diameter of the pores; (c; bottom left) cross section through snapped membrane; (d; bottom right) higher magnification view of cross section revealing the well-aligned and highly regular carbon nanopipe array.

to control the pore diameter and density – and therefore the available flow area – with higher accuracy than for the rather randomly growing CNT. Secondly, the fabrication process ensures that the carbon channels are the only cavities permeating the membrane since the aluminum oxide template effectively fills the space between nanopipes (compare Fig. 5).

Slip length and enhancement factor for water flow through these carbon nanopipes, are reported to be 35 ± 3 nm and 34 ± 3, respectively. In addition Whitby *et al.* investigated the decane and ethanol permeability, and found similar values for slippage and flow enhancement. Results for decane were higher, and for ethanol lower than for water, but deviations were less than 30%.

2.2.4 Summary and comparison to the simulation outcomes

Comparing results of the different experimental studies, we basically come to the same conclusion as at the end of the last part, where the numerical results have been discussed: All groups agree that fluid transport through carbon nano channels exceeds continuum hydrodynamic no-slip expectations considerably. However, the indicated magnitudes of this flow enhancement, which are gathered in Tab. 2, are scattered over three orders of magnitude. We also detect qualitative inconsistencies. While Majumder *et al.* found the 7 nm-MWCNT membrane to be 15 times more permeable for water than for decane, Whitby *et al.* report comparable flux through the 44 nm-nanopipe membrane for both liquids, with a slightly higher value for decane. Furthermore, as for the MD simulations, the experimental results from different groups do not give a clear trend concerning an eventual curvature dependence of flow enhancement and slip length. Slip length reach from tenth of nanometers for the 44 nm-nanopipes, to tenth of micrometers for the 7 nm-MWCNT, with results for the 2 nm-DWCNT in between. It could be speculated that some of the disagreement might be attributed to the different properties of the carbon pores (double walled vs. multi walled CNT and amorphous nanopipe vs. well-ordered CNT), or the diverse surface treatments in the membrane production that might lead to different chemical composition of the CNT ends which would influence the membrane permeability.

In short, both experiments and simulations present evidence for exceptionally rapid fluid transport in carbon nano channels. However, due to the existing quantitative and qualitative differences of the various studies' results, the extent of the flow enhancement remains unclear. Alternative explanations for the augmented throughput in experiments have been proposed: Insufficient control of the experimental setup, like the presence of an electric field as a supplementary external driving force, the presence of leaks, or a miscalculation of the pore density [98, 105]. A juxtaposition of numerical and experimental values does not reveal a clearer interpretation of the different results either (compare Tab. 1 and Tab. 2).

2.3 Discussion of open questions and formulation of the aim of the presented study

In the previous discussion of hitherto existing studies of liquid transport in carbon nano channels, it came out that nanoporous graphitic media might facilitate extremely elevated flow rates, while simultaneously exhibiting high selectivity due to the nanometric pore diameters. This would offer exciting possibilities for different applications. Unfortunately, numerous inconsistencies of both quantitative and qualitative nature, give cause to doubt the predictions – especially the most promising ones. Furthermore, to our knowledge, no attempt exists to predict the flow enhancement from a theoretical model like for example the one discussed in 1.3.3, and to quantitatively compare the outcome of simulation studies to such a model. Instead, empirical explanation attempts refer to the breakdown of continuum theories [41, 99, 105], confinement effects influencing water properties like diffusion and viscosity [100], or low interface friction due to the atomic smoothness of the graphite wall [67]. Others evoke a non-wetting behavior of water in CNT and attribute the high slippage to a low liquid/solid binding energy [100, 54], or postulate a depletion zone at the interface [48, 75]. But so far, no description of the water/CNT interface properties has been given that could conclusively explain the observed high flow rates.

Consequently, in view of the applications at stake, there is great need for further careful investigations of the matter, in order to clarify the situation. Beyond that, from a fundamental point of view, it is also of major interest to gain further understanding of the physical mechanisms at the bottom of liquid-solid friction in general.

Against this background, we performed a thorough study of liquid/solid interface friction in graphitic systems of different geometries. In recognition of the significant role of water for the mentioned applications at stake, we put our main focus on water/CNT systems. Our first aim is to identify the relevant properties of the considered systems, that influence the amount of interface friction, and hence, the water flow behavior. To this end, we use molecular dynamics simulation, that permits to perfectly control the system's characteristics, to investigate systematically the influence of various factors, like for example, the CNT radius. Furthermore, we benefit from the microscopic nature of MD simulations to search on a molecular level for the control parameters of the macroscopic boundary condition. Our ultimate goal is to give a theoretical description of water/graphite friction that quantitatively explains the numerically measured flow rates. Such a model would enable us to make a soundly based prediction for the order of magnitude of the flow enhancement for water in CNT.

Part II

Molecular dynamics simulation study of water in confined graphitic systems

This part consists of an exhaustive study of nanometric water/graphitic systems by means of molecular dynamic (MD) simulations. After a short introduction to MD simulations of water in general, and of water in CNT in particular, we pass to the first main part of our work: the measurement of water/graphite friction in systems of various geometries and topologies. We motivate the focus on water/graphite *friction* and the choice of systems that are considered, before describing simulation procedures and friction measurement methods. A discussion of the obtained results follows: We report on low friction supporting high water flow rates; furthermore, the friction coefficient was found to be independent of confinement, but extremely sensible to wall curvature. Afterwards, the robustness of the results is validated performing various tests. Furthermore, a quantitative comparison to the existing results – that have been discussed in the previous part – is conducted. Finally, the results are analyzed with regard to parameters that influence liquid/solid slip as it was discussed in section 1.3, namely wetting properties, depletion and pressure. However, none of these parameters was found to explain the curvature dependent friction coefficient. Anticipating the following part III, we mention that this lack of understanding of the observed flow behavior prompted us to theoretical investigations which will allow to predict the water/graphite friction coefficient based on microscopic properties of the interface.

Contents

3 MD simulation of water/graphite systems 33

3.1 Introduction and motivation to use molecular dynamics simulation 33
3.2 Empirical potentials to model water 35
3.3 Confined water in graphitic systems 36
3.4 Summary: Interaction potentials employed in the study at hand . 37

4 Equilibrium and flow measurement of water/graphite friction 39

4.1 Measuring the friction coefficient - a new approach to determine the liquid/solid boundary condition 39
4.2 Geometry of the considered systems 40
4.3 Equilibration process (temperature and pressure control) 42
4.4 Flow measurement of the friction coefficient 43
4.5 Equilibrium measurement of the friction coefficient 45
4.6 Discussion of results: Curvature dependent friction 46
4.7 Testing the robustness of the main outcome 47
  4.7.1 Independence on confinement 47
  4.7.2 Further check-ups on the robustness of the friction results . 48

5 Comparison to literature: Linking friction, slip, shear viscosity and diffusion 50

5.1 Further studies of water confined in the graphene slab geometry: viscosity and diffusion 50
  5.1.1 Measurement of slippage and viscosity in Couette flow simulations 50
  5.1.2 Equilibrium measurement of the self diffusion coefficient . . 52
5.2 Comparison to other groups' results 53

6 Incompatibility with the common slip models 56

6.1 Normal pressure 56
6.2 Wetting behavior: depletion and contact angle 58
6.3 Interface water structure 59
6.4 Conclusion 62

3 Molecular dynamics simulation of water/graphite systems

The fact that water flow through CNT has been studied above all with molecular dynamic simulations is a logical consequence of the principle idea MD simulation is based on. In the following, a reminder of this basic idea of MD, its advantages and inconveniences, will make it apparent why MD simulations are a suitable tool for investigations of fluid properties at the nanoscale. For a detailed introduction to MD simulations we refer to the appropriate textbooks [83, 25, 80].

We thus motivate why we perform yet another MD study of water flow through CNT, before introducing some important points of MD simulations of water in general, and finally, of water/graphite systems in particular. Many points that are raised in this section are discussed at length in an instructive review given by Alexiadis and Kassinos, that specifically deals with *MD simulations of water in carbon nanotubes* [1].

Finally, we introduce the most commonly used water models, including the two models – TIP3P and SPC-E – that have been used for our studies.

3.1 Introduction and motivation to use molecular dynamics simulation

The basic idea of MD simulations is to calculate the trajectories of a set of atoms (mass m_i and positions $\mathbf{r}_i$, $i = 1...N$) according to Newton's equations of motion

$$m_i \, \partial_t^2 \mathbf{r}_i = -\nabla_{\mathbf{r}_i} \left(U(\mathbf{r}_1, ..., \mathbf{r}_N) + U_{\mathrm{ext}} \right) \tag{8}$$

where U is the total potential energy depending on all atom positions and U_{ext} an external potential like, for example, a gravitational field. In MD simulations, these equations are numerically integrated with an algorithm that determines the position of each particle after n time steps δt, based on their positions at preceding time steps. Multiple algorithms are conceivable to perform this task, but not all of them will result in realistic time-evolutions of the thermodynamic properties of the given system. In no case the calculated trajectories will be the exact solution of the equations of motion; due to numerical errors, the trajectories always diverge exponentially from the 'real' ones after a limited number of time steps. However, the average behavior of the whole statistical ensemble is still thought to be accurately predicted under certain conditions, that is most importantly, if energy conservation is respected adequately. A prerequisite for energy conservation is a time-reversible algorithm. The most commonly used formulation fulfilling these requirements, is the Verlet algorithm or a variation thereof.

Apart from the mathematical question whether an algorithm accurately reproduces or not, the long-time evolution of the system's statistics, a second factor intervenes when it comes to modeling the behavior of a real physical system. The significance of simulation result depends crucially on the empirically chosen energy potential.

The potential energy includes intramolecular contributions, and contributions from interactions between atoms that are part of different molecules. For the latter, non bonded, atoms, only two particle interactions (atoms i and j at distance r_{ij}) are taken into consideration: Electrostatic interactions between two charges q_i and q_j are given by the Coulomb potential

$$U_{\text{Coulomb}}(r_{ij}) = \frac{q_i q_j}{4\pi\varepsilon_0 r_{ij}} \tag{9}$$

with the dielectric constant ε_0. Long ranged attractive Van der Waals force and short ranged repulsive force due to overlapping electron orbits (Pauli repulsion) are commonly modeled combined via the Lennard-Jones potential

$$U_{\text{LJ}}(r_{ij}) = 4\epsilon_{ij}\left[\left(\frac{\sigma_{ij}}{r_{ij}}\right)^{12} - \left(\frac{\sigma_{ij}}{r_{ij}}\right)^{6}\right] \tag{10}$$

where ϵ_{ij} is the minimal potential energy and σ_{ij} the distance, where the potential is zero.

The intramolecular potential energy is usually split into the following contributions: One associated with the distance between two bonded particles, a second one associated with the angle between two neighboring bonds and further parts associated with the torsion angle of two atoms separated by three bonds. The first two – bond and angle – are commonly modeled with harmonic potentials, the third one with a dihedral potential. Interactions of atoms that are separated by more than three bonds are neglected in most models. Instead of using these intermolecular potentials, molecules are also often considered as rigid bodies. The reason for this further simplification is mostly the need/wish to save computation time, a point which leads directly to the discussion of some major (dis)advantages of MD simulations.

Systems that can be studied with MD simulations are typically of nanometric size (between $10^{-9} - 10^{-7}$ m) and contain $10^3 - 10^4$ particles. Simulation times are also in the nanoseconds-range. These length and timescales are inconceivably short compared to the macroscopic world we experience in every day life. Seemingly simple effects (like, for example, freezing water), constitute a big challenge to observe in simulations because the implied time- and/or length scales can not be handled with available computational power. However, what presents itself as a major inconvenience of MD techniques where macroscopic systems are concerned, transforms in a great advantage when we are interested in the 'nanoworld'. For system sizes comparable to atomic lengths, the number of particles is feasible and physical effects that happen on the nanoscale can be perfectly well investigated by means of MD simulations. Contrarily, this can not yet be said about the handling of nano-objects for experimental or technological purposes, in spite of impressive advances concerning scale reduction to micro- and ultimately to nanofluidic devices. MD simulations on the other hand not only represent a suitable tool to study the length and timescales of interest, but also offer a perfect control of system size and geometry. In fact, in simulations we can easily exceed practical limitations of real world experiments and prepare 'artificial' setups – systems that have not yet been realized, or are not realizable at all. This control makes it possible to investigate the role of certain parameters with tailor-made setups.

Still, although simulations are a convenient and suitable tool for investigations in the field of nanofluidics, they do not supersede experiments. The pertinence of MD simulation results depends crucially on the accurateness of the potential energy function in Eq. (8) that is used to calculate all atomic forces. In practice, this accounts to choosing the geometry of the molecules and the functional forms of the interaction potentials as well as the free parameters like electrical charges, Lennard-Jones ϵ and σ, etc... in a way that quantitatively reproduces real properties, that is to say experimentally measurable values like, for example, density, viscosity, etc... of a fluid. The ensemble of these parameters makes up a model. In the following, some common water models will be introduced and the choice which water models we use for our studies will be explained.

3.2 Empirical potentials to model water

The behavior of water as it is experienced in every day life forms the common view of 'normal' liquid properties to a large extend. And from a scientific point of view, concerning the field of fluid dynamics, water is classified as a *simple liquid*, referring to its 'simple' rheological properties: water keeps the same viscosity under shear, independent of the applied shear rate. However, contrary to the impression one could get, water is far from being an 'ordinary' substance: Dozens of cases have been found to date, were water behaves in an anomalous way, which explains why the behavior of water – also extensively studied – is still not completely understood.

Not surprisingly, when numerical simulations emerged as a new complimentary way to study materials, water has been in the main focus. Unfortunately, it also turned out to be rather resistant to the attempt to find a model that quantitatively reproduces *all* its physical properties. Over the years, a large number of water models has been proposed (almost 50 models in 2002, [33]). Starting from some geometric assumptions, a model was usually developed by fitting the free model parameters to reproduce one (or few) particular real water characteristics. Improving a model with respect to one property often implied a less good compliance with another one. Moreover, better quantitative agreement was achieved with ever more complicated models with an increasing number of degrees of freedom per molecule. This has negative implications for the necessary computational time.

Commonly used models include geometric representations of the water molecule with three, four or five interaction sites. The interaction sites of the so called '3-site models' are the oxygen and the two hydrogen atoms, represented by point masses. To reproduce the water dipole moment, every mass also carries a charge. A Lennard-Jones potential is attributed to the oxygen atom, but not to the hydrogen atoms. Popular 3-site models are the transferable intermolecular potential 3 point (TIP3P) water model and the extended version of the simple point charge (SPC-E) water model. These are the two models that we used for our studies. In both cases, molecules are kept rigid, which means that intramolecular bond lengths and angles are fixed. TIP3P and SPC-E differ in the values for the geometry (bond length

Figure 6: Geometry of the 3-site water models TIP3P and SPC-E.

and angle) and interaction parameters (LJ-σ,ϵ and charges). The geometry for both models is sketched in Fig. 6. In more complicated models further hypothetical interaction sites with point charges, are added. Examples are the TIP4P and TIP5P [66] water model, with one or two extra-charges added, respectively.

There is no general answer to the question which model is the best one. A choice has to be made according to the aims of the envisioned study: Which physical properties are studied under what thermodynamic conditions, and how much computational power is available. 3-site models have the advantage of relatively low computational cost and, despite their simplicity, give instructive results that qualitatively and semi-quantitatively reproduce the basic properties of water under ambient conditions [23, 33, 104].

Furthermore, all water models have been optimized for the reproduction of *bulk* water properties. So far, lacking the necessary experimental results to do so, they have not been validated for *confined* water. Ab initio simulations of water confined in silicalite pores, suggest that the molecular dipole moment decreases about 10%, with consequences for the wetting properties [79]. In our opinion, the quantitative improvement for the bulk water properties that can be reached with more sophisticated models is not worth the implied elevated expenditure of time. Even more so, since it is not clear that these models also give more reliable results in confined systems.

3.3 Confined water in graphitic systems

After the above brief discussion of the theoretical description of bulk water, we now turn to the modeling of water/graphite systems. In this context, we focus mainly on the water/carbon interaction parameters. Possibilities to model and investigate properties of graphitic solids (like for example graphene, carbon nanotubes, fullerenes) will be skipped. The reason for this is, that in our simulations, carbon walls are modeled as a rigid body, where atoms are fixed at all times at their equilibrium positions, which makes the definition of a potential energy function for the bonded carbon-carbon interactions superfluous. Simulations with flexible and fixed walls were shown to give similar results for the statics and friction of confined water [1, 99, 109], flexibility increasing flow by a small (10-20%) and systematic amount [89, 48].

Contrarily, one expects the liquid-solid interaction to be crucial for the overall

Water/carbon model parameters

	TIP3P/AMBER	SPC-E/Werder
$d_{\mathrm{OH}}(\text{Å})$	0.9572	1.0
$\sphericalangle$ HOH	104.52	109.47
$q_{\mathrm{O}}(\mathrm{e})$	-0.834	-0.8476
$q_{\mathrm{H}}(\mathrm{e})$	0.417	0.4238
$\sigma_{\mathrm{OO}}(\text{Å})$	3.151	3.166
$\epsilon_{\mathrm{OO}}(\mathrm{kJ/mol})$	0.636	0.650
$\sigma_{\mathrm{OC}}(\text{Å})$	3.276	3.190
$\epsilon_{\mathrm{OC}}(\mathrm{kJ/mol})$	0.477	0.392

Table 3: Water model and interaction parameters for the two water models employed in the presented study.

systems behavior, especially for highly confined water, where the interface region is larger than the bulk region. Indeed, Werder *et al.* found that the water-carbon interaction energy has a significant influence on the water/graphite contact angle [109, 44] and used this to calibrate the oxygen-carbon Lennard-Jones parameters (for usage in combination with the SPC-E model) to reproduce experimental results [24, 73] for the water/graphite contact angle $84 - 86°$. These parameters, however, lead to a non-wetting behavior of water in CNT, which is in contradiction to experiments [28]. A lot of other parameters have also been used (see Tab. 1 for the numerical studies of water flow in CNT that were discussed in part I). They are either obtained by fitting them to some experimental data, or by applying Lorentz-Berthelot mixing rules

$$\epsilon_{ij} = \sqrt{\epsilon_i \epsilon_j} \qquad\qquad \sigma_{ij} = (\sigma_i + \sigma_j)/2 \tag{11}$$

to already existing C-C and O-O parameters, that have been previously determined for other systems.

To sum up the situation, the question which water model and which C-O interaction parameters are best to use for simulating water in CNT is still wide open and can not be answered properly without analogous experiments or with still increasing computer performance results from ab initio simulations. For this reason, we used two different combinations of water model and C-O parameters to check the robustness of our results.

3.4 Summary: Interaction potentials employed in the study at hand

Following Hummer *et al.* [41], we performed most simulations with TIP3P water and the AMBER96 force field [15]. For comparison, we also used the SPC-E water model in combination with the oxygen-carbon interaction parameters given by Werder *et al.* [109], with a cut-off distance of 1.0 nm. Parameters for both models are summarized in Tab. 3. The positions of the carbon atoms were fixed at all times. This simplification was found by others to give somewhat lower flow rates for water flow in CNT, but the difference is acceptable since it is systematic and relatively small [1, 99, 109, 89, 48].

Simulations were mainly performed with the LAMMPS molecular dynamics package [77], that uses a modified version of the Verlet algorithm. Electrostatic interactions were computed with the particle-particle particle-mesh (PPPM) method [78] and rigidity of the water molecules was assured with the SHAKE algorithm [84]. Additionally, we also used GROMACS [103] as a comparison. The GROMACS simulations were carried out by Felix Sedlmeier in the group of Roland R. Netz (Physics Department, Technical University Munich).

4 Equilibrium and flow measurement of water/graphite friction in various confined geometries

Although a number of MD studies of water in CNT has already been undertaken, the work presented in the following stands out due to the direct focus on liquid/solid friction. Furthermore, we perform simulations of a variety of graphitic systems to distinguish between the influence of curvature and confinement, and we measure the friction coefficient in two independent ways.

4.1 Measuring the friction coefficient - a new approach to determine the liquid/solid boundary condition

The friction of liquids on solid surfaces is usually discussed in terms of the partial slip hydrodynamic boundary condition that relates the fluid velocity v_{slip} at the solid surface to its gradient $\partial_n v$ in the direction normal to it as:

$$b\ \partial_n v = v_{\text{slip}} \tag{12}$$

where b is the slip length [7]. Various numerical studies have quantified slippage of water in CNT by measuring directly the velocity profiles and comparing it to the expected parabolic form

$$v(r) = \frac{R^2}{4\eta}\left(1 - \frac{r^2}{R^2} + \frac{2b}{R}\right)(-\partial_z P) \tag{13}$$

The shape of the velocity profile depends apart from the confinement and the external driving force, e.g. the pressure gradient $\partial_z P$, only on the shear viscosity η of the fluid and the slip length b. Hence, for a given confinement and forcing, both the slip length and the viscosity can be found from a 2-parameter fit to the measured velocity profile. But this approach becomes inefficient when b is substantially larger than the confinement. In this case the velocity profile tends to a plug which leads to large uncertainties for the parabolic fit. Some authors made an effort to reduce the error by determining the viscosity independently. This can be done by measuring the self diffusion coefficient which is connected to the fluid viscosity. In bulk systems where the relation between viscosity and mobility/diffusion is given by the well known Stokes-Einstein relation $D_{\text{bulk}} = k_{\text{B}}T/3\pi\eta a$ with a the particle diameter. However, under confinement this relation is much more subtle than in bulk [85]. Using the Einstein relation to calculate the shear viscosity from the measured diffusion remains questionable.

In this work, we have thus taken a different approach and focused on the liquid/solid friction coefficient of water at graphitic surfaces. The friction coefficient is the physically relevant property characterizing the interfacial dynamics, a large slip length being associated with a low friction. Indeed, the partial slip boundary condition stems physically from the identification of the 'bulk' viscous stress $\sigma_f = \eta\ \partial_n v$ with a surface fluid/solid friction force $F/\mathcal{A} = -\lambda\, v_{\text{slip}} = -\sigma_f$, with λ the fluid/solid friction coefficient and $\mathcal{A}$ the contact area. The slip length is accordingly deduced by the relation $b = \eta/\lambda$. For large slip length $b \gg R$, the velocity profile Eq. (13) tends to plug flow

$$v(r) \equiv v_{\text{slip}} = \frac{R}{2\lambda}(-\partial_z P) \tag{14}$$

and depends only on the ratio of viscosity and slip length, or in other words, it depends only on the friction coefficient. Under this condition, the fluid's dynamics are completely determined by the interface friction, and not by the viscosity. This can also be seen in Eq.(2) for the flux that reduces to $Q = \frac{\pi R^3}{2\lambda}(-\partial_z P)$

In this study, we performed both equilibrium and non-equilibrium molecular dynamics simulations of water in different graphitic channels. Two independent approaches were followed to extract the friction coefficient λ:

1. In simulations of pressure driven flows, the friction force of water at the surface and the slip velocity were measured to determine the friction coefficient as

$$\lambda = -\frac{F}{\mathcal{A}\, v_{\text{slip}}} \tag{15}$$

2. In equilibrium (flow free) situations the friction coefficient is calculated from the Green-Kubo relation

$$\lambda = \frac{1}{\mathcal{A} k_{\text{B}} T} \int_0^\infty \langle F(t) F(0) \rangle \, \mathrm{d}t \tag{16}$$

4.2 Geometry of the considered systems

Several possible explanations have previously been proposed for the unexpected high flow rate that was found experimentally. In part I we discussed the possibility of i) a breakdown of hydrodynamic theory in ultra-high confinement, ii) gradually changing fluid properties (especially viscosity) due to confinement and iii) change of boundary conditions (slip length) caused by wall curvature.

Keeping these hypotheses in mind, we investigated the following three different system types:

1. water inside armchair CNT
2. water outside armchair CNT
3. water in graphene slab

With the choice of *armchair* nanotube (chirality (n,n)), we follow the lead of the other groups that have already performed MD simulations of water in CNT; see section 2.1. We also considered *zigzag* CNT (chirality (0,n)) to test the influence of the CNT structure on the friction coefficient. Results for this test will be discussed later on in chapter 9. First, we concentrate on the armchair systems. We change curvature and confinement by using various tubes with diameters ranging from 10.2 nm down

Considered geometries: water in graphene slab, inside and outside CNT

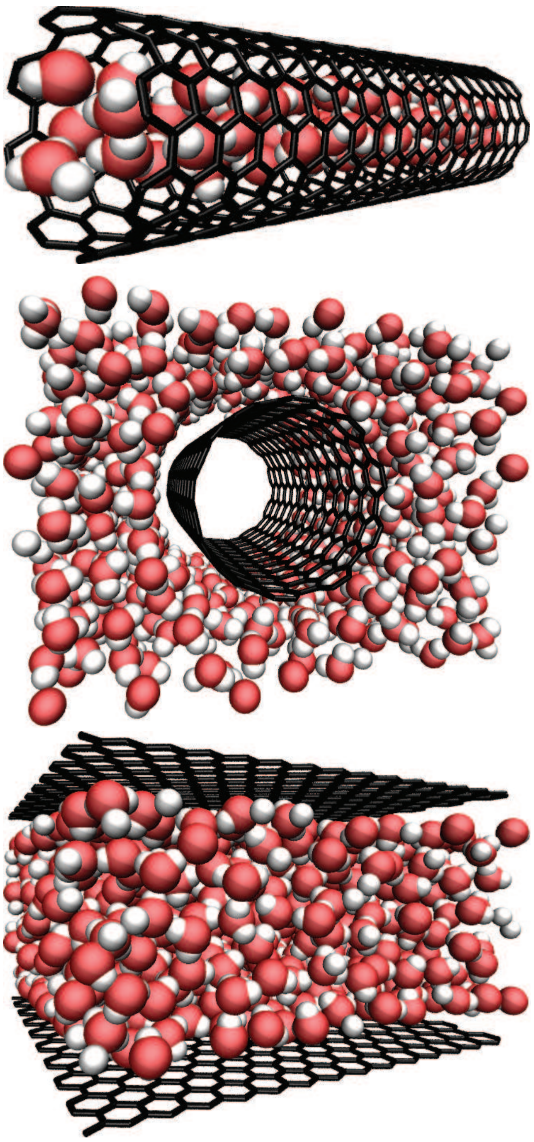

Figure 7: Various geometries were considered in the presented study of water-carbon friction: water inside (*upper*) and outside (*middle*) armchair CNT, as well as water confined in a slab of two parallel graphene sheets (*lower* figure). These setups allow to distinguish between confinement and curvature effects on the friction coefficient.

to 0.68 nm. In addition to the classic setup of a water filled nanotube, we also looked at nanotubes surrounded by water. This expands the observation range to negative wall curvature and it allows to look at the influence of curvature in the absence of confinement. Furthermore, in order to fully disentangle the roles of confinement and topology, we have also explored a slab geometry, with water confined between two parallel graphene sheets, with width varying between 6.1 nm and 0.68 nm. Snapshots of the three different systems are shown in Fig. 7.

The graphene structure is given by a honeycomb lattice with a carbon-carbon distance $d = 0.142\,\text{nm}$. Carbon positions are $n_+\mathbf{a}_+ + n_-\mathbf{a}_-$ with $n_\pm \in \mathbb{N}$ and the lattice vectors

$$\begin{aligned} \mathbf{a}_+ &= \frac{l_0}{2}\begin{pmatrix}\sqrt{3}\\ 1\end{pmatrix} \\ \mathbf{a}_- &= \frac{l_0}{2}\begin{pmatrix}\sqrt{3}\\ -1\end{pmatrix} \end{aligned} \tag{17}$$

where $l_0 = \sqrt{3}d$. Carbon nanotube are 'prepared' by 'rolling' rectangular graphene sheets to a cylinder. Depending on the orientation of the tube axis $n\mathbf{a}_+ + m\mathbf{a}_-$ with respect to the graphene structure, CNT are called 'armchair', 'zigzag' or 'chiral' CNT. For armchair CNT the cylinder axis is in direction $\mathbf{a}_+ - \mathbf{a}_-$; for zigzag CNT it is in direction $\mathbf{a}_+ + \mathbf{a}_-$.

4.3 Equilibration process (temperature and pressure control)

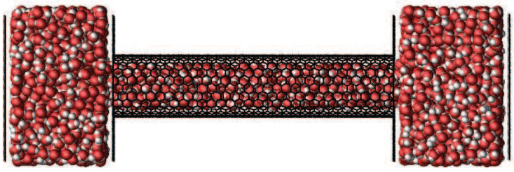

Figure 8: System equilibration (NPT) with reservoir

All simulations were performed at constant number of particles, volume and temperature (NVT). During equilibrium as well as flow simulations, temperature was held constant at 300K by a Nosé-Hover thermostat which was coupled on the velocity components perpendicular to the flow direction. No heating was observed. The relaxation time of the thermostat was 0.2 ps (= 100 time steps) which is several orders of magnitude smaller than the time needed to establish a stationary flow profile (∼ 1 ns). Hence, we are confident that the thermostating did not affect the simulated fluid flow in any unphysical way.

In order to ensure equal pressure conditions for all simulations, the number of water molecules was previously determined in additional equilibrium simulations with tubes of finite length. For water inside a CNT, reservoirs were added at both open ends of the tube. The reservoirs were kept at 1 atm by a piston. For simulations of water outside CNT, the pressure was also imposed by a piston perpendicular to the tube axis. After a certain time, the systems reached a stable equilibrium. Then the reservoirs were removed and periodic boundary conditions were applied.

In most of the slab simulations, the number of molecules was fixed arbitrarily, and the volume was adjusted instead to control the pressure: One graphene plane

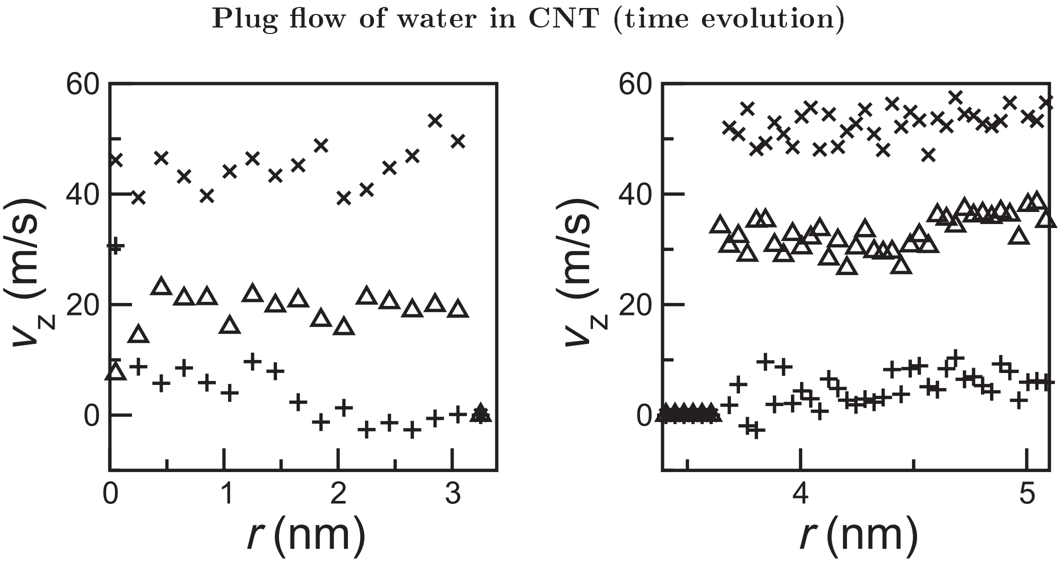

Figure 9: Flow profiles inside (*left*) and outside (*right*) a CNT with radius $R = 3.39$nm. Water was initially at rest and was then accelerated by a constant force. The shown profiles result from time averages over 20 fs, starting 0(+), 0.08(△) and 0.18 ns(×) after switching on the external force.

was used as a piston while the second plane was fixed. For the subsequent measurements, the positions of both planes were fixed at the equilibrium distance which was found. This process requires less particles and therefore less computing time than an equilibration with particle reservoirs. This procedure is not suitable for slab sizes $H \lesssim 1.5$nm, where hydrophobic interactions between walls start to become noticeable. If the wall is allowed to move, dewetting may occur and lead to air cavities. Completely water filled graphene slabs of sub nanometer size can be obtained, however, by using particle reservoirs (at 1atm) as for the CNT.

4.4 Flow measurement of the friction coefficient

In non-equilibrium simulations, the friction coefficient was determined according to Eq. (15) by measuring the friction force F and the slip velocity v_{slip} for different flow velocities.

Water flow was driven by applying a constant acceleration $a_0 \sim 10^{-4}\frac{\mathrm{nm}}{\mathrm{ps}^2}$ to all O and H atoms (corresponding to a pressure gradient $\sim 10^{14}\frac{\mathrm{Pa}}{\mathrm{m}}$, a driving force similar or lower than in previous works [98, 48]). Due to the very large slippage at the surfaces, velocity profiles are flat (plug-like) over the channels' width. The slip velocity v_{slip} is defined as the fluid velocity within the first water layer close to the surface. But due to the flat velocity profiles, the slip velocity can be identified in good approximation with the averaged fluid velocity. In fact, the radial velocity profile was found to be constant within the uncertainties due to statistical fluctuations of the streaming velocity. In parallel to the slip velocity, we measure the friction force F between wall and water due to all particle-particle interactions between oxygen

Friction force vs. slip velocity

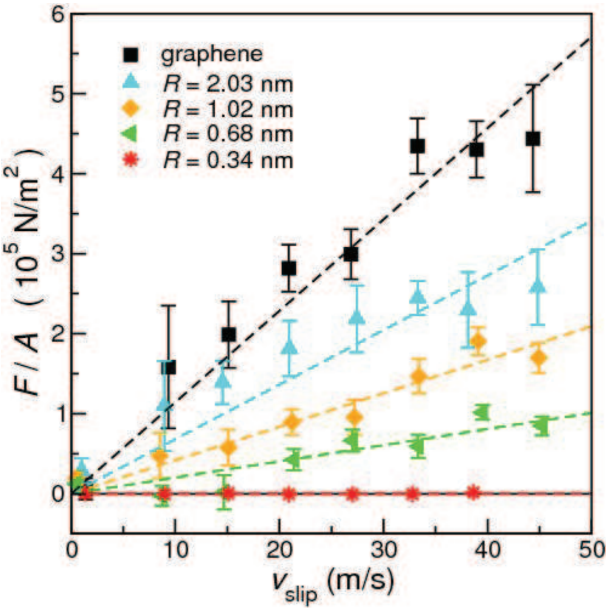

Figure 10: Friction force of water versus slip velocity at the carbon nanotube surface for various confinements inside the CNT. From bottom to top the CNT radius is $R = 0.34, 0.68, 1.02, 2.03\,\mathrm{nm}$. The top result is for the graphene slab (with wall-to-wall distance $h = 3.23\,\mathrm{nm}$).

and carbon atoms. The contact area

$$\mathcal{A} = 2\pi r_{\mathrm{eff}} L \tag{18}$$

between water and CNT (inside and outside) is calculated with the effective radius

$$r_{\mathrm{eff}} = R \mp \frac{1}{2}\sigma_{\mathrm{oc}}. \tag{19}$$

During a simulation both the friction force F and slip velocity v_{slip} increase over very long time scales (nanosecond), to finally reach a stationary state. However, as a consequence of the low liquid/solid friction, this relaxation time $\tau \sim \rho R/\lambda$ is much larger than the momentum diffusion transfer time scale associated with the building up of the flow profile, and one may consider this relaxation as a quasi-stationary state [6]. One example for the time evolution of the velocity profiles is shown in Fig. 9. We thus take benefit of this time-scale separation by measuring the force-velocity relationship in a single simulation within such a quasi-stationary regime. During 0.2 ns, F and v_{slip} were calculated every 2 fs and averaged over time intervals of 20 fs. The slope of $F(v_{\mathrm{slip}})$ was then determined from a linear fit on the resulting 10 data points. Statistical uncertainties were estimated by repeating this procedure for ~ 20 different initial configurations. We find a linear relationship between the friction force and the slip velocity up to $v_{\mathrm{slip}} \sim 50\,\mathrm{m/s}$. Non-linear deviations are observed for higher velocities: The friction force was found to depend under proportional on the slip velocity for higher velocities. We will come back to this point later on.

---

[6] The time evolution of the velocity for plug flow under a constant acceleration a_0, where $v(t = 0) = 0$, is given by the equation of motion $\frac{\mathrm{d}v}{\mathrm{d}t} = -\frac{\lambda\mathcal{A}}{M}v + a_0$ (M the total mass of the liquid). The solution is $v(t) = \tau a_0(1 - \exp(-t/\tau))$ with the relaxation time $\tau = \frac{M}{\lambda\mathcal{A}} = \frac{\rho R}{2\lambda}$.

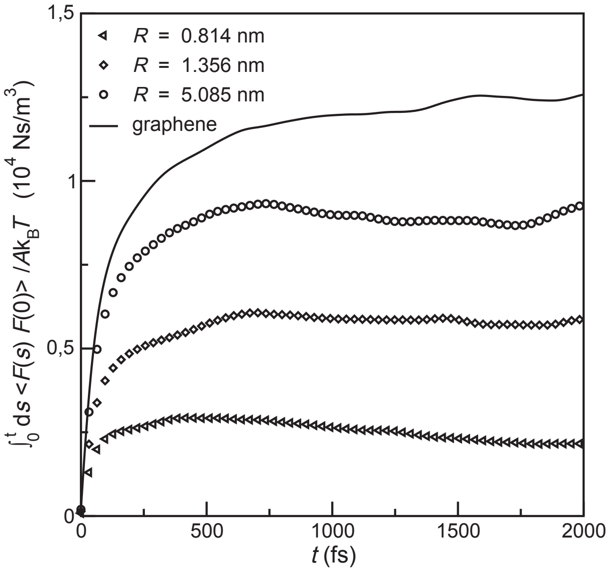

Friction coefficient via Green-Kubo expression

Figure 11: Integral of the force auto correlation function measured in equilibrium simulations for various CNT radii. The friction coefficient was obtained from the plateau value. As in the flow simulations, we observe a decrease in friction with the CNT radius.

Fig. 10 shows some results for $F(v_{\mathrm{slip}})$ in the linear regime. For better visibility, the original data points (200 for each tube) were averaged within certain velocity intervals. The dotted lines represent the results for the friction coefficient λ that we obtained from the described evaluation procedure.

4.5 Equilibrium measurement of the friction coefficient

To test the robustness of the results from the flow measurements, the friction coefficient was also determined via the Green-Kubo relation Eq. (16). In equilibrium simulations of about 1 ns, we measured every 2 fs the total force F between all oxygen and carbon atoms - as it was done before in flow simulations, but without any external forcing (leading to zero mean force $\langle F\rangle$ in the thermodynamic limit). We are now interested in the force *fluctuations* and more specifically, its temporal autocorrelation $\langle F(t)F(0)\rangle$.

A well documented difficulty of such equilibrium estimates of Green-Kubo relationships is associated with the finite size of the simulated system, which leads on very long times to a vanishing of the friction coefficient due to an inversion of infinite time and thermodynamic limit [21, 6]. However this decay of the time integral occurs on very long time scales (here, typically ns) and a plateau value can be defined over intermediate times in the picosecond range (see Fig. 11), thereby avoiding this spurious long time effect. In the following, we take this plateau value as the equilibrium value for the friction coefficient. The value for λ is obtained from the plateau of the integrated force autocorrelation function, obtained typically in the range $t \in$ [1ps;10ps].

4.6 Discussion of results: Curvature dependent friction

The results for the three different geometries and two different measurement methods are gathered in Fig. 12. We compare the friction coefficient for water inside a graphene slab and water inside as well as outside a CNT as a function of the confinement. For the slab geometry the confinement is quantified by the half distance of the graphene sheets, and in case of CNT by the nanotube radius.

The first key result highlighted by this plot is, that the friction coefficient λ is strongly dependent on the *curvature* of the graphitic surface: it decays with CNT radius for *positive* curvature (water *inside* nanotubes), but increases for *negative* curvature (water *outside* nanotubes). In contrast the friction coefficient for the graphene slab (with zero curvature) is found not to depend on the confinement, confirming that the curvature is the relevant parameter controlling friction. A second key conclusion is that the friction coefficient vanishes - within numerical uncertainty - below a threshold radius ($R_c \approx 0.4$nm), leading to a 'superlubric' behavior of water in CNT

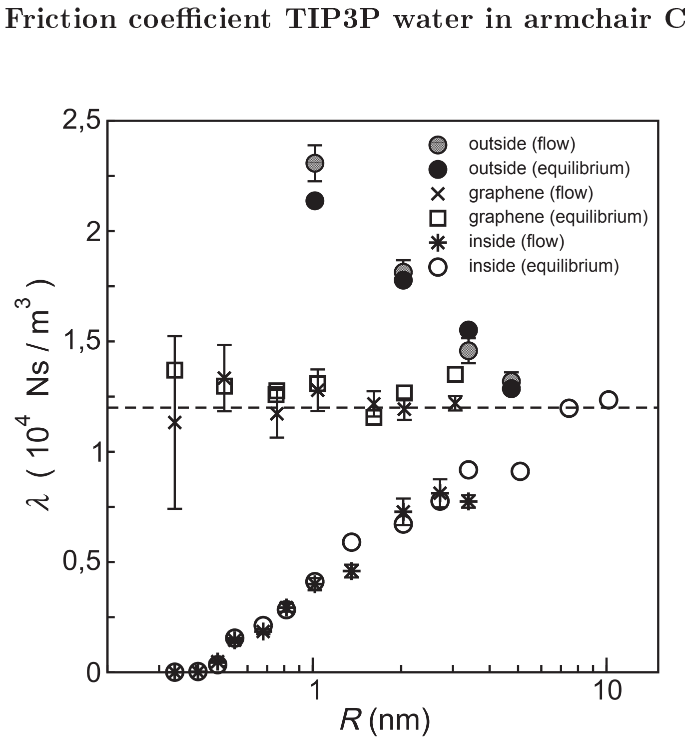
Friction coefficient TIP3P water in armchair CNT

Figure 12: Evolution of the friction coefficient λ with the confinement R, for water inside/outside CNT and between graphene sheets. For CNT, R is the radius of the tube, while for slabs it is the half-distance between the graphene sheets. Flow measurements: graphene (×); armchair CNT, inside (∗) and outside (•). Equilibrium measurements: graphene (□); armchair CNT, inside (○) and outside (•). Otherwise indicated, uncertainties are on the order of symbol size.

with radius below R_c. Another remarkable feature to be noted is that the friction coefficient is found to deviate significantly from its flat surface value ($R \to \infty$) already for low confinement, that is to say for CNT diameters about ~ 10 nanometers. The occurrence of such an effect at relatively 'large' system sizes - with respect to the molecular diameter of water - is quite puzzling.

Finally, we point out that the values for the friction coefficient measured in flow and equilibrium simulations match well, confirming on the one hand the general robustness of the results, and on the other hand that the flow measurement of the friction coefficient was carried out in the linear response regime $\lambda \propto v_{\text{slip}}$.

4.7 Testing the robustness of the main outcome

Due to the fact that the results for the friction coefficient from two totally independent measurement methods agree quite well, we are confident about their validity. Still, so far we lack an explanation for the curvature dependent liquid/solid friction and the occurrence of superlubricity. Even more important, numerical experiments depend on the molecular models and interaction potentials that are used to calculate the atomic forces. And finally, erroneous implementation in the applied simulation package might lead to unphysical effects, as it was, for example, found recently for MD simulations of water with GROMACS in the presence of an external electric field [10]. Considerable effort has thus been made to ascertain the correctness of the presented results: On the one hand, we further tested the conclusion that confinement does not influence the friction coefficient by simulating water in a square CNT (Fig. 13). On the other hand, we checked for a possible influence of the chosen water model and simulation software. These tests are discussed in the following.

4.7.1 Independence on confinement

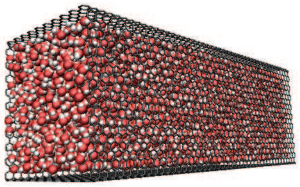

Figure 13: square tube

Based on the results for the graphene slab simulations, we argued that the friction coefficient is independent of confinement. This is backed by the results for large CNT diameters > 10 nm which approach the value for zero curvature for both water inside and outside of the CNT.

However, one might note that in the slab geometry, water is confined only in one dimension, while in CNT it is confined in two dimensions. In order to leave no doubt concerning this question, we also considered water in a block-shaped tube with a square cross section of $4.26 \times 4.26\ \text{nm}^2$ and 7.87 nm length. A snapshot of this system is shown in Fig. 13. Measurement of the friction coefficient according to Eq. (16) (in an equilibrium simulation) resulted in $\lambda = 1.29 \times 10^4 \frac{\text{Ns}}{\text{m}^2}$, in reasonable agreement with the results for the slab geometry, Whereas in a CNT with comparable diameter ~ 4 nm, the friction coefficient is about 40% smaller.

These results for water in a square tube confirm that friction of water on graphitic surfaces is not influenced by confinement that is several times the molecular diameter.

4.7.2 Further check-ups on the robustness of the friction results

Simulation parameters We performed several standard tests to exclude a dependence of the simulation outcome on simulation parameters: A possible effect of the fact that the **thermostat** was coupled only on two velocity coordinates was ruled out in an equilibrium measurement with a coupling to all three $\mathbf{v}$-components. Likewise, it was checked that the **simulation box** was large enough, so that interaction of periodic images of water filled tubes with each other did not influence the results. Diminishing the **time step** did not change the outcome either.

Water model As discussed in section 3, the validity of MD simulation results depend crucially on the accuracy of the model that is used to describe the various interactions - in this study, the water model and the oxygen-carbon interaction. To test the robustness of our results with respect to these parameters, we also performed equilibrium simulations for all system types (water inside/ outside CNT and in graphene slab) with the SPC-E water model and the water/carbon force field introduced by Werder *et al.* [44]. All parameters of the SPC-E modeling in comparison to TIP3P/AMBER can be found in Tab. 3. The main difference between both models is the water-graphene contact angle. Simulation of a water droplet on a graphene sheet gave a water-carbon contact angle of $\theta = 95°$ for SPC-E and $\theta = 57°$ for TIP3P.

The non-wetting behavior of the SPC-E water caused some problem with the pressure equilibration procedure for water in the CNT as it was described in the beginning. For the combination TIP3P/AMBER, the CNT was empty in the starting configuration, but water from the reservoirs immediately began to fill the tube. For SPC-E/WERDER parameters, however, a pressure of 1 atm is too low to force water into CNT. So, for the friction measurement with SPC-E water inside CNT, we used the same number of particles as for the TIP3P simulations. This means that these results were certainly obtained at a higher pressure than for SPC-E water outside and in the graphene slab, where the equilibrium number of molecules could be determined without problems.

The results for the two different water models are in qualitative agreement. The friction coefficient for the different SPC-E systems - shown in Fig. 14 - exhibits the same behavior as it was found before: Friction is independent of confinement, but very sensible to curvature. In general, friction measured with the SPC-E water model is higher than for TIP3P. For graphene, the difference is only about 10%; for water outside CNT, the friction coefficient is up to ≈ 50% larger. Given the differences in the wetting behavior for both models, however, it is somewhat surprising that we do not find a bigger discrepancy.

Implementation of MD algorithm (software package) Furthermore, we also cross-checked our results with equilibrium simulations performed with a different MD simulation package, namely GROMACS [103], in order to be sure they were not falsified by any error in the implementation. (It has recently been shown that some 'spurious results' for water in CNT in the presence of a static electric field

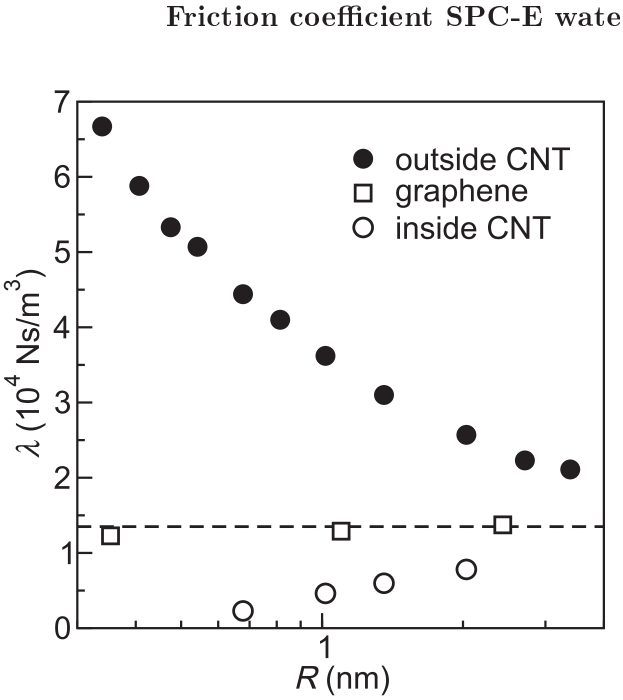

Figure 14: Results for the friction coefficient for water inside, outside armchair CNT and in the graphene slab geometry for the SPC-E water model and AMBER interaction parameters. Results obtained with the simulation packages LAMMPS and GROMACS are combined in this plot. The friction coefficient exhibits the same behavior for SPC-E water as for TIP3P water (compare Fig. 12): λ is independent of confinement; it increases with positive and decreases with negative curvature. The good agreement between results for both water models is quite surprising since the water carbon interactions used with SPC-E and TIP3P (AMBER and WERDER, respectively) lead to very different wetting behavior of water on graphitic surfaces.

were caused by a bug in GROMACS [10].) These simulations were carried out and evaluated by Felix Sedlmeier at the Physics department of the Technical University Munich. Results were compared for the TIP3P water model inside a CNT with diameter 1.36 nm and for the SPC-E model outside CNT with diameters 2.04, 4.06 and 6.78 nm. The values for the friction coefficient agree within 20%. Additionally to these tests, most systems of SPC-E water outside CNT were simulated only with GROMACS. Consequently, Fig. 14 where the friction coefficient for SPC-E water in all three geometries is displayed, gathers results from both packages, LAMMPS and GROMACS.

5 Comparison to literature: Linking friction, slip, shear viscosity and diffusion

Before changing over to the theoretical discussion of the curvature dependent friction coefficient, we would like to compare our numerical results to the previously conducted studies that have been presented in section 2 of experimental (see Tab. 2) and of numerical nature (Tab. 1).

Observing the friction coefficient λ to characterize the boundary condition for water flow in CNT is one of the main novel aspects of this work. Usually, the liquid/solid boundary condition is discussed in terms of slip length b. To link our work to previous studies and compare results directly, we would like to know how our results for the friction coefficient translate into the commonly used slip length. As already mentioned, λ can be expressed as the ratio of shear viscosity η and slip length b. The canonic way to measure the slip length in a cylindric geometry, is to impose a poiseuille flow and extract b as well as the viscosity from the velocity profile Eq. (13). But, due to the large slip $b \gg R$ the Poiseuille flow profile tends to a plug. In the simulations performed for the study at hand, statistical fluctuations make the flow profile indeed indistinguishable from plug flow. While we could use this fact to our advantage for the measurement of the friction coefficient, it renders the determination of slip length and viscosity via Poiseuille flow impossible for the system sizes and simulation times that have been used (compare Fig. 9).

Nevertheless, we can draw useful information from a comparison to the other groups results, as it will be discussed below. Among other things, we will highlight some subtleties in the relations between friction, slip and water viscosity on the one hand, and viscosity and self diffusion on the other hand, and the role of confinement thereon.

5.1 Further studies of water confined in the graphene slab geometry: viscosity and diffusion

To get an idea of the importance of confinement for viscosity and diffusion, we expanded our investigations of the graphene slab geometry: We conducted Couette flow simulations, which allow to compare η and b for different slab size. Additionally, the translational self diffusion was measured in equilibrium simulations. The outcome of these simulations will be presented in the following, before we turn to the comparison with other groups.

5.1.1 Measurement of slippage and viscosity in Couette flow simulations

We consider water confined between two parallel graphene planes at distance H. The system is sheared by imposing the wall velocities $\mathbf{v} = (\pm U,\ 0,\ 0)$. The resulting stationary velocity profile is the linear Couette flow profile whose slope s depends only on the channel width H, the wall velocity U and the slip length b (compare sketch Fig. 15) So for given H and U, we get the slip length from a simple linear fit on the velocity profile.

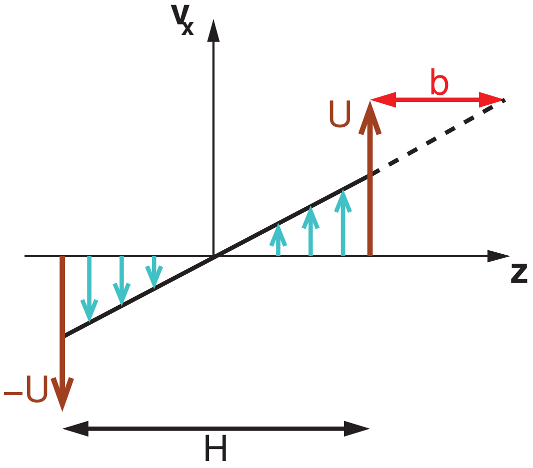

Figure 15: Couette flow geometry: Shearing water between two parallel graphene walls leads to a linear velocity profile whose slope depends on the wall distance H, the wall velocities $\pm U$ and the slip length b.

Furthermore, measuring in parallel the shear force F at the wall allows to determine the viscosity $\eta = F/\dot{\gamma}$. We have thus not only the possibility to measure the slip length but also get an idea of the influence of confinement on water viscosity. In addition, by measuring both η and b, we also just presented a third way to measure the friction coefficient λ in the slab geometry.

Although the situation is much more controllable than for poiseuille flow, because the mean total momentum is zero, the low fluid wall friction also poses some problems in the Couette flow experiment: Since low friction means low momentum transfer, the fluid velocity is much smaller than the wall velocity (about one order of magnitude). This is insofar problematic as for $U \gg v_{\text{fluid}}$ the wall velocity also sets the slip velocity $v_{\text{slip}} \approx U$. But in order to obtain valid results we have to limit the slip velocity to the regime of linear response, which implies maximum wall velocity 50 m/s. For this reason, water velocities are only about $\sim 1\frac{\text{m}}{\text{s}}$. This is the same order of magnitude as the equilibrium fluctuations of the center of mass velocity lateral to the carbon wall in the considered systems (of finite size). Due to this large center of mass fluctuations (in comparison to the maximum flow velocities), profiles are often found to be unsymmetric even for time averages $\sim 1\,\text{ns}$. This is not due to a lack of equilibration time, but caused by equilibrium fluctuations of the stationary flow profile. Indeed, variations of the slope are much smaller, justifying the term 'stationary' even if two consecutive time averages might result in two distinctly different profiles. The difference disappears for infinite times or system sizes. In order to evade unfeasible long simulation times, we reduce the velocity vectors instead, by subtracting the center of mass velocity from all particle velocities.

The slab size dependence of slip length and viscosity is shown in Fig. 16. In addition, the friction coefficient calculated from these two quantities is plotted. Note first of all that the friction is constant and its value $\lambda \approx 1.2\frac{\text{Ns}}{\text{m}^3}$ is in excellent agreement with the outcome from the plug flow and the Green-Kubo measurements. The behavior of b and η under changing confinement is coupled: We found a simultaneous increase of the shear viscosity and the friction coefficient with decreasing slab size, while results from both experiments [81, 60] and simulations [59, 86] suggest that water keeps its bulk viscosity for system sizes that are several times the molecular

Couette flow results: viscosity, slip length, friction coefficient

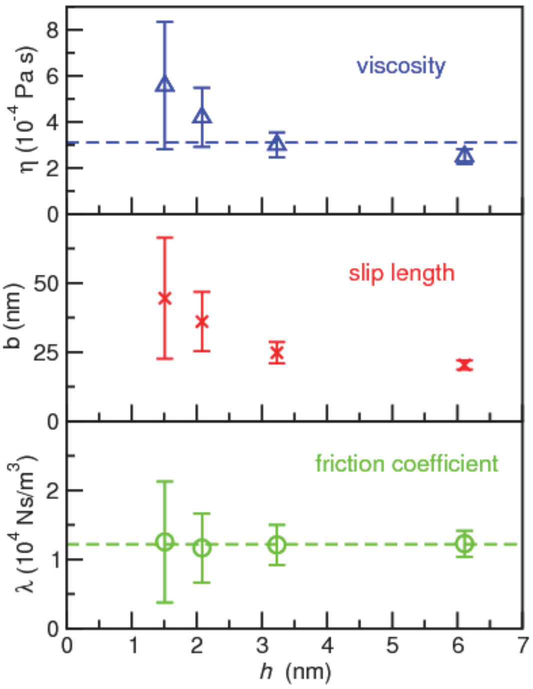

Figure 16: Shear viscosity $\eta = F/s$ and slip length $b = U/\dot{\gamma} - H/2$, extracted from Couette flow simulations (wall velocity U) in a graphene slab of size H, as a function of the slab size. The measurement is afflicted with considerable statistical errors due to fluctuations of the shear rate $\dot{\gamma}$ of the velocity profile and the shear force F. Within the errors, the viscosity is in good agreement with the bulk viscosity for the TIP3P water model (blue dashed line). For the friction coefficient $\lambda = \eta/b$ which is independent of H, we recover the same value (green dashed line) as in the flow and equilibrium measurements discussed in section 4.

diameter. Indeed, our measurements were afflicted by considerable statistical errors that were due to fluctuations of the velocity and the shear force. We can therefore not state any significant deviation from the bulk value of the TIP3P water model 0.32 mPa s, which was independently determined in an equilibrium bulk simulation using the Green-Kubo relation $\eta = \frac{\beta}{V} \int_0^\infty \mathrm{d}t \, \langle \sigma_{ij}(t) \sigma_{ij}(0) \rangle$ [35]. This value for the bulk viscosity is in good agreement with literature [30].

Further studies would be necessary to investigate water viscosity under confinement. But the question of confined liquid dynamics is a delicate one, from a theoretical as well as from an experimental point of view [86, 71, 85, 112, 55, 53]. A properly conducted study of water viscosity in nanopores is an interesting challenge, but goes beyond the scope of this work [7]. In the following, we just want to shortly demonstrate, that the relation between diffusion and viscosity under confinement is more complex than in bulk liquid.

5.1.2 Equilibrium measurement of the self diffusion coefficient

The bulk Stokes-Einstein relation predicts a dependance of the diffusion coefficient $D \propto \eta^{-1}$. From the shear measurements, we found an increasing viscosity for higher confinement. To compare the above determined viscosity with the prediction from the Einstein relation, we independently measured the diffusion coefficient via the

---

[7] Given that from the commonly used water models, TIP3P gives the worst result for the bulk water viscosity, we do not recommend to use this model for such an investigation

velocity autocorrelation function [8]

$$D_t = \int_0^\infty \mathrm{d}t \, \langle v_t(t) v_t(0) \rangle \, . \tag{20}$$

for the transverse velocity components. We find basically constant transverse diffusivity for the considered slab sizes 6.1 to 1.5 nm. The values that we find for the self diffusion coefficient lie all within 10% of the literature value for the TIP3P bulk self diffusion coefficient $D \sim 5.6 \frac{\mathrm{m}^2}{\mathrm{s}}$ at 300 K and 1 atm [68]. The fact that the water diffusivity under confinement is the same as in bulk is generally not the case. Bonnaud *et al.* observed, for example, a decreasing diffusivity of water in hydrophilic silica nanopores of width $1-2$ nm [9]. The constantly high mobility of the water molecules even under relatively high confinements is a further indication for the low friction at the graphite. If the friction at the wall is negligible, mobility of the molecules is not reduced despite the confinement. For a more quantitative discussion of diffusion in small pores we refer to studies of Saugey *et al.* [85], and also to Lauga and Squires [57].

5.2 Comparison to other groups' results

To discuss our results in comparison to the work of other groups, we may assume that the water viscosity keeps its bulk value for low confinements. Under this assumption, the decreasing friction is equivalent to an increasing slip length as it has been found in [98]. To give some order of magnitude, we take the literature value for the bulk viscosity of water $\eta \sim 0.9$ mPa s (298 K, 1 atm). Then the slip length amounts to $b \approx 80$ nm for water on graphene surfaces – for both TIP3P and SPC-E models. But in CNT with diameter < 2 nm, the MD results in Fig. 12 lead to a slip length of $b \gtrsim 250$ nm, comparable to the result by Holt *et al.* in the same conditions [38].

In order to tackle a quantitative comparison of simulation data, we look at the problem the other way round and translate the other groups' results into friction coefficients, whenever all the needed values are available. Our observation of plug flow is in accordance with references [34, 48]. The authors of reference [48] induced the water flow with a constant acceleration $a_{\mathrm{ext}} = 2.0 \times 10^{-3} \frac{\mathrm{nm}}{\mathrm{ps}^2}$. With this driving force, they get a stationary plug flow of $\sim 200 \frac{\mathrm{m}}{\mathrm{s}}$ in a CNT with radius 1.1 nm. Balance of forces $\lambda \mathcal{A} v_{\mathrm{slip}} = \rho V a_{\mathrm{ext}}$ allows to estimate the friction coefficient for their system to $\lambda \approx 5 \times 10^3 \frac{\mathrm{Ns}}{\mathrm{m}^3}$ (assuming homogeneous water density $10^3 \frac{\mathrm{kg}}{\mathrm{m}^3}$). The result is in good agreement with what we find for a tube of comparable diameter [9]. In reference [34] the driving force is not specified, which prevents a quantitative comparison. Thomas and McGaughey found a parabolic (although pretty flat) Poiseuille profile that enabled them to determine viscosity and slip length [98]. They performed flow simulations for different CNT sizes and found an increasing slip length and a

---

[8] In practice, we have to correct the velocities by subtracting the center of mass velocity (see Couette flow simulations for a discussion)

[9] We note, however, that the authors do not comment on linearity of the relation between applied forcing and stationary velocity. In our system, non-linear dependence of the friction on the slip velocity started to be noticeable above $50 \frac{\mathrm{m}}{\mathrm{s}}$. This makes a comparison of results for higher velocities somewhat ambiguous.

decreasing viscosity for decreasing radius [10]. Accordingly, the friction coefficient can be calculated directly for comparison to our results: It amounts to $\sim 2.7 \times 10^4 \frac{\mathrm{Ns}}{\mathrm{m}^3}$ on a flat graphene surface. No deviations from this graphene result are found for CNT radii larger than $\sim 2\,\mathrm{nm}$. For smaller tubes, friction continuously decreases to about 25% of the graphene value for tube radius 0.8 nm. This is in qualitative agreement with our results. Quantitatively, the friction is about the double from our values for graphene, as well as for CNT radius 0.8 nm. But while Thomas/McGaughey predict curvature influence only for tube radii $< 2\,\mathrm{nm}$, we find considerable deviations from the flat case for radii as large as 5 nm. Note, that Thomas and McGaughey use not a 3-site model, but TIP5P, together with Werder's *et al.* parameters for oxygen-carbon interaction. Furthermore, we foster some reservations about the exact procedure that is used in their work to measure η and b, because it relies on the validity of the *bulk* Stokes-Einstein relation $\eta = k_\mathrm{B}T/(3\pi\sigma D_z)$, which is not generally true under confinement [85] as was demonstrated above for the graphene slab geometry. Instead of extracting both parameters from the velocity profile, Thomas/McGoughey determined the viscosity via the self diffusion Eq. (20). The authors illustrate themselves the difference in an example for tube radius 1.6 nm: From a 2-parameter-fit of the profile, they get $\eta = 0.42\,\mathrm{mPa\,s}$ and $b = 24\,\mathrm{nm}$, while the viscosity calculated from the Einstein relation with the translational diffusion coefficient amounts to $0.72\,\mathrm{mPa\,s}$. With η set to the second value, a 1-parameter-fit of the velocity profile gives $b = 41\,\mathrm{nm}$. It is interesting to see, that both cases result in the same *friction coefficient*. Eventually, this indicates that the above discussed results concerning friction are independent of the evaluation procedure, and suggests again that friction is the relevant parameter controlling the flow behavior, when the flow profile tends to plug flow $v \propto (\lambda R)^{-1}$.

In conclusion, we emphasize that a most convenient parameter to compare MD simulation results for the water/graphite boundary condition is the friction coefficient. We find a qualitative and semi-quantitative agreement with the corresponding numerical studies on water/CNT systems performed by other groups [34, 48, 98]. A comparison of simulation results in terms of slip length is much more delicate, because it depends not only on the interface friction, but also on the liquid viscosity. In situations of large slippage, a reliable measurement of the viscosity is difficult. Furthermore, while results for the friction coefficient agree surprisingly well for different water models the bulk viscosity is largely model dependent (SPC-E: $\eta = 0.73\,\mathrm{mPa\,s}$,TIP3P: $\eta = 0.32\,\mathrm{mPa\,s}$,TIP5P: $\eta = 0.70\,\mathrm{mPa\,s}$, experiment:$\eta = 0.90\,\mathrm{mPa\,s}$[30]). On top of that, to our knowledge, no model-specific systematic examination of viscosity in confinement exists. Finally, one study, that has not been mentioned in this comparative part yet, is the original work of Hummer *et al.*, who observe a quasi-frictionless motion of single-file water in (6,6) CNT [49]. Our results support the idea of zero friction in this system.

Altogether, these results provide a strong support for reported experimental flow enhancement of 10^2 to 10^3, as stated by Holt *et al.* [38]. They are also in agreement with the flow enhancement of the order of magnitude 10 which was found by Whitby

---

[10] Mean flow velocities in this study are low (about $10\frac{\mathrm{m}}{\mathrm{s}}$); linearity can be safely assumed.

et al. for water flow in carbon nanopipes with 44 nm diameter [110]. Note, however, that our results do not agree with the experimental measurements performed by Majumder *et al.* [67]. While they reported on a water flow enhancement of $> 10^4$ for CNT membranes with pore sizes ~ 7 nm, our simulations resulted only in flow rates that were about 10^2 times larger than expected for the no-slip boundary condition under the same conditions.

6 Incompatibility of the curvature dependent friction coefficient with the common slip models

The first step to understand the observed behavior of the friction coefficient consists of exploring parameters that have formerly been found to influence the slip length either in simulations or experimentally. Such parameters are

1. pressure variation due to curvature of the water/carbon interface
2. changing properties of the interface water, such as the density (layering) characterized by the depletion length
3. or a change in the liquid structure due to confinement

In this section, we discuss the behavior of these properties in the different systems presented above. And, one by one, we discard them as possible explanations for the curvature effect, since we find indeed that none of the mentioned properties correlate with the curvature dependence of the friction coefficient.

6.1 Normal pressure

While the tangential pressure $p_\mathrm{T} = 1$ atm is the same in all simulations, the normal force on the carbon wall is curvature dependent due to the liquid solid interface tension γ_ls:

$$p_\mathrm{N}(R) = p_\mathrm{T} - \frac{\gamma_\mathrm{ls}}{R} \tag{21}$$

We observed a strong decrease of the normal force with the CNT radius, leading to large negative p_N (up to about $-1000\,\mathrm{atm}$ for the smallest radius). This corresponds to an interface tension of $\gamma_\mathrm{ls} \approx 0.07\frac{\mathrm{N}}{\mathrm{m}}$ (Fig. 17, left). In numerical studies of simple liquids it was found previously that a variation of p_N changes the properties of water confined between two hydrophobic walls (slab geometry) [27]; furthermore lower pressure was found to result in lower friction [2].

We checked the pressure dependence of the friction coefficient independently for zero curvature. For this we prepared systems of water confined between two graphene slabs at different pressures between −1000 atm and 500 atm. The pressure was controlled as described in section 4.3. The results are shown in in the right plot of Fig. 17: No change of the friction coefficient was observed in the range from $-500\,\mathrm{atm}$ to $500\,\mathrm{atm}$, and only a small decrease for even higher negative pressure $p = -1000\,\mathrm{atm}$.

We conclude that the decreasing normal force in CNT is not responsible for the curvature dependence of the friction coefficient. Additionally to the graphene slab simulations, we checked this result for one CNT with radius $R = 1.02\,\mathrm{nm}$ at $p_\mathrm{T} = 500\,\mathrm{atm}$ and $-500\,\mathrm{atm}$ and the obtained result for the friction coefficient differed less than 15% and 5%, respectively.

Friction coefficient and normal force

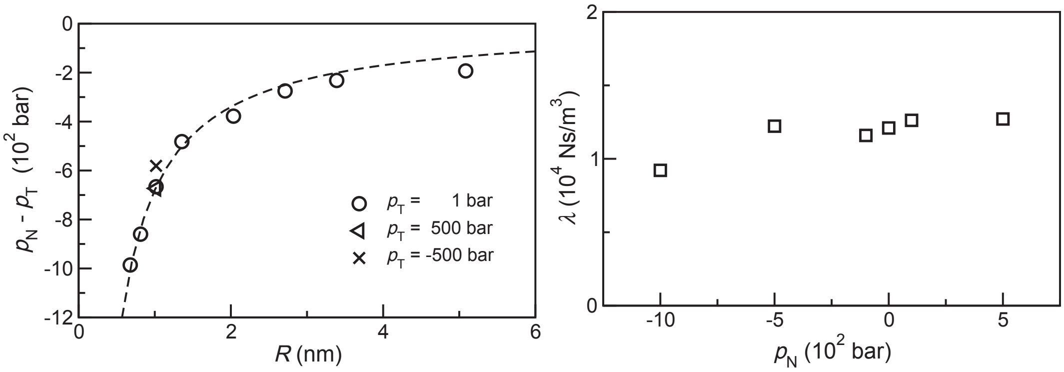

Figure 17: *Left:* Difference of normal and tangential pressure in a CNT of radius $R = 1.02\,\mathrm{nm}$. For increasing curvature the pressure normal to the CNT wall is reduced about $10^2 - 10^3$ atm due to the liquid-solid surface tension. A fit $p_\mathrm{N}(R) - p_\mathrm{T} = -\frac{\gamma_\mathrm{ls}}{R}$ (dotted line) gives $\gamma_\mathrm{ls} \approx 0.07\frac{\mathrm{N}}{\mathrm{m}}$ for the water graphene surface tension. *Right:* Friction coefficient λ for water in a graphene slab ($H \approx 2.5\,\mathrm{nm}$) for varying pressure. For pressure between $[-1000;\ 500]$ atm, no significant change in friction was observed. Therefore, the pressure drop at the CNT wall due to surface tension can not explain the observed curvature dependence of the friction coefficient.

Radial density profile and potential depth

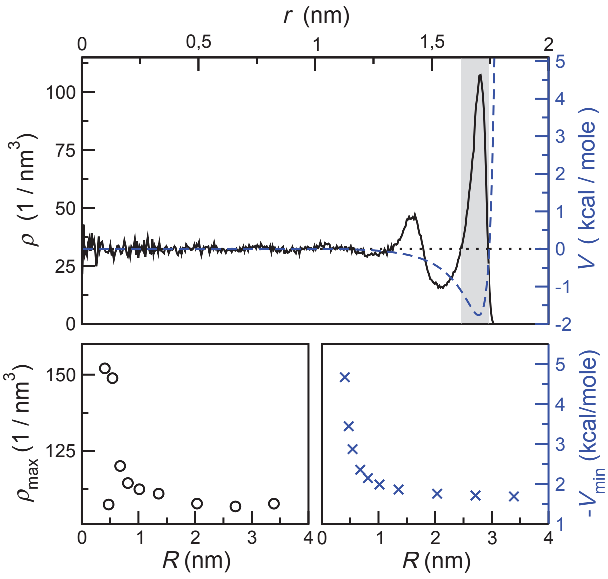

Figure 18: Density profile and potential for TIP3P water in armchair CNT. *Upper plot*: radial density function of oxygen and potential energy $V(r)$ of one oxygen atom positioned at $(r; \theta = 0, z = 0)$ for $R = 2.03\mathrm{nm}$. The contact density increases along with the curvature (*lower left*) due to the deepening of the potential well (*lower right*). One exception is the $(7,7)$ CNT ($R = 0.48$), where the maximum density is strongly reduced due to size exclusion: two water molecules barely fit in the cross section inhibiting the formation of a true interface layer. But the tube is still too large to impose a real single file. In this intermediate situation, water molecules are distributed almost equally over the tube cross section which leads to a smaller *maximum* density.

6.2 Wetting behavior: depletion and contact angle

It has been proposed, that water inside CNT has actually a non-wetting behavior [54], and that a depletion area between the carbon wall and the first water layer is responsible for the low friction [48]. An empirical correlation between slip length and contact angle $b \propto (1 + \cos\theta)^2$, or alternatively between slip and depletion length $b \propto \delta^4$ has been shown to hold for hydrophobic planar surfaces [40, 86]. In this paragraph, we test this prediction for the investigated water/CNT systems, by comparing the measured curvature dependence of the friction coefficient to the depletion length.

To start with, we have a look at the upper plot in Fig. 18, which shows the potential energy $V(r)$ of one oxygen atom positioned at $(r, \theta = 0, z = 0)$ due to its interaction with all carbon atoms, and the radial density profile of oxygen $\rho(r)$. The oxygen-carbon interaction results in a region of highly increased water density next to the wall (gray background). We refer to this region of molecular thickness as to the 'first water layer'. From the outside to the inside, the first layer is followed by a second layer and the bulk region. The distance between the first layer and the carbon wall ($\sim \sigma_{\text{oc}} = 0.33\,\text{nm}$) is independent of the CNT radius. For decreasing tube radii down to $R \approx 1\,\text{nm}$, the potential well deepens slightly (lower right plot) which consequently leads to an equally slight increase of the contact density (lower left). For even smaller radii $R < 1\,\text{nm}$ the potential well deepens considerably. The small diameter allows only for four water molecules or less. Therefore these tubes do not contain bulk water.

The layering of a fluid near a planar wall as it can be seen in Fig. 18 can be quantified by the depletion length δ, which is defined as the integrated density variation. For a graphene slab with carbon positions $z = \pm\frac{H}{2}$, the depletion length is

$$\delta_{\text{planar}} = \frac{1}{2}\int_{-\frac{H}{2}}^{\frac{H}{2}} \mathrm{d}z \, \left(1 - \frac{\rho(z)}{\rho_{\text{bulk}}}\right) \tag{22}$$

and for a CNT with radius R we define

$$\delta_{\text{cylindric}} = \frac{1}{R}\int_{0}^{R} \mathrm{d}r \; r \, \left(1 - \frac{\rho(r)}{\rho_{\text{bulk}}}\right). \tag{23}$$

According to these definitions, the bulk region $\rho = \rho_{\text{bulk}}$ should not contribute to the depletion length, but in practice, statistical density fluctuations in MD simulations add to the result. To reduce the impact of fluctuations, we did not include the bulk region in the calculation of the depletion length. The values we thus get for the depletion length with the bulk density $\rho_{\text{bulk}} = 32.4$ molecules/nm^3 are shown in Fig. 19.

We do not observe a correlation between the friction coefficient and the depletion length. And while we expect the slip length $b \propto 1/\lambda$ to increase – assuming constant η –, the depletion length decreases slightly with the CNT radius (less than 10% in the range from 5 to 1 nm). This is in contradiction to the mentioned prediction $b \propto \delta^4$. In addition, the result for tubes of big diameters do not match the result for graphene, which would be expected when the curvature gets small. Furthermore, the

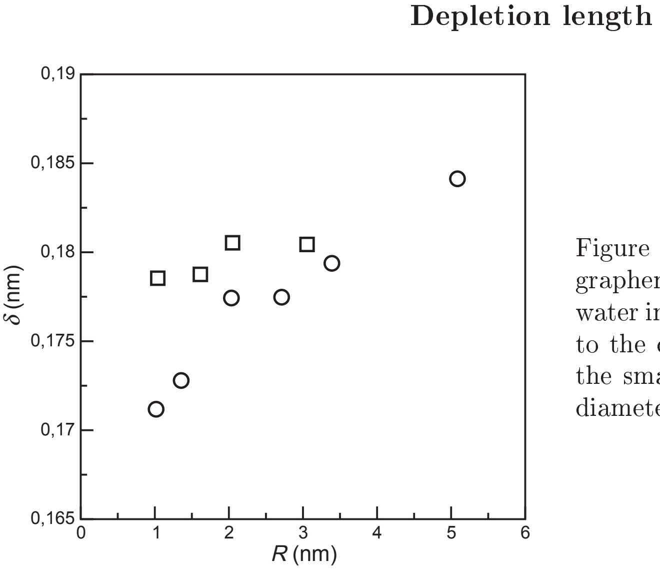

Figure 19: Depletion length of water in graphene slabs of size $H = 2R$ (□) and of water in CNT with radius R (∘) - according to the definitions Eq. (22) and (23). Note the small variation of δ over the range of diameter studied.

depletion length is not a good parameter to characterize the water CNT interaction for high confinement $R < 1\,\mathrm{nm}$, because no bulk density can be defined.

Finally, comparing the friction obtained for both water models, TIP3P and SPC-E, we see the same curvature dependent behavior in the CNT, and a fair quantitative agreement for the graphene slabs. But simulations of a water droplet on a graphene sheet reveal a very different contact angle: 57° for TIP3P/AMBER and 95° for SPC-E/Werder parameters.

In fine, a theory based solely on the water/carbon interaction energy – like the contact angle or the depletion length – can not explain the observed behavior of the friction coefficient in water/graphite systems.

6.3 Interface water structure

Last but not least, we considered that the increasing wall curvature might induce a change of the spatial arrangement of the water molecules in close proximity to the wall. A restructuring could in turn influence the water/carbon friction due to a changing commensurability between water molecules in the first layer and the CNT wall. We quantify ordering in the first water layer with the 2-dimensional static structure factor

$$\begin{aligned} S(\mathbf{q}) &= \frac{1}{N}\left\langle \sum_{j=1}^{N}\sum_{l=1}^{N} \exp(\mathrm{i}\mathbf{q}\cdot(\mathbf{x}_l - \mathbf{x}_j)) \right\rangle \qquad (24) \\ &= \frac{1}{N}\left\langle \left(\sum_{j=1}^{N}\cos(\mathbf{q}\cdot\mathbf{x}_j)\right)^2 + \left(\sum_{j=1}^{N}\sin(\mathbf{q}\cdot\mathbf{x}_j)\right)^2 \right\rangle \end{aligned}$$

where $\mathbf{x}$ is tangential to the water/carbon interface. In case of CNT, this means $\mathbf{x} = (r_\mathrm{o}\theta, z)$ with the radial position r_o of the first layer (position of density maximum in Fig. 18). This can be imagined as calculating the 2D structure factor of the 'unrolled' water layer. 'Unrolled' means that the positions of all oxygen atoms in the first layer are mapped according to

$$\mathbf{r} = \begin{pmatrix} r \\ \theta \\ z \end{pmatrix} \longrightarrow \mathbf{x} = \begin{pmatrix} s = r\theta \\ z \end{pmatrix} \tag{25}$$

on the euclidean plane. The structure factor $S(\mathbf{q})$ for the interfacial water layer at a plane graphene sheet is shown in the left part of Fig. 22. It is found to be isotropic and independent of confinement for slab sizes about three times the molecular diameter and larger. Surprisingly, we find the same characteristics for the structure of the interface water in CNT: The structure factor is isotropic $S(\mathbf{q}) = S(q)$ $(q = |\mathbf{q}|)$ and it is not affected by confinement for CNT radii above 0.8 nm. This is exhibited in the middle plot of Fig. 22, where the structure factor of oxygen atoms in the first water layer close to the surface is shown for various CNT radii. Consequently, the curvature dependence of the friction coefficient which is eminent even for tube radii as large as 3 nm can not stem from a rearrangement of the water molecules in the CNT due to confinement. Again, the water structure is not found to correlate with the friction coefficient decrease, the latter being already significant for large tubes.

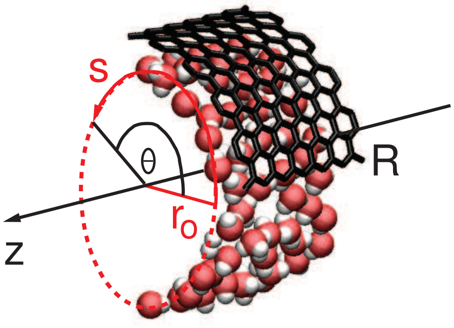

Figure 20:

A significant change in the structure factor was only observed for CNT diameter smaller than 1 nm. For the highest confinements, water molecules are forced to arrange in single file on the tube axis. This can be seen in the right plot in Fig. 22, where the one-dimensional structure factor in direction of the tube axis is shown for different radii.

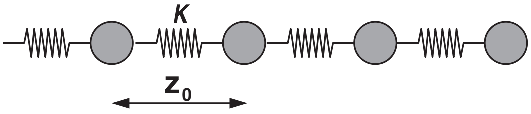

Figure 21: Bead-spring model

We note that the structure factor of single file water is identical to the structure factor of a bead-spring chain as it is sketched in Fig. 21: particles at equilibrium distance z_0 are coupled by a harmonic potential with spring constant κ.

The structure factor of this system reads

$$S(q) = \frac{1 - \mathrm{e}^{\frac{-q^2}{\beta\kappa}}}{1 - 2\mathrm{e}^{\frac{-q^2}{2\beta\kappa}} \cos(qz_0) + \mathrm{e}^{\frac{-q^2}{\beta\kappa}}} \tag{26}$$

with $\beta = 1/k_{\mathrm{B}}T$ (see appendix A for a derivation). A fit of this expression on the data for the two smallest tubes (fit parameters κ and z_0) gives the solid lines in the right plot of Fig. 22. The resulting values for z_0 coincide with the mean distance of two water molecules along z, given by the CNT length divided by the number of water molecules in the tube.

First water layer structure factor (TIP3P model)

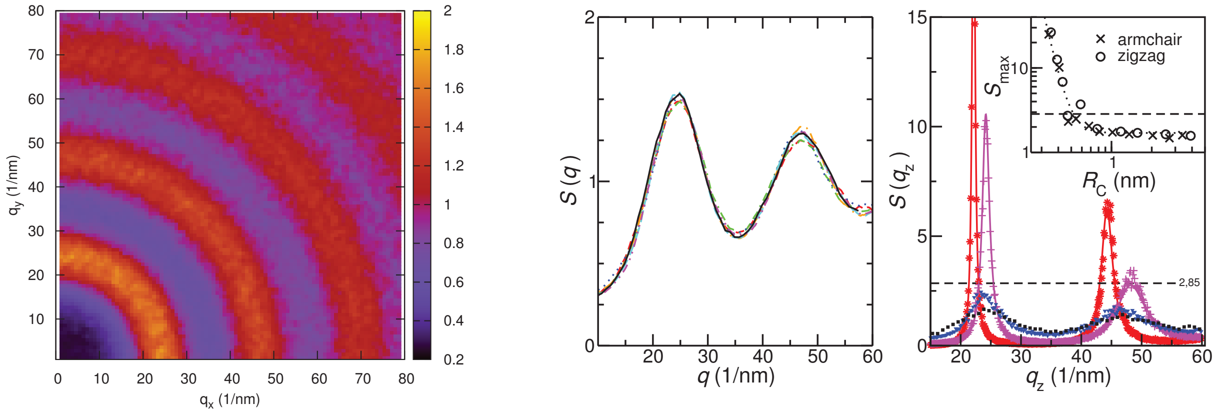

Figure 22: Structure factor of water in the first water layer close to the carbon surface (definition Eq. (25)). *left*: $S(\mathbf{q})$ for the water boundary layer on a plane graphene sheet. The water structure is isotropic; the SF is independent of the wave vector orientation. *middle*: $S(q)$ of water in the first layer, for the slab geometry and six armchair CNT with radii in the range 0.81 to 3.39 nm. For low confinement the SF is independent of the tube radius. *right*: $S(q_z)$ with wave vector q_z along the CNT length, within the smallest CNT with radii $R = 0.34\,\text{nm}$ (red), $R = 0.41\,\text{nm}$ (pink), $R = 0.48\,\text{nm}$ (blue) and $S(q)$ of the first water layer on graphene for comparison (black). Water in the two smallest tubes is arranged in single file. The lines correspond to a simplified 1D analytical model of the water structure (see Eq. (26)). *Inset:* Maximum value of the structure factor, measured at its first peak. The horizontal line with $S_{\max} = 2.85$ defines the onset of water crystallization according to the Hansen-Verlet criterion [36].

6.4 Conclusion

In this section, we evaluated our simulations according to several parameters that we expected to have an impact on the water/CNT friction: normal pressure, depletion, water structure, etc. Surprisingly, none of the considered factors was found to be at the origin of the curvature dependence of the friction coefficient. On the contrary, the friction coefficient was found to be independent of pressure variations in a range over three orders of magnitude. Wetting properties did not play a crucial role either – TIP3P and SPCE water model have a very different contact angle on graphene, but the friction coefficient exhibits nevertheless a quite similar behavior. Finally, properties of the interface water like the depletion length and the static structure factor barely change in low confinement.

At this point, the reason for the observed friction decrease in CNT is thus still completely unclear. This is why the following part is dedicated to a theoretical investigation of the friction coefficient, with the aim to reveal the physical mechanisms controlling the liquid/solid friction force in the considered systems.

Part III

Theoretical understanding of the curvature dependent friction coefficient

In this part, a theoretical description of the water/carbon friction is proposed. Starting point for this study will be the Green-Kubo expression Eq. (16). An analytic approach will then lead us to an approximate expression for the friction coefficient that consists solely of interfacial properties, that is to say properties of the first water layer. Evaluation of our simulation results according to this description will show that it captures the observed curvature dependence of the friction. This will then allow us to identify the mechanisms at the origin of this behavior, namely low structure commensurability and smoothing of the wall potential. These two effects concur to the extraordinarily high flow rates for water in CNT. Furthermore, understanding the relevant physical processes on a molecular level, we make predictions based on our theoretical expression for the friction coefficient in other systems. Finally, we use again MD simulations to confirm these predictions.

Contents

7 Approximative expression for the friction coefficient 65

7.1 Distinction of 'static' and 'dynamic' part in the Green-Kubo expression . . . 65

7.2 Approximating the random mean squared force . . . 65

7.2.1 Low confinement (CNT diameter > 1.5 nm) . . . 67

7.2.2 High confinement (single file) . . . 68

8 Comparison of theory and simulations 70

8.1 Static origin of the curvature dependent friction (validation of the theory) . . . 70

8.2 Microscopic origin of the curvature dependence: understanding friction on a molecular level . . . 71

8.2.1 Low confinement . . . 71

8.2.2 High confinement . . . 74

9 Testing predictions 75

9.1 Changing wall structure without curvature - variations of the graphene lattice parameter . . . 75

9.2 Changing the carbon nanotube structure - zigzag chirality . . . 77

9.3 Non-linear behavior for large slip velocities . . . 83

10 Quantitative agreement between the rms force and its approximation 84

10.1 Neglect of second water layer . . . 84

10.2 Truncation of the force field Fourier expansion . . . 84

10.3 Projection of the first water layer . . . 86

7 Analytic derivation of an approximative expression for the friction coefficient

To get further insight into the physical mechanisms at play, we take a closer look at the Green-Kubo expression Eq. (16) for the friction coefficient. The chosen approach imitates the derivation of the approximate expression Eq. (6) for the slip length by Barrat and Bocquet [2] – adapted to the cylindric geometry of the CNT and the specificities of the water/graphite interface.

7.1 Distinction of 'static' and 'dynamic' part in the Green-Kubo expression

The GK expression may be first rewritten formally as

$$\lambda = \beta \tau_F \frac{\langle F^2 \rangle}{\mathcal{A}} \tag{27}$$

$\beta = 1/k_\mathrm{B}T$, defining the decorrelation time

$$\tau_F = \frac{1}{\langle F^2 \rangle} \int_0^\infty \mathrm{d}t \langle F(t)F(0) \rangle. \tag{28}$$

that characterizes the decay of the force-force autocorrelation function. Interestingly this time depends only very weakly on the CNT curvature in the weak confinement regime, as shown in Fig. 23. Typically it is on the order of 100 fs. In contrast, curvature has a strong influence on the static rms force. The variation of the friction coefficient λ on CNT curvature is found to directly correlate with the static rms force $\langle F^2 \rangle$, as shown in Fig. 24, both for water inside ('positive' curvature) and outside ('negative' curvature). Consequently, we investigate in the following the mean squared force $\langle F^2 \rangle$ to identify the physical effects at the origin of the curvature dependent friction.

7.2 Approximating the random mean squared force

The water-carbon force can be written in the general form

$$\mathbf{F} = \int \mathrm{d}^3 r \; \rho(\mathbf{r}) \mathbf{f}(\mathbf{r}) \quad \text{with } \mathbf{f}(\mathbf{r}) = -\nabla V(\mathbf{r}) \tag{29}$$

where $V(\mathbf{r})$ denotes the potential energy of one oxygen atom at position $\mathbf{r}$ due to interactions with all wall atoms. Starting from Eq. (29) an approximate expression for the rms force is developed in the following.

In order to simplify Eq. (29) for the force, we have to distinguish between the different topologies in low and high confinement - bulk water and layering in the former, single file structure in the latter case. We first concentrate on the low confinement case, which is closer to the plane geometry considered in reference [2].

Static rms force and decorrelation time

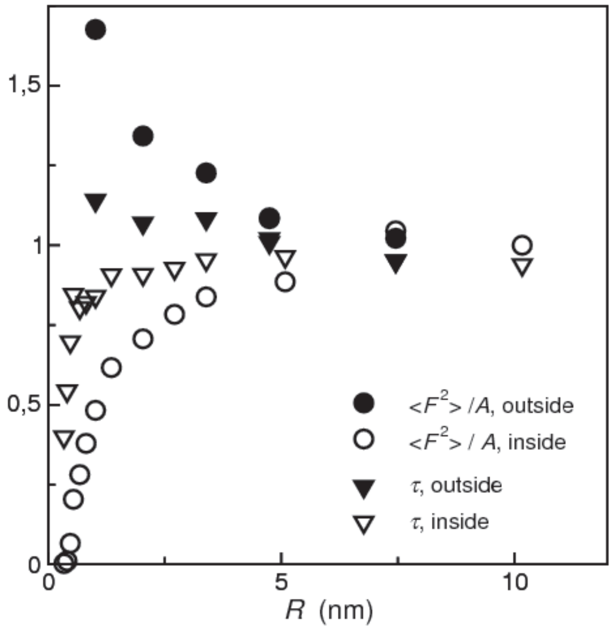

Figure 23: Static rms force $\langle F^2 \rangle$ and decorrelation time τ_F for water inside and outside CNT of radius R (normalized on the values for graphene).

Friction coefficient vs. static rms force

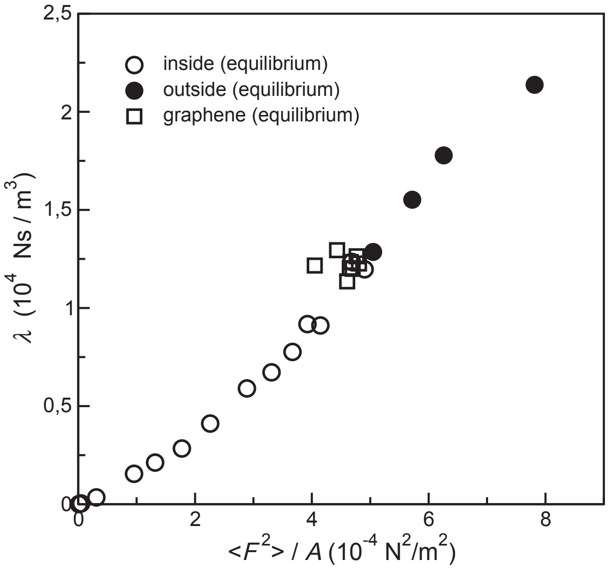

Figure 24: Functional dependence of the friction coefficient λ versus the static rms force $\langle F^2 \rangle$. This plot gathers results for all confinements and geometries: ○ water inside CNT; • water outside CNT; □ slab geometry. The friction coefficient is directly correlated with the rms force. The curvature dependence of the friction is mainly a static effect. Deviations from a linear relationship $\lambda \propto \langle F^2 \rangle$ due to changing decorrelation times are small.

7.2.1 Low confinement (CNT diameter $> 1.5\,\mathrm{nm}$)

Keeping in mind the density profile in Fig. 18, we use that the main contribution to the force stems from the water molecules in the first layer to write

$$F \approx \int \mathrm{d}z \int \mathrm{d}s\ \partial_z V(r_\mathrm{o}, s, z) \tag{30}$$

where $r_\mathrm{o} = R \pm \sigma_\mathrm{oc}$ is the mean radial position of the water molecules in the first layer (inside or outside the CNT) and $s = r_\mathrm{o}\theta$. We further note that the periodicity of the oxygen-wall potential $V(s,z)$ at the radial position of the first layer is given by the projection of the carbon structure on the cylinder with radius r_o. The lattice vectors for the projected structure are

$$\begin{aligned} \mathbf{a}_+ &= \frac{l_0}{2}\begin{pmatrix} \sqrt{3}\frac{r_\mathrm{o}}{R} \\ 1 \end{pmatrix} \\ \mathbf{a}_- &= \frac{l_0}{2}\begin{pmatrix} \sqrt{3}\frac{r_\mathrm{o}}{R} \\ -1 \end{pmatrix} \end{aligned} \tag{31}$$

where $l_0 = \sqrt{3}d$ (carbon-carbon distance $d = 0.142\,\mathrm{nm}$) is the length of the lattice vectors for the graphene structure which is recovered in the limit $\frac{r_\mathrm{o}}{R} \to 1$. The corresponding reciprocal lattice vectors are

$$\begin{aligned} \mathbf{q}_+ &= q_0\begin{pmatrix} \frac{R}{\sqrt{3}r_\mathrm{o}} \\ 1 \end{pmatrix} \\ \mathbf{q}_- &= q_0\begin{pmatrix} \frac{R}{\sqrt{3}r_\mathrm{o}} \\ -1 \end{pmatrix} \end{aligned} \tag{32}$$

where $q_0 = 2\pi/l_0 \approx 25.55\,\mathrm{nm}^{-1}$. The resulting force field $f(s,z) = -\partial_z V$ for an oxygen atom in the first layer has the same periodicity. The potential $V(s,z)$ and the derivative $\partial_z V(s,z)$ for a plane graphene sheet are shown in Fig. 25. Expressing the force as a Fourier series and omitting higher orders (see Fig.37)

$$f\ (\mathbf{x} = (s,z)) \approx f_{q_\parallel}\left(\sin(\mathbf{q}_+ \cdot \mathbf{x}) - \sin(\mathbf{q}_- \cdot \mathbf{x})\right) \tag{33}$$

the mean force can in first approximation be written as

$$\begin{aligned} \left\langle F^2 \right\rangle &= \int \mathrm{d}^2\mathbf{x} \int \mathrm{d}^2\mathbf{x}'\ f(\mathbf{x})f(\mathbf{x}')\left\langle \rho(\mathbf{x})\rho(\mathbf{x}')\right\rangle \\ &\approx f_{q_\parallel}^2 \int \mathrm{d}^2\mathbf{x} \int \mathrm{d}^2\mathbf{x}'\ \left(\sin(\mathbf{q}_+ \cdot \mathbf{x}) - \sin(\mathbf{q}_- \cdot \mathbf{x})\right) \times \\ &\qquad \left(\sin(\mathbf{q}_+ \cdot \mathbf{x}') - \sin(\mathbf{q}_- \cdot \mathbf{x}')\right)\left\langle \rho(\mathbf{x})\rho(\mathbf{x}')\right\rangle \\ &= \frac{1}{2}N_1\left(S(\mathbf{q}_+) + S(\mathbf{q}_-)\right). \end{aligned} \tag{34}$$

The last equality holds due to the relation $\langle \tilde{\rho}(\mathbf{q})\,\tilde{\rho}(-\mathbf{q})\rangle = N_1 S(\mathbf{q})$ where N_1 is the number of molecules in the first water layer. Finally, using the isotropy of the water

Potential energy landscape for water next to graphene and CNT

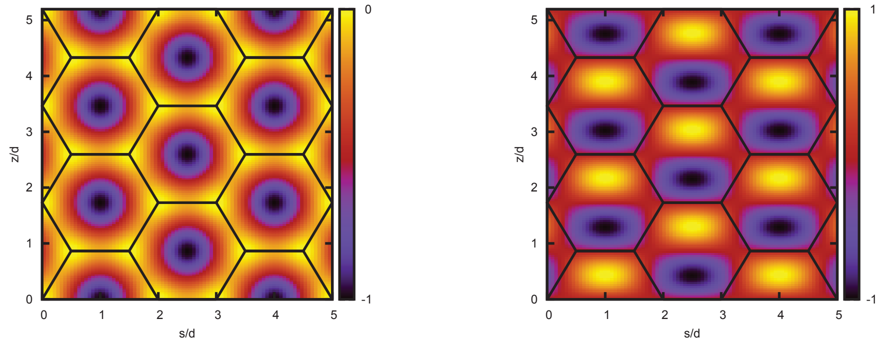

Figure 25: Potential landscape $V(s,z)$ (*left*) and its derivative $\partial_z V$ (*right*) for one oxygen atom at the distance σ of a graphene plane (distances are normalized by the C-C-distance $d = 0.142\,\mathrm{nm}$)

structure factor and the length of the reciprocal lattice vectors $q_+ = q_- =: q_\|$, we find

$$\frac{\lambda}{\beta\tau_F} = \frac{\langle F^2 \rangle}{\mathcal{A}} \approx \frac{N_1}{\mathcal{A}} f_{q_\|}^2 S(q_\|). \tag{35}$$

This expression constitutes a microscopic description of the water carbon friction. It relates the friction coefficient via the mean squared force to the

1. average number of water molecules in the first layer N_1 per interface area; in other words the *surface density* $\frac{N_1}{\mathcal{A}}$
2. force field amplitude $f_{q_\|}$ (see Eq. (33)) which characterizes the *roughness* of the lateral interaction potential
3. 2-dimensional structure factor $S(\mathbf{q})$ of the first water layer, evaluated at the main reciprocal lattice vector $q_\|$ of the water/wall potential at the position of the first layer

All quantities in the expression above are i) characteristics of the interface, and ii) easily accessible in MD simulations.

7.2.2 High confinement (single file)

With increasing confinement, the water molecules get more and more ordered along the tube axis, up to the point where they build a single file chain for the two smallest tubes ($R = 0.34$ and $0.41\,\mathrm{nm}$). Hence an evaluation with the structure factor defined in Eq. (25) is not possible, because the range of the angular coordinate $s = \theta r_o$ becomes too small, from a few molecular diameters to $s \approx 0$ for water arranged in single file – the two dimensional water layer is reduced to a one dimensional chain.

To quantify the structuring that occurs hereby, we calculated the structure factor in z-direction:

$$S(q) = \frac{1}{N} \left\langle \sum_{j=1}^{N} \sum_{l=1}^{N} \exp(\mathrm{i}q(z_l - z_j)) \right\rangle \tag{36}$$

Structure factors for $R = 0.34$, 0.41 and 0.47nm are compared in the right plot of Fig. 22. The inset shows the increase of the first peak for strong confinements. For the single file cases, the maximum exceeds the crystallization criterion $S = 2.85$ of Hansen and Verlet [36].

Now coming back to the rms force, it turns out that for the one dimensional case of a water chain in the middle of the CNT, $\langle F^2 \rangle$ takes the same form as in expression (35). This can be derived in complete analogy to the case of a two dimensional water interface layer: Water molecules situated on the tube axis are subject to a one dimensional periodic force field

$$f(z) = f_{q_0} \sin(q_0 z) \tag{37}$$

where the periodicity is $q_0 = 2\pi/\sqrt{3}d = 25.5\ \mathrm{nm}^{-1}$. The result for the rms force is then

$$\langle F^2 \rangle = \frac{1}{2} \frac{N}{\mathcal{A}} f_{q_0}^2 S(q_0). \tag{38}$$

8 Comparison of theory and simulation results for the friction coefficient

In the last section, an approximate expression for the friction coefficient was deduced, that connects water/graphite friction to static properties of the water interface layer. The next step, which will be taken in this section, consists of verifying the relevance of this description on the basis of the simulation results from section 4. Evaluating the simulations according to Eq. (35) shows that this expression captures in fact the observed curvature dependence of the friction coefficient. After establishing the pertinence of the theoretical model, the three contributions to the mean squared force will be considered individually. This will lead to a concrete picture of the physical processes at the origin of the low friction.

8.1 Static origin of the curvature dependent friction (validation of the theory)

In order to test the prediction of Eq. (35) for the friction coefficient, we calculate the three contributions to the rms force – contact density $\frac{N_1}{\mathcal{A}}$, structure factor $S(q_\parallel)$ and potential roughness $f_{q_\parallel}$.

The contact density is given by the ratio of mean number of molecules in the first layer N_1 and the contact area $\mathcal{A}$. We get N_1 from a time average of the number of oxygen atoms in the interface area defined in Fig. 18. The contact area is calculated with the effective tube radius (definition Eq. (18)). The water structure factor is calculated according to Eq. (25) and averaged over a few hundred configurations. Finally, the force field at the position of the first layer is the sum of the pair interactions between one oxygen atom at position $\mathbf{r} = (r_\text{o}\cos\theta; r_\text{o}\sin\theta; z)$ and all carbon atoms $\mathbf{R_i} = (R\cos\theta_i; R\sin\theta_i; z_i)$

$$f(\theta, z) = -\sum_i \partial_z U_\text{LJ}\left(\mathbf{R}_i - \mathbf{r}\right) \tag{39}$$

where U_LJ is the Lennard-Jones potential (given in Eq. (10)).

This force field is calculated for a discrete sample of oxygen positions $\mathbf{r}_n$ which is then used in the next step to calculate the Fourier coefficient of the wave vector $\mathbf{q}_\pm$ according to

$$f_{q_\parallel} = \sum_n f\left(\theta_n, z_n\right) \exp\left(\mathrm{i}\mathbf{q}_\pm \cdot \{r_\text{o}\theta_n; z_n\}\right) \tag{40}$$

We can now compare the measured rms force and the derived approximation $\frac{N}{\mathcal{A}} f_{q_\parallel}^2 S(q_\parallel)$. This comparison, shown in Fig. 26, reveals a proportional relationship. Eq. (35) catches all effects that lead to the curvature dependence of the rms force and thus of the friction coefficient.

The derived expression for the friction coefficient allows to investigate the origin of this curvature dependence on a molecular level.

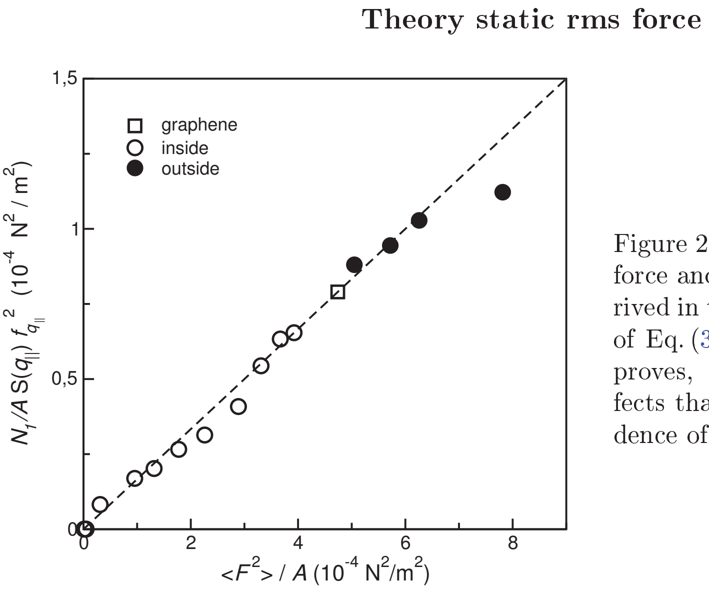

Figure 26: Correlation between the rms force and the theoretical expression derived in this section, the right hand side of Eq. (35). As the linear relationship proves, this expression catches all effects that lead to the curvature dependence of the rms force.

8.2 Microscopic origin of the curvature dependence: understanding friction on a molecular level

After identifying the relevant physical properties influencing the water-carbon friction, we now want to understand in detail what effects cause the friction to diminish with the CNT radius. We find that all three factors – contact density $\frac{N_1}{\mathcal{A}}$, roughness $f_{q_\|}$ and commensurability factor $S(q_\|)$ – contribute to the curvature dependent behavior of the rms force, as can be seen in Fig. 30. However, while there clearly exists an inverse correlation for low confinement (higher $\frac{N}{A}$, $f_{q_\|}$, $S(q_\|)$ for lower curvature and vice versa), the situation seems less coherent for higher confinement (small R). In the following, both regimes are discussed separately.

8.2.1 Low confinement

In low confinement, all three relevant factors change monotonously with curvature. This is shown in Fig. 27. In the following, the origin of the curvature induced changes of contact density, wall roughness and structure commensurability will be discussed one by one.

Contact density In section 6, we mentioned that higher curvature leads to a somewhat deeper potential well at the position of the first water layer and therefore to a slightly higher density in the first water layer (Fig. 18). Now, Fig. 27 states a decreasing contact density. This is not a contradiction, but a simple geometric effect: The maximum of the radial density profile really increases (but not much). But what we call *contact* density is the number of molecules per interface area $\frac{N_1}{\mathcal{A}}$ and it decreases with the radius, because the interface area $\mathcal{A} = 2\pi\ (r_\mathrm{o} + \sigma/2)\ L_\mathrm{z}$ increases in relation to $2\pi r_\mathrm{o}$.

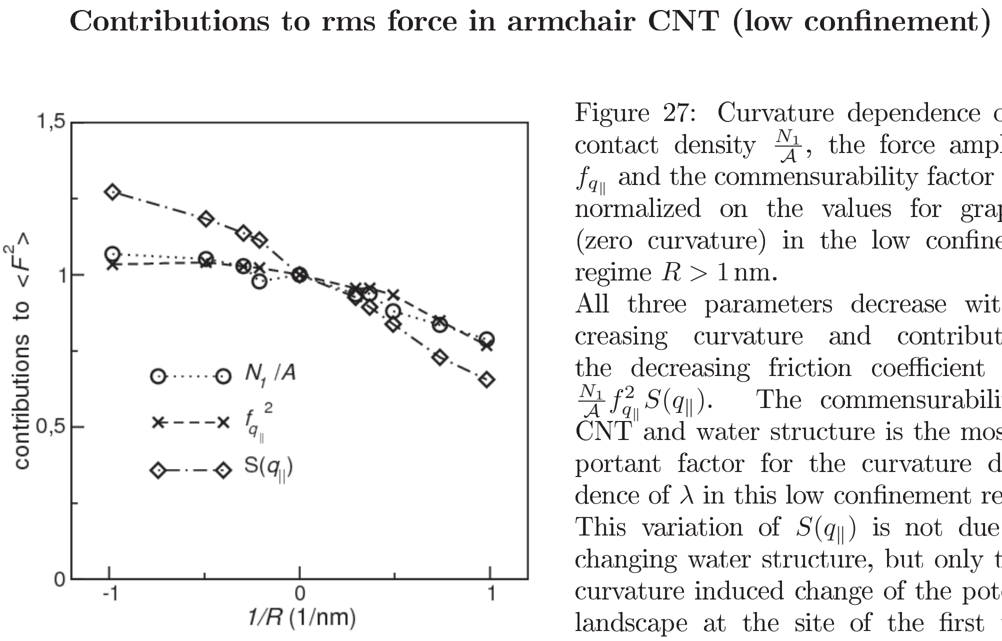

Figure 27: Curvature dependence of the contact density $\frac{N_1}{A}$, the force amplitude $f_{q_{\|}}$ and the commensurability factor $S(q_{\|})$ normalized on the values for graphene (zero curvature) in the low confinement regime $R > 1\,\text{nm}$.
All three parameters decrease with increasing curvature and contribute to the decreasing friction coefficient $\lambda \propto \frac{N_1}{A} f_{q_{\|}}^2 S(q_{\|})$. The commensurability of CNT and water structure is the most important factor for the curvature dependence of λ in this low confinement regime. This variation of $S(q_{\|})$ is not due to a changing water structure, but only to the curvature induced change of the potential landscape at the site of the first water layer.

Potential roughness Curvature changes the periodicity of the oxygen-wall potential as well as its roughness: For the first water layer inside a CNT, higher curvature smoothens the potential in lateral direction to the wall, so that the force amplitude $f_{q_{\|}}$ decreases. On the other side, the potential outside the CNT gets rougher. An example for this smoothing of the oxygen-wall potential is displayed in Fig. 28.

Structure (in)commensurability In this low confinement regime, the biggest change with curvature takes place for the structural contribution $S(q_{||})$. The water structure for water in CNT and graphene slabs was already discussed in 6. The structure factor was found to be isotropic and independent of curvature in low confinement. This holds equally true for water outside CNT. However, the key point is that one estimates $S(q)$ at a confinement dependent wave vector $q_{||}(R)$. The structural contribution $S(q_{||})$ to the rms force is crucial, even for small wall curvature. Again, this is not due to a change in the spacial arrangement of the water molecules. But, the curvature causes a deformation of the oxygen-wall potential for a molecule in the first water layer compared to the potential next to a plane graphene sheet, as it can be seen in Fig. 28.

The unit cell of the periodic potential, given by the lattice vectors $\mathbf{a}_{\pm}$ (Eq. (31)), is compressed (positive curvature) or expanded (negative curvature) in the direction perpendicular to the tube axis. In Fourier space, this leads to an elongation and shortening, respectively, of the wave vector $q_{||}$. So the structure factor of the first water layer which figures in Eq. (35) and which is itself independent of the CNT radius, has to be evaluated at another wave vector for each radius. Concretely, the radius dependent length of the reciprocal lattice vector $q_{||}$ (see Eq. (32)) is given by

Oxygen-wall potential of the first water layer for graphene and CNT

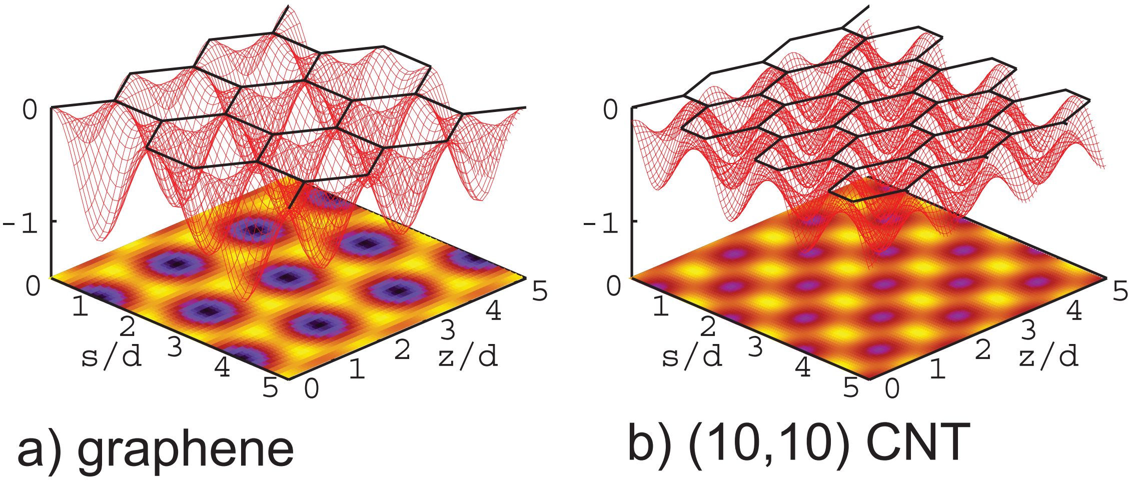

a) graphene

b) (10,10) CNT

Figure 28: Interaction energy landscape (shifted and normalized) felt by a single water molecule in the first layer close to the carbon wall, for water in a graphene slab (*left*) and inside a CNT with radius $R = 0.68\,\mathrm{nm}$ (*right*). The potential is computed from a direct summation of the water-carbon interaction at a distance σ from the wall; In case of zero curvature, the periodicity of the potential is identical to the graphene structure; for the CNT, the periodicity is given by the *projection* of the wall structure on the position of the first water layer. Curvature also induces a smoother potential inside the CNT.

Radius dependent q-vector

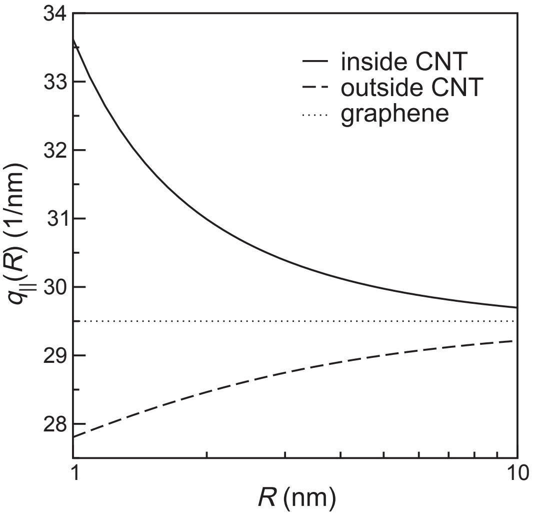

Figure 29: Radius dependence of the absolute value of the wave vectors $|\mathbf{q}_+| = |\mathbf{q}_-| = q_{\|}$. $\mathbf{q}_\pm$ are the reciprocal lattice vectors defining the periodicity of the water-carbon potential for a water molecule in the first layer near a graphitic wall. They change with curvature since bending the wall leads to a deformation of the potential landscape for water in its proximity. Inside or outside CNT, the periodicity of the energy landscape for water in the first layer is given by the projection of the carbon structure on the first layers position. $q_{\|}$ increases with curvature for water inside and decreases for water outside an armchair CNT.

$$q_{\|}(R) = \frac{2\pi}{l_0}\sqrt{\frac{R^2}{3r_{\mathrm{o}}^2}+1} \tag{41}$$

For water inside and outside CNT with radius $R > 1$nm, $q_{\|}(R)$ covers an interval $[27.8; 33.5\,\mathrm{nm}^{-1}]$ (Fig. 29). This corresponds to a range of large variations of the water structure factor between the first maximum and the following minimum.

8.2.2 High confinement

In the high confinement regime the role of contact density, roughness and structure for the rms force are somewhat different from what was just discussed for low confinement. On the one hand, the vector q_0 defining the oxygen-wall potential's periodicity is radius independent, because it is oriented in axial direction. On the other hand, the structure factor in z-direction changes drastically with the tube radius due to the rearrangement of water molecules in high confinement. Both facts combined lead to a rather unsystematic behavior of the structural contribution $S(q_0)$. Furthermore, we note that the strong confinement also has an impact on the water dynamics: It influences the correlation time τ that, according to Eq. (35), also directly affects the friction coefficient. But the dominating factor which leads to frictionless motion for single file water is the disappearing roughness of the potential, as it can be seen in the comparison of all these contributions in Fig. 30.

Contributions to rms force in armchair CNT (all radii)

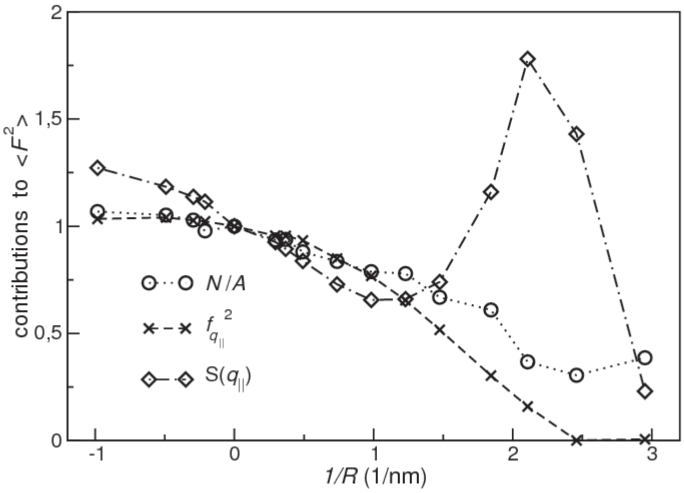

Figure 30: Contact density $\frac{N_1}{A}$, force amplitude $f_{q_{\|}}$ and commensurability factor $S(q_{\|})$ as in Fig. 27, but now for all considered radii. For CNT radii $R > 1$ nm the curvature dependence of all three contributions is monotonous. But in high confinement ($R < 1$ nm) the structure factor changes in an unsystematic way due to the confinement induced ordering of the water molecules along the tube axis. The frictionless flow observed for single file water is caused by the vanishing roughness $f_{q_{\|}}$ of the oxygen-wall potential.

9 Testing predictions

In order to test our theoretical understanding of the physical mechanisms at play, we considered some additional water/carbon systems with other geometries than in section 4. More precisely, we tested our main conclusion that the crucial point to explain the curvature dependence of the friction coefficient (in low confinement) is the degree of commensurability between the water and the carbon structure. To this aim, we perform again simulations in the slab geometry (Fig. 7) but change the carbon-carbon distance of the hexagonal graphene structure.

Furthermore, simulations of water in zigzag CNT predict the dependence of the friction on the CNT chirality in accordance with the presented theoretical model and allow to gain further - and somewhat surprising - insight concerning the mechanisms controlling the water-graphite friction.

9.1 Changing wall structure without curvature - variations of the graphene lattice parameter

Simulations offer an easy possibility to verify the importance of the solid structure for the interfacial friction: We can tune the lattice spacing of the solid wall, and therefore the length of the reciprocal lattice vector $q_{||}$, which determines the structural contribution $S(q_{||})$ to the friction coefficient. We performed equilibrium simulations of the graphene slab system exactly as before, but with a fixed carbon-carbon distance that was either larger ($d = 0.173\,\mathrm{nm}$) or smaller ($d = 0.118\,\mathrm{nm}$) than the real value ($d = 0.142\,\mathrm{nm}$). The values for the carbon-carbon distances of the 'artificial' graphene were chosen to result in $q_{||}$-values that mark the position of the first maximum ($q_{||}^{\mathrm{max}} = 24.2\ \mathrm{nm}^{-1}$) and the following minimum ($q_{||}^{\mathrm{min}} = 35.5\ \mathrm{nm}^{-1}$) of the interface water structure factor (see Fig. 22) in order to get the maximal possible effect on the friction coefficient.

As expected according to Eq. (35), the friction changes indeed with the lattice spacing: We find a smaller value for the friction coefficient $\lambda = 1.8 \times 10^{-5}\,\frac{\mathrm{Ns}}{\mathrm{m}^3}$ for the smaller carbon-carbon distance - equivalent to $q_{||}^{\mathrm{min}}$ - and a larger value $\lambda = 4.9 \times 10^{-4}\,\frac{\mathrm{Ns}}{\mathrm{m}^3}$ for the larger d ($q_{||}^{\mathrm{max}}$). Considering the maximal and minimal value of the structure factor, we note however that the difference is even more dramatic than can be explained only with the structure contribution $S(q_{||})$: while we expect $S(q_{||})$ to differ by a factor of approximately 2, the friction coefficient varies more than a factor of 20.

A careful look at all contributions shows that this bigger variation is again coherent with our approximation for the rms force. Indeed, the comparison in Tab. 4 shows that $S(q_{||})$ is not the only contribution influenced by the lattice spacing of the graphene structure, but the contact density $\frac{N_1}{\mathcal{A}}$ and roughness $f_{q_{||}}$ also change considerably, leading to variations of the static rms force which explain in large parts the behavior of λ. We understand this as follows: Similar to bending the wall, changing the carbon-carbon distance modulates the potential landscape felt by the oxygen atoms. First, the potential well (in perpendicular direction; see also Fig. 18 for CNT) next to the wall deepens with the number of carbon atoms per unit area. Decreasing

Results ’artificial’ graphene

d $(10^{-10}\mathrm{m})$	$q_\parallel$ (nm^{-1})	$S(q_\parallel)$	$f_{q_\parallel}$ $(10^{-12}\mathrm{N})$	$N/\mathcal{A}$ (nm^{-2})	$\left\langle F^2\right\rangle_{\text{theory}}/\mathcal{A}$ $(10^{-4}\frac{\mathrm{N}^2}{\mathrm{m}^2})$	$\left\langle F^2\right\rangle/\mathcal{A}$ $(10^{-4}\frac{\mathrm{N}^2}{\mathrm{m}^2})$	τ_F (fs)	λ $(10^4\frac{\mathrm{Ns}}{\mathrm{m}^3})$
1.18	35.5	0.6	1.6	9.06	0.14	1.01	74	0.18
1.42	29.5	1.0	3.1	8.25	0.79	4.74	109	1.25
1.73	24.2	1.7	4.4	7.17	2.36	14.3	142	4.90

Table 4: Results for equilibrium simulations of water in ’artificial’ graphene slabs (=carbon honeycombs with different C-C distances). The real graphene value is $d = 1.42$ Å; the other values are chosen to maximize ($d = 1.73$ Å) and minimize ($d = 1.18$ Å) the structure contribution $S(q_\parallel)$. the friction coefficient λ The static rms force $\left\langle F^2\right\rangle/\mathcal{A}$ and consequently also the friction coefficient, change with the lattice spacing: as expected they are bigger for $d = 1.73$ Åand smaller for $d = 1.18$ Å. The theoretical estimation of the rms force composed of the various contributions ($\frac{N}{\mathcal{A}}$, $S(q_\parallel)$ and $f_{q_\parallel}$) explains this behavior. A change in the decorrelation time τ_F further adds to the effect on λ.

Density profiles for water next to ’artificial’ graphene

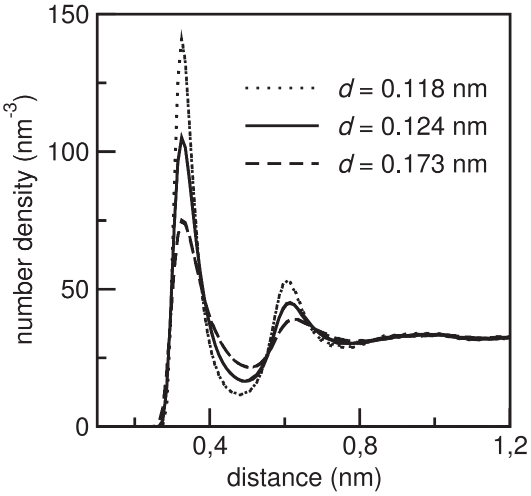

Figure 31: Water density profile in proximity of different ’artificial’ graphene walls for constant temperature $T = 300$ K and pressure $p = 1$ atm. The carbon wall atoms are organized in a honeycomb lattice in all three setups, but with different C-C distances d. The model value for real graphene is $d = 1.42$ Å. The layering effect of water at the graphene wall is stronger for higher carbon surface densities (shorter C-C distance).

the carbon-carbon distance leads to an increase of the solid surface density, and in turn to an increase of the water contact density because attraction is higher with a denser surface (see density profiles Fig. 31). Vice versa, the contact density decreases for a larger C-C distance. Secondly, the roughness of the force field $f_{q_{||}}$ at the bottom of the well depends also strongly on the C-C distance.

Finally, we note that the relation between the friction coefficient and rms force follows less accurately the proportional relation found for the water/CNT systems. In other words, unlike for the systems studied before, the decorrelation time τ_{F} changes notably. This indicates that the decorrelation time is related to the density in the first water layer.

9.2 Changing the carbon nanotube structure - zigzag chirality

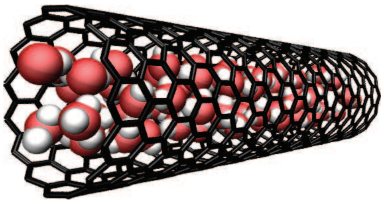
Figure 32: Water in zigzag CNT

Both the roughness and the periodicity of the oxygen potential next to a carbon wall, are determined by the carbon structure. This dependence of the friction coefficient on the wall structure was demonstrated in the previous paragraph by varying the carbon-carbon distance of the graphene honeycomb. Wall curvature has a similar effect on the potential and leads to the observed variations of the friction coefficient for water inside and outside armchair CNT of different radii.

Moreover, bending a graphene sheet to a cylindric shape influences only one component of the lattice vectors for the potential landscape for water in proximity to the wall (compare Eq. (32) to Eq. (43) further down: see also Fig. 28). Therefore, the direction of the cylinder axis with respect to the graphene structure also plays a role for the potential. For other CNT *chirality* the form of the potential evolves differently with increasing curvature [61]. Given its sensibility to both the roughness of the force field and the degree of commensurability between water and wall structur, the friction coefficient should not only depend on the CNT radius, but also on the chirality. To test this prediction, we performed equilibrium and flow simulations of water in *zigzag* CNT with radii between 0.35 nm and 9.8 nm. There is indeed a measurable influence of the CNT chirality on the friction: In zigzag CNT of $R \lesssim 2\,\mathrm{nm}$, we find a considerable higher friction than in armchair CNT of the same size. In particular, although friction decreases again with increasing curvature, it does not disappear completely for single file motion in zigzag CNT, in contrary to armchair CNT (compare Fig. 33).

The different behavior of the friction coefficient for water in armchair or zigzag CNT can be explained within the presented theory. In the low confinement regime (tube diameter above one nanometer), the friction coefficient for zigzag CNT is again proportional to the rms force (Fig. 34). For higher confinement where the water structure changes, the dynamics also change notably. This has an additional impact on the friction coefficient $\lambda = \beta \tau_F \langle F^2 \rangle / \mathcal{A}$ via the decorrelation time τ_F of the force autocorrelation function, which leads to the deviations from the line through

Friction coefficient for water in armchair and zigzag CNT

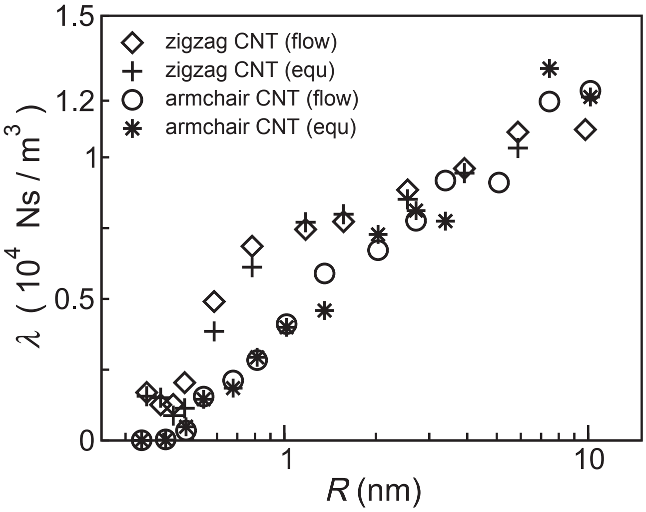

Figure 33: Friction coefficient versus carbon nanotube radius for water inside CNT of different chiralities, namely armchair and zigzag. The different wall structure causes a measurable variation of the friction coefficient for radii smaller than $2-3$nm. We did not find a significant change of friction for different flow directions on graphene.

Friction coefficient vs. rms force for water in zigzag CNT

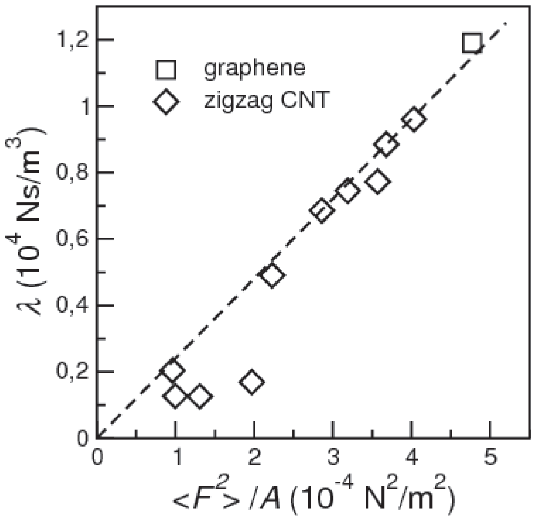

Figure 34: The friction coefficient λ is proportional to the rms force $\langle F^2\rangle/\mathcal{A}$ in the low confinement regime ($R > 1\,\mathrm{nm}$). For smaller radii, confinement effects influence the water dynamics and via the decorrelation time of the force autocorrelation function also the friction coefficient $\lambda = \beta\tau_F\langle F^2/\rangle/\mathcal{A}$

origin in Fig. 34 for small radii. In the following, we focus on the low confinement regime, where only static effects control the friction. In this case, the rms force can be expressed similarly as in Eq.34. The only difference to the derivation for armchair CNT is the Fourier expansion of the force field. In fact, more parts of the Fourier series have to be included to get a decent approximation (see Fig. 37). (The magnitude of the error due to the truncation of the Fourier expansion, as well as of the other approximations that have been introduced, will be discussed in section 10.) We write the force f_z on one oxygen atom in the first water layer for the zigzag chirality as

$$f_z(\mathbf{x} = (s, z)) \approx f_{q_{||}}(\sin(\mathbf{q}_+ \cdot \mathbf{x}) - \sin(\mathbf{q}_- \cdot \mathbf{x})) + f_{q_z} \sin((\mathbf{q}_+ + \mathbf{q}_-) \cdot \mathbf{x}) \tag{42}$$

Furthermore, the definition of $\mathbf{q}_\pm$ themselves are also different in a subtle way. This is due to the fact that switching from armchair to zigzag chirality means that the axial (z) and angular ($s = r\theta$) directions are inverted. Consequently, keeping the notation that the first vector component denotes the radius dependent s-coordinate, we have to write

$$\begin{aligned} \mathbf{q}_+ &= q_0 \begin{pmatrix} \frac{R}{r_\mathrm{o}} \\ \frac{1}{\sqrt{3}} \end{pmatrix} \\ \mathbf{q}_- &= q_0 \begin{pmatrix} -\frac{R}{r_\mathrm{o}} \\ \frac{1}{\sqrt{3}} \end{pmatrix} \end{aligned} \tag{43}$$

Calculating the modulus of the Fourier coefficients for force fields on graphene and in CNT, we find that the main contribution stems from the linear combination $(\mathbf{q}_+ + \mathbf{q}_-$ instead of the individual vectors. For graphene, $f^2_{q_z}$ is about twice the magnitude of $f^2_{q_{||}}$ and for CNT the proportions shift more and more in favor of $f^2_{q_z}$ with decreasing tube radius. So, in contrary to the armchair case, the main q-vector for the periodicity of the potential landscape in zigzag tubes

$$\mathbf{q}_+ + \mathbf{q}_- = q_0 \begin{pmatrix} 0 \\ \frac{2}{\sqrt{3}} \end{pmatrix} \tag{44}$$

is *radius independent*. The length of this vector is $q_z = 29.5\mathrm{nm}^{-1}$.

With the above representation of the force $f(s, z)$, the rms force can, in complete analogy to the derivation for armchair CNT, be estimated to

$$\langle F^2 \rangle \approx N_1 \left(f^2_{q_{||}} S(q_{||}) + \frac{1}{2} f^2_{q_z} S(q_z) \right) \tag{45}$$

where N_1 is the number of water molecules in the first layer and $S(q)$ is the static structure factor of this layer. The length of the wave vectors $|\mathbf{q}_\pm| = q_{||}$ is again radius dependent, but q_z and consequently $S(q_z)$, is not affected by curvature.

Data for the friction coefficient superimpose reasonably well for armchair and zigzag CNT when displayed as λ versus $\frac{N_1}{\mathcal{A}} f^2_{q_{||}} S(q_{||})$ and $\frac{N_1}{\mathcal{A}} \left(f^2_{q_{||}} S(q_{||}) + \frac{1}{2} f^2_{q_z} S(q_z) \right)$,

Friction coefficient vs. theoretical rms force: (artificial) graphene, zigzag and armchair CNT

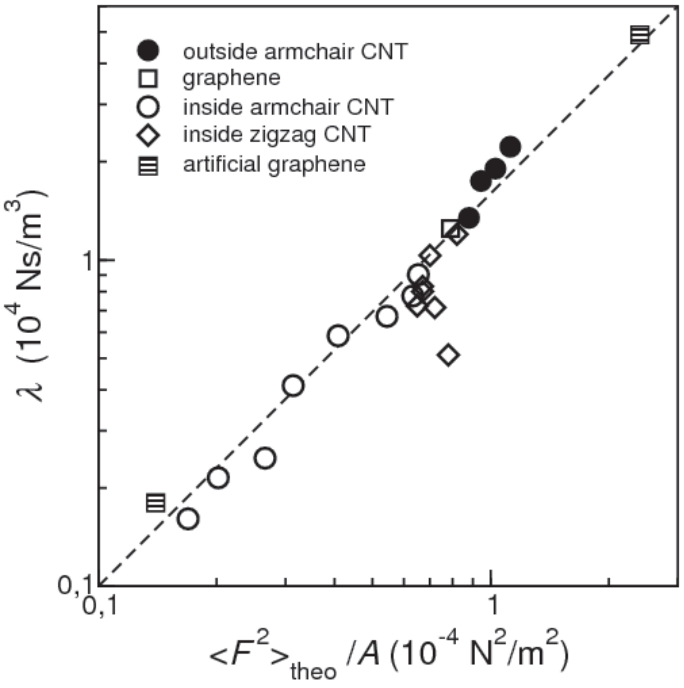

Figure 35: Friction coefficient vs. theoretical rms force for all geometries considered so far: water inside and outside armchair CNT, as well as inside zigzag CNT and water in a graphene slab modeled with different scales for the carbon honeycomb lattice. Results for the friction coefficient in all these setups superimpose well when plotted against the theoretical expressions Eq. (34) and Eq. (45) for armchair and zigzag, respectively. The figure recapitulates two major results of this study: it shows all at once that (i) the curvature dependence of the friction coefficient is a static effect $\lambda \propto \langle F^2 \rangle / \mathcal{A}$ (ii) the static rms force of water on graphitic surfaces can be quantitatively understood within the presented theory. Bending the wall or changing the carbon structure affects the roughness of the wall as it is seen by the interfacial water layer. It also affects the commensurability between this interface layer and the carbon wall. Knowledge of the structure factor of the first water layer allows to tune the friction by choosing the wall structure accordingly as we have done when setting the C-C-distance for 'artificial' graphene.
Only data points for low confinement are included in this plot since the relation $\lambda \propto \langle F^2 \rangle / \mathcal{A}$ and Eq. (34) and (45) hold not true in high confinement where water structure and dynamics change drastically.

respectively. This is shown in Fig. 35. The good agreement for armchair and zigzag CNT further emphasizes that the theoretical expressions for the friction coefficient captures the relevant effects.

To understand better how different CNT chiralities generate different friction forces, it is very informative to compare the three contributions to the rms force for the two CNT chiralities (Fig. 36, compare also Fig. 30).

Contact density The water contact density shows a very similar behavior in zigzag and in armchair CNT. This is not surprising since the carbon surface density remains the same. The contact density which is the number of particles per interface area decreases, because the interface area increases in comparison to the area defined by the radial position of the liquid interface area. This can be explained as follows: While the mass density ρ changes only slightly with the tube radius in low confinement, the surface density at the interface decreases due to a changing ratio between the effective interface area $\mathcal{A}$ and the area defined by the position of the first liquid layer A_1. The latter is $A_1 = 2\pi r_1 L_\mathrm{z}$, a cylinder surface with radius r_1, where $r_1 \approx R - \sigma$ is the position of the first liquid layer. The effective interface area is accordingly $2\pi r_\mathrm{eff} L_\mathrm{z}$, with the effective radius $r_\mathrm{eff} = (R + r_1)/2 \approx R - \sigma/2$. Estimating the number of atoms in the first layer with $N_1 = \rho(r_1)A_1\sigma$, we can write

$$\frac{N_1}{\mathcal{A}} \approx \rho(r_1)\sigma\frac{A_1}{\mathcal{A}} \approx \rho(r_1)\sigma\frac{R-\sigma}{R-\sigma/2} \tag{46}$$

So for constant (or even for slightly increasing) $\rho(r_1)$, the surface density $N_1/\mathcal{A}$ decreases with the tube radius R. This is a purely geometric effect, that contributes nevertheless to the curvature dependence of the rms force.

Potential roughness and commensurability The structure factor and especially the potential roughness, however, exhibit a very different behavior for both chiralities. In armchair CNT, the changing structure contribution is the main effect in low confinement. The potential roughness also decreases continuously and, in particular, it is responsible for the frictionless motion of single file water in $(5, 5)$ and $(6, 6)$ CNT. In zigzag CNT, the behavior of $S(q_\parallel)$ and $f_{q_\parallel}$ is similar to the one in armchair CNT, but the most important contribution to the friction coefficient stems not from $q_\parallel$ but from q_z: For the zigzag flow direction on graphene, f_{q_z} is about the double of $f_{q_\parallel}$ and is increasing further for decreasing zigzag CNT radius, leading to an increasing roughness of the potential energy landscape at the position of the first water layer. Furthermore, $S(q_z)$ is curvature independent in weak confinement, because neither the water structure factor nor the q_z-vector change with the radius. That means no incommensurability like in armchair CNT occurs. The friction decrease for radii larger than $\sim 1\,\mathrm{nm}$ is only due to the decreasing contact density. This explains why the effect is smaller in zigzag than in armchair CNT in weak confinement. Finally, note that for water on graphene the approximate expressions for the rms force in the two different flow directions predict indeed the same value, although

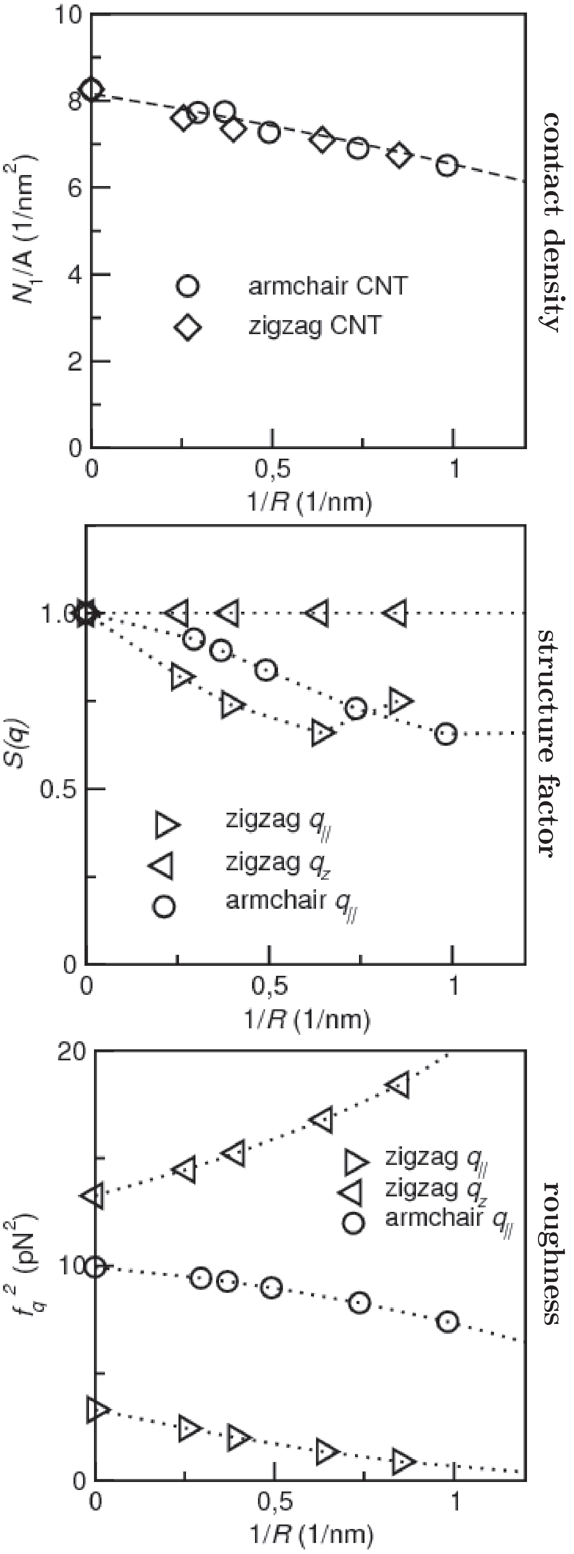

Figure 36: Curvature dependence of the three contributions to the static rms force $\langle F^2 \rangle$ – contact density (*upper*), commensurability factor (*middle*) and roughness of the potential landscape (*lower*) – for water in zigzag and armchair carbon nanotubes in the low confinement regime. While the behavior of the contact density is expected to be identical for all CNT chiralities, both the roughness and the periodicity of the potential are sensible to the wall structure. For tube radii below 2 nm this leads to a measurable different friction in armchair and zigzag CNT.

Upper: The contact density decreases with the curvature according to $\rho_0(R-\sigma)/(R-\sigma/2)$ given by the dotted line (see Eq. (46)) independently of the CNT chirality.

Middle: The wave vector $q_\|$ and consequently the structure contribution $S(q_\|)$ depend on the radius for both armchair and zigzag tubes (see Eq. (32) and Eq. (43)). The structure contributions decrease with increasing curvature indicating a growing incommensurability between water and carbon structure. However, in zigzag CNT, the second wave vector $q_z = 29.5\,\mathrm{nm}^{-1}$ which actually contributes most to the friction force is radius independent. Since the water structure in low confinement is also unchanged, $S(q_z) \approx 1$ is constant.

Lower: Contrary to armchair CNT the water-wall potential gets rougher in zigzag CNT with increasing curvature. Even when $f_{q_\|}$ decreases also for zigzag chirality, the contribution from the Fourier coefficient f_{q_z} is much larger.

While all three contributions to the rms force decrease with the radius in armchair CNT, this is only the case for the contact density in zigzag CNT. No incommensurability occurs for the main wave vector q_z and the associated Fourier coefficient even increases for smaller radii. Altogether, the friction coefficient in zigzag CNT also decreases with increasing curvature, but slower than for armchair tubes.

they compose of different contributions (compare values at $1/R = 0$ in Fig. 36).

In short, for both CNT types increasing curvature leads to decreasing friction, but according to our understanding, caused by subtly different effects. Since armchair and zigzag represent the two extremes of all possible chiralities, it seems likely that the discussed mechanisms (decreasing contact density, smoothing of potential and incommensurability) also lead to a decrease of friction for the intermediate chiralities.

9.3 Non-linear behavior for large slip velocities

Having found the mechanisms leading to the curvature induced friction decrease in CNT, we can now try to also understand the decrease in friction that has been encountered in flow simulations with high velocities. The relation between slip velocity v_{slip} and friction force F becomes non-linear for v_{slip} higher than $\sim 50\frac{\text{m}}{\text{s}}$ – the derivative $\frac{\text{d}F}{\text{d}(v_slip)}$ decreases with higher flow velocity. This was observed in several graphene slab simulations, both with TIP3P and SPC-E water model with the LAMMPS software package. Ma *et al.* also report about this effect in recently published work [64]. They performed MD simulations of water flow through CNT up to velocities about $\sim 1000\frac{\text{m}}{\text{s}}$. In a graphene slab simulation (slab size $H = 2.08\,\text{nm}$), we checked if this friction decrease has again a static origin. Contact density or water structure might be influenced by the high accelerations. But for flow velocities $\sim 10^3\,\frac{\text{m}}{\text{s}}$, we did not observe changes in the water density distribution or the water structure factor. Thus, the decreasing friction must have a dynamic cause. Changes in the dynamics have been found by others, for example, longer hydrogen bond lifetime for higher flow velocities [34].

10 Quantitative agreement between the rms force and its approximation

Before, we showed that the curvature dependence of $\langle F^2 \rangle$ was correctly reproduced by its approximate simple form $N_1 f_{q_{||}}^2 S(q_{||})$. However, the two quantities differ by a numerical prefactor, as seen in Fig. 26. Given that several approximations have been applied in the derivation of this formula, a certain discrepancy is not surprising. In the following, the quality of these approximations will be discussed one by one. We anticipate that this numerical discrepancy in the prefactor stems from the distance to the wall at which the force landscape for water molecules is evaluated. This globally scales up the force amplitude without affecting the structure of the landscape and thus the underlying physics.

10.1 Neglect of second water layer

The first approximation was to neglect all water molecules except those in the interface layer. In principle, in the performed MD simulations, it would have been possible to directly calculate the part of the friction force that stems from interaction with the first water layer and compare the proportion to the total force. Unfortunately, the necessary information to do so was not recorded. Instead of re-running time consuming simulations, the importance of the omitted contribution can also be estimated out of existing data using the presented theory for the rms force: we can evaluate the *second* water layer similarly to the first one, that means calculating $\frac{N_2}{A} f_{\mathbf{q}}^2 S(\mathbf{q})$ for the second water layer. In the course of this analysis, it was found that the form of the potential energy landscape at the radial position of the second layer is completely different than for the first layer (see Appendix B). Consequently, we can not assume the principal wave vector $\mathbf{q}$ to be the same as for the first layer. More information about the form of the oxygen wall potential and in particular about the dependence of its amplitude on the distance to the wall, will be given later on. At this point, we take the force field amplitude $(f_z^{\max} - f_z^{\min})/2$ as an upper limit for the roughness $f_{\mathbf{q}}$. Using the example of water on graphene, we find that the force field amplitude for a water molecule in the second layer is three orders of magnitude smaller than for the first layer (see also Fig. 38). Since the friction coefficient depends quadratically on $f_{\mathbf{q}}$, we conclude that the contribution of the second water layer is indeed insignificant.

10.2 Truncation of the force field Fourier expansion

The second approximation is the truncation of the Fourier expansion of the oxygen/wall force field at the position of the first water layer after the leading term. To estimate the magnitude of the neglected part, we calculate numerically the Fourier coefficients of the following term. For graphene, the force field Fourier transforms for both flow directions, 'armchair' and 'zigzag', are shown in Fig. 37. For the friction force in x-direction (armchair) we write $f_x \approx f_{q_{||}}(\sin(\mathbf{q}_+ \cdot \mathbf{x}) - \sin(\mathbf{q}_- \cdot \mathbf{x})$. The next biggest contributions stem from the wave vector $\mathbf{q}_+ - \mathbf{q}_-$. But the magnitude of the

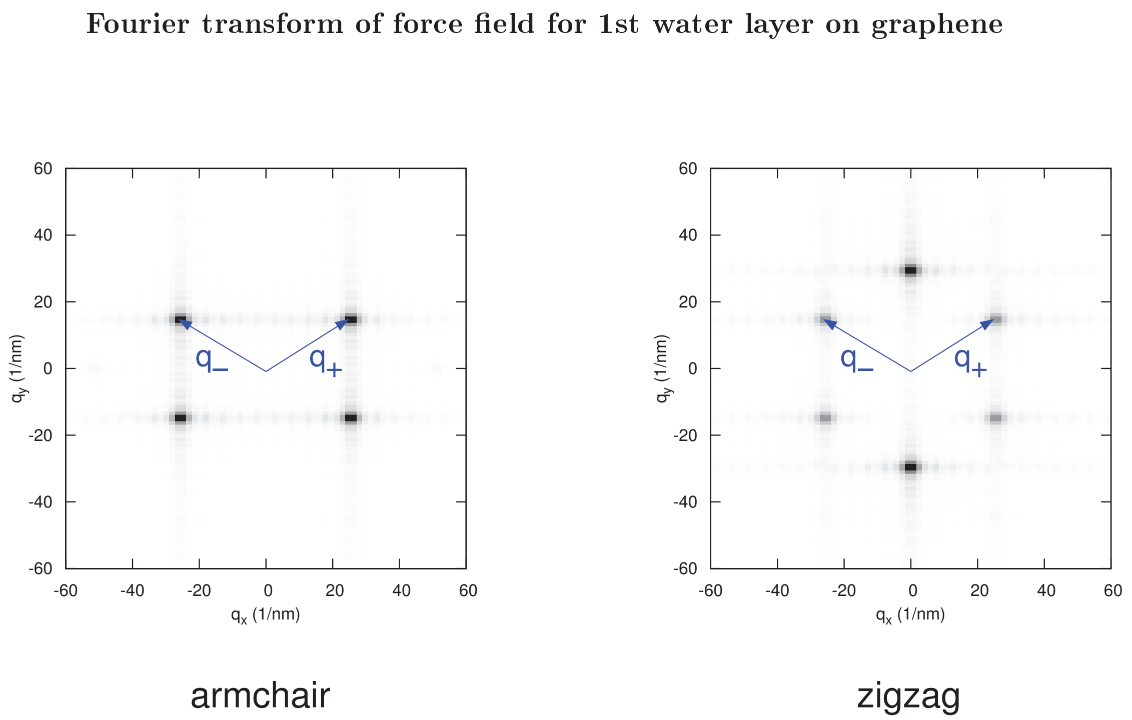

Figure 37: Fourier transform (FT) of the force field on an oxygen atom at distance σ from a graphene sheet.

Left: FT of force field in x-direction ('armchair' direction) $F_x(\mathbf{x}) = f_{q_\parallel}(\sin(\mathbf{q}_+ \cdot \mathbf{x}) - \sin(\mathbf{q}_- \cdot \mathbf{x}))$+higher order terms;

Right: FT of force field in y-direction ('zigzag' direction) $F_y(\mathbf{x}) = f_{q_\parallel}(\sin(\mathbf{q}_+ \cdot \mathbf{x}) - \sin(\mathbf{q}_- \cdot \mathbf{x})) + f_{\mathbf{q}_+ + \mathbf{q}_-} \sin((\mathbf{q}_+ + \mathbf{q}_-) \cdot \mathbf{x})$+higher order terms;

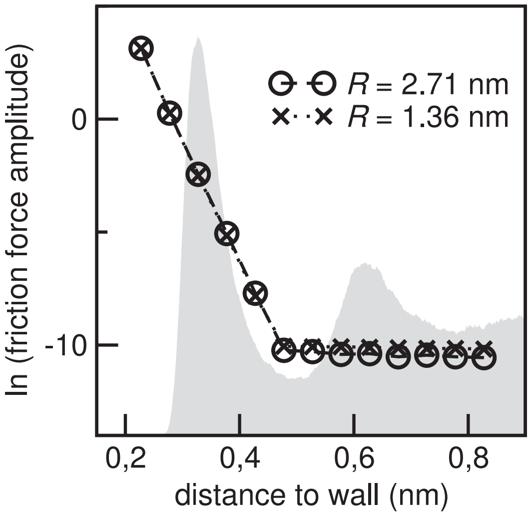

Amplitude of the lateral force field for different wall distance

Figure 38: Amplitude of the lateral force field for one oxygen atom close to a CNT in dependence of the oxygen-wall distance d. Note that the plot actually shows the logarithm $\ln f_{\mathrm{max}}$. The gray area is a sketch of the oxygen density profile and thus gives the position of first and second water layer. The roughness (amplitude) of the force field increases exponentially approaching the wall $f_{\mathrm{max}}(d) \propto \exp(-\alpha d)$ where the exponential coefficient α changes abruptly at a distance $\sim 1.5\sigma$. In the region of the first layer, the exponent is radius independent.

Fourier coefficients $f_{\mathbf{q}_+\mathbf{q}_-}$ is less than 3% of $f_{\mathbf{q}_\pm}$. For the friction force in y-direction (zigzag), the contribution from the wave vector $\mathbf{q}_+ + \mathbf{q}_-$ is the most important one, followed by the contributions from $f_{\mathbf{q}_\pm}$. Hence, we have to write for the force field $f_y \approx f_{q_{||}}(\sin(\mathbf{q}_+ \cdot \mathbf{x}) - \sin(\mathbf{q}_- \cdot \mathbf{x})) + f_{q_z} \sin((\mathbf{q}_+ + \mathbf{q}_-) \cdot \mathbf{x})$. Higher order terms that are not considered in this formula are several orders of magnitude smaller. In other words, the approximations for the force fields are very good.

10.3 Projection of the first water layer

Finally, the first water layer was assumed to be a two dimensional plane: every oxygen atom was supposed to be located at a fixed distance σ from the wall. In reality, the water layer has a certain thickness $\sim \sigma/2$. The influence of this simplification is difficult to quantify directly. But since the discussed approximations are the only ones entering into the derivation of Eq. (35), we can attribute the quantitative discrepancy that can be accounted for neither by the truncation of the Fourier expansion nor by the neglect of the second layer, to this reduction of dimensionality (from 3D layer to 2D plane). Since the first two simplifications have been found not to result in any significant errors, the projection of the atom positions has to be responsible for the observed quantitative discrepancies between the rms force $\langle F^2 \rangle$ and the approximation. In fact, we can check the reality of this conclusion by measuring the friction force on one single graphene plane, that is wetted by a single water layer with molecular thickness: We restrict the oxygen positions of this water layer artificially to the distance σ from the wall. In this setup, the only inexactness in Eq. (34) and (45) for the mean squared friction force in armchair and in zigzag direction, respectively, stems from the force field approximation, which was found to be very accurate. Indeed, the measured values for $\langle F^2 \rangle$ differ less than 3% from the 'theory' for both flow directions.

The reason why a projection of the water positions on the cylinder surface at $R-\sigma$

leads to an underestimation of the friction force becomes clear from a deeper look at the oxygen wall potential. Calculating the potential landscape $V(s, z)$ at varying distances from the wall, we find that the force amplitude increases exponentially when a molecule approaches the wall. Particles at a distance smaller than σ feel a considerable rougher potential as we estimate in Eq. (35) and thus their contribution to the friction force is underestimated. The form of the potential stays about the same over the whole radial range occupied by the molecules in the first layer; see Appendix B for plots of the force field landscape at different r.

Part IV

Investigation of other liquid/solid combinations

The last part of this manuscript is concerned with the question how the hitherto discussed study of the water/carbon friction can be extended to other fluid/solid interfaces. In other words, we will investigate in how far the presented theoretical understanding of interface mechanisms controlling friction based on the consideration of the rms force, is transferable to other liquid/solid combinations. In this context, we look at two interface types: First, water in hydrophilic nanometric silica pores are studied as a counter example where friction at the solid wall is very large, compared to graphitic walls. In this system we expect the no-slip boundary condition to hold true, which would be equivalent to a diverging friction coefficient $\lambda = \eta/b$. We will see to which extend the equilibrium measurement of the friction coefficient reflects this theoretical expectation. Additionally, a simple poiseuille flow simulation shows that the relevant property impacting water flow in nanometric silica pores, is not the interface friction, but the water viscosity.

In the second section of this part, we come back to the graphitic systems that have been investigated in detail above, but instead of limiting the studies to water filled pores, various other liquids are considered in this last section. The aim is to broaden the range of applicability of our understanding of the molecular origin of liquid/CNT friction to other liquids. Specifically, we consider decane and ethanol, because experimental results are available for these two liquids.

We also performed simulations with OMCTS, that is often used in the experimental field as a model for a Lennard-Jones liquid. Finally, a comparative summary completes the chapter.

Contents

11 Introduction and motivation **91**

12 Water flow in a silica pore **93**

12.1 System setup 93
12.2 Equilibrium measurement of the friction 94
12.3 Poiseuille flow simulation to determine the slip length 95

13 Fast fluid flow in CNT - other liquids **97**

13.1 Model parameters: molecule geometries and interaction potentials 97
13.2 Considered systems and their equilibrium density profiles 99
13.3 Liquid/graphite friction for larger molecules 102
  13.3.1 Curvature dependent friction 102
  13.3.2 Application of the theory for the rms force to organic liquids 104
  13.3.3 Microscopic effects that influence liquid/graphite friction . 106
13.4 Summary and outlook 109

11 Introduction and motivation

The main part of the presented study concerns water flow in graphitic systems, and especially in carbon nano tubes. This focus was motivated by the high hopes CNT have generated with respect to possible applications and by the central role of aqueous solutions in the aforementioned applications as well as in many biological and chemical processes on the micro- or nanoscale. The question arises if the observed high permeability - due to low friction and even superlubricity - is a *unique* property of water/CNT systems. Could membrane of other materials feature the same high water flow rates? And would other fluids in CNT exhibit comparable as water? To find answers to some aspects of these questions, we also performed simulations of other liquid/solid combinations.
Considering our understanding of the liquid solid friction based on the hitherto existing results, we can already partly give an answer. We remind the effects leading to the low water-carbon friction that have been discussed in the previous part: i) extreme smoothness of the graphitic wall, and ii) incommensurability between water and carbon structure. Ultimately, both effects rely on the regularity of the atomically smooth carbon honeycomb structure, an intrinsic property of graphene. To underscore the huge difference between fast transport in CNT and water flow through a material with vanishing slip, we conducted a study of water flow in a nanometric pore made of silica glass. The outcome of these simulations will be discussed in section 12.

We now come back to the second question - are CNT fast transporters only for water or also for other fluids? Firstly, we note that the degree of (in)commensurability is of course sensible to the solid and fluid structure, and thus a specific (and unknown) property of each fluid/solid interface. But concerning the smooth CNT surface, this cause for low friction holds true for all liquids, provided that their interaction with the carbon wall can be modeled qualitatively in the same way – a short ranged potential combining an attractive and a repulsive part. We thus expect CNT membranes to be fast transporters for a variety of fluids.

Although the scientific community's main interest was on water flow through CNT, most of the groups whose work was presented in the beginning (section 2), also considered other fluids, liquids as well as gases. In particular, ethanol and decane were included in several studies. As for water, first evidence of low decane/CNT friction was found in simulations: Supple and Quirke carried out MD simulations of decane imbibition in single walled CNT [92, 93, 94] and found that the tube was filled much more rapidly than expected (velocities $\sim 800\frac{\mathrm{m}}{\mathrm{s}}$ for tube radius $R = 0.48\,\mathrm{nm}$). Furthermore, the imbibition speed was constant over the considered time intervals; The penetration length was found to be a linear function of time, instead of the $\sqrt{t}$-dependence predicted from the Washburn law [108]. Following these findings, Majumder *et al.* [67] and Whitby *et al.* [110] conducted experiments of flow measurements not only with water, but also with decane and ethanol. They both reported on results comparable to those for water. Like for water, experimental results disagree to a large extend. Majumder *et al.* state slip length in the micrometer range for CNT radius 7 nm. The slip they observe for ethanol is about two times, and for decane about ten times smaller than for water. Whitby *et al.* get slip length 30 to 40 nanometers and results for the three liquids differ less than 20%.

While these simulation and experimental results agree in general with our expectation that the observed behavior of water also holds true for other liquids, the degree of understanding remains unsatisfactory. Particularly, we would like to make a prediction regarding the order of magnitude for the friction coefficient and its curvature dependence. In order to accomplish this, we performed MD simulations as well as a theoretical analysis of liquid/solid friction for decane and ethanol in armchair CNT, based on the work that we did before for water.

Additionally, we also considered octamethylcyclotetrasiloxane (OMCTS). This organic liquid made of globular-shaped molecules of relatively large diameter ($\sim 1\,\mathrm{nm}$), is an inherent part of a long ongoing discussion about liquid dynamics under confinement. It has been shown, that a solidification of liquid can occur, when it is situated between two plates, where the distance approaches about 6 times the molecular diameter. Due to its near spherical shape OMCTS became popular as a model for simple Lennard-Jones fluids, and is extensively used in experiments to study such confinement effects [4, 18, 65]. A theoretical description that accurately reproduces this phase transition to an ordered state is still missing. The liquid/wall friction could play a big role in this question. That is why we checked if our theoretical model also works for other liquids than water.

12 Water flow in a silica pore

In this section, we report on MD results for water flow through amorphous silica nanopores. Due to the hydrophilicity of the pore surface in the silica glass that was used, we expect the no-slip boundary condition to hold true in this system. This expectation is backed by results from Gruener *et al.* who performed experiments on capillary rise of water [31] and hydrocarbons [32] in hydrophilic silica pores with mean radii smaller than 5 nm. They measured the mass uptake of a porous silica sample due to water imbibition and found an excellent compliance of the square root of time Lucas-Washburn law which implies that no slippage occurs.

12.1 System setup

The equilibration of the system consisted of two steps: First, the silica pore was prepared and then it was filled with water and equilibrated at constant temperature, pressure and number of particles.

Preparation of silica pore The preparation of a cube shaped sample of silica glass was actually performed by Boris Mantisi in the group 'Theory and Modeling' at the LPMCN, Lyon. This part of the simulations was done in the framework of his PhD studies about low vibrational properties of silica glasses. A modified BKS-potential [13, 102] was applied to model the SiO_2 probe. The silica glass was obtained by starting from the cristobalite beta SiO_2 crystal configuration which was then heated to 5200 K in 10^{-10} s. Subsequently, the system relaxed for further 10^{-10} s, before it was quenched to 1 K in 10^{-9} s. Then, the potential energy of the obtained configuration was minimized with the conjugate gradient method and finally, the sample size was adapted to obtain zero pressure.

After preparation of an equilibrated sample of silica glass as it was just described, the silicon and oxygen positions were fixed. A cylindrical pore was drilled into the cube by omitting all atoms with positions $x^2 + y^2 < R^2$. We considered pores with radii $R = 0.5$, 1.0 and 2.0 nm. Due to the amorphous structure, the resulting pore surface is relatively rough compared to graphene and features no distinct periodicity.

Water filling A silica force field for the interaction with TIP3P water has been proposed by Cruz-Chu *et al.* [17]. They applied a similar procedure as Werder *et al.* used to obtain the water/graphite interaction parameters: While the values for oxygen and hydrogen composing water are those of the TIP3P model, the Lennard-Jones and Coulomb force fields for silicon and oxygen in silica have been tuned to reproduce the experimental contact angle of water on silica glass for different surface treatments of the silica glass. Parameters for Si and O of silica are

	σ (Å)	ϵ (kcal/mol)	q (e)
Si	3.83	0.30	1.0
O	3.12	0.15	−0.5

Parameters for the water-silica interactions (O_{water}-O_{silica} and O_{water}-Si) are calculated with standard mixing rules $\sigma_{XY} = (\sigma_X + \sigma_Y)/2$ and $\epsilon_{XY} = \sqrt{\epsilon_X \epsilon_Y}$. To fill the

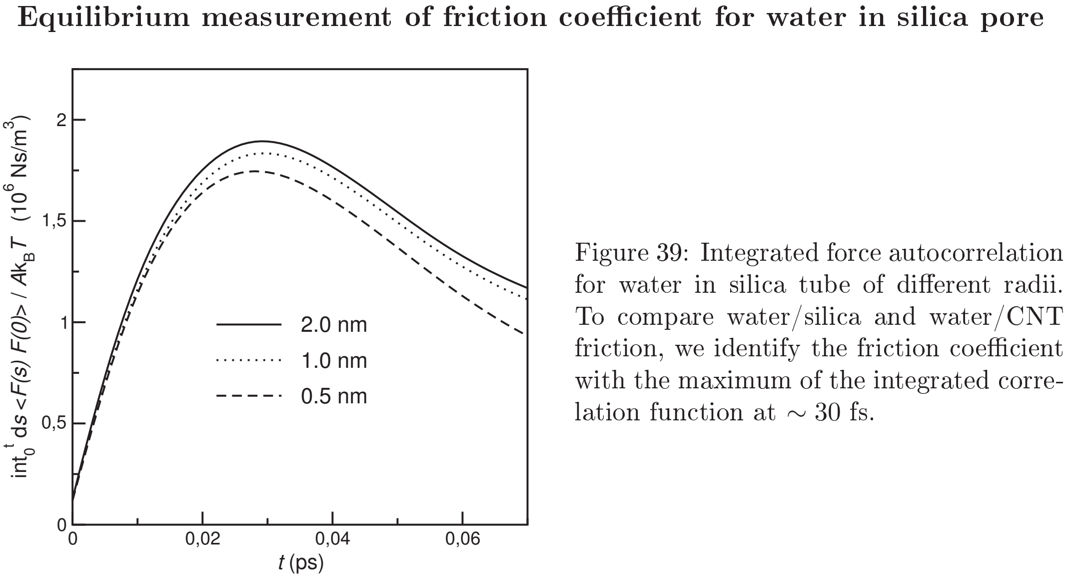

Figure 39: Integrated force autocorrelation for water in silica tube of different radii. To compare water/silica and water/CNT friction, we identify the friction coefficient with the maximum of the integrated correlation function at ~ 30 fs.

silica pores with water, the same procedure as for CNT was used (compare section 4). The wetting properties of silica lead to an easy infiltration of water from the reservoirs at both open ends of the pores (at 1 atm). After attaining equilibrium density, reservoirs were removed and simulations were performed at constant number of particles, volume and temperature, exactly as explained in detail for water in CNT.

12.2 Equilibrium measurement of the friction

Due to its hydrophilicity and (relatively) high roughness, we expect the no-slip boundary condition to hold true for the silica-water interface, which in theory, amounts to a diverging friction coefficient $\lambda = \eta/b$. This means on the one hand, that contrary to water flow in CNT, the flow rate through silica pores is not determined by the interfacial friction, but by the fluid viscosity. In other words, the friction coefficient is not the relevant physical property describing water flow through silica pores. On the other hand, for small slip length, a clear parabolic velocity profile is established in flow simulations. Comparison to the theoretical Poiseuille flow profile allows to measure η and b. We performed such flow simulations and the results will be presented in the next subsection. Nevertheless, to directly compare results for the water/CNT and the water/silica friction coefficient, we also performed equilibrium simulations and measured the force auto-correlation function.

The procedure for the friction measurement is again the same as for water in CNT: During 4 ns the force between silica and water was calculated every 2 fs and then, λ was calculated according to the Green-Kubo relation Eq. (16). Results for the integrated force auto correlation function are shown in Fig. 39. If we identify the friction coefficient with the maximum of the integral, we find a value of approximately $1.8 \times 10^6 \frac{\mathrm{Ns}}{\mathrm{m}^3}$. This is two orders of magnitude higher than friction on graphene. To estimate the corresponding slip length, we take the literature value for the TIP3P water bulk viscosity $\eta_{\mathrm{TIP3P}} = 0.3 \times 10^{-3} \frac{\mathrm{Ns}}{\mathrm{m}^2}$ [30], and find accordingly $b = \eta/\lambda \approx 0.2\,\mathrm{nm}$. Given the uncertainty on the exact position of the hydrodynamic boundary, this result for the slip length $b < \sigma$ is in good accordance with the no-slip boundary condition. We note that the wall roughness also complicates the definition of the contact area $\mathcal{A}$ which enters Eq. (16). In fact, the rather porous composition (with respect to size of a water molecule) leads to slightly overlapping water and silica densities in the interface region. In this situation, a proper definition of the contact area is not obvious. But the uncertainty is only of the order of the wall roughness; the choice to set the contact area $\mathcal{A} = 2\pi RL$ with the tube radius R is a good enough estimation for the given purpose (determining the order of magnitude of water/silica friction). As a final remark before we switch to the flow measurements, we emphasize that no curvature dependence was observed. The measured friction coefficient holds true for all tested tube sizes $R = 0.5$, 1.0 and 2.0 nm.

12.3 Poiseuille flow simulation to determine the slip length

Water flow through a silica pore with radius $R = 2\,\mathrm{nm}$ was driven by a gravitational force: all liquid atoms were subject to a constant acceleration $2.9 \times 10^{-10} \frac{\mathrm{m}}{\mathrm{s}^2}$. After approximately 10^{-11}s a stationary velocity profile was obtained. This is much faster than in CNT, where it takes more like 10^{-9}s to establish stationary flow. From the velocity profile in Fig. 40 it is immediately apparent that, as expected, no slip occurs: water velocity falls to zero at a radius even slightly smaller than 2 nm. We thus consider the Poiseuille profile Eq. (13) for $b = 0$, which simply reads

$$v(r) = \frac{\tilde{R}^2}{4\eta} \left(1 - \frac{r^2}{\tilde{R}^2}\right) \rho g \tag{47}$$

with acceleration g and the position of the hydrodynamic radius $\tilde{R}$ where $v(\tilde{R}) = 0$. Fitting this theoretical curve allows to determine the water viscosity η; $\tilde{R}$ is a sec-

Poiseuille profile water in silica tube

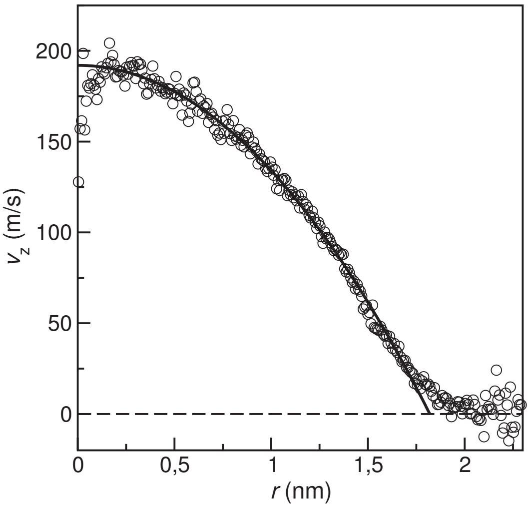

Figure 40: Poiseuille flow profile of water in silica tube. The pore radius, given by the most inner silica atoms, is 2 nm. The no-slip boundary condition holds true at the hydrodynamic boundary which was found to be positioned 0.18 nm further inside.

ond independent fit parameter. The middle of the tube is excluded from the fit range because statistics are poor. The region close to the wall is equally excluded, because the velocity profile deviates from the theoretical parabolic shape. The hydrodynamic boundary is found to be 1.8 Åinside the radial position R of the most inner silica atoms, which is a well known phenomenon [3]. We note that the result for $\eta = 1.5 \times 10^{-4} \frac{\mathrm{N}s}{\mathrm{m}^2}$ is about two times smaller than the bulk viscosity. The reason for this could be a too elevated flow velocity.

In this section, we investigated the boundary condition for water in a hydrophilic pore. We confirm in a Poiseuille flow simulation the accurateness of the no-slip boundary condition in the studied water/silica system. Although it is possible to calculate a friction coefficient defined by the Green-Kubo relation in equilibrium simulations in this no-slip simulation, the usefulness of this approach is clearly limited. The friction coefficient is not the crucial parameter for the flow rate in the no-slip case, it is the water viscosity.

13 Fast fluid flow in CNT - Transfer of the theoretical understanding to other liquids

Due to their extreme smoothness, we suspect CNT to exhibit low friction not only for water, but also for other liquids. For this reason, we extended our studies of liquid/graphite systems to decane, ethanol and OMCTS.

13.1 Model parameters: molecule geometries and interaction potentials

Decane belongs to the group of saturated hydrocarbons (alkanes). Hydrocarbons are composed solely of hydrogen and carbon atoms; they are non-polar. A decane molecule is a flexible chain build of ten carbon atoms where the remaining bonds are saturated with hydrogen atoms. Each carbon atom forms a functional group together with the directly bonded hydrogen atoms; that is decane consists of eight CH_2 segments (methylene groups) and two CH_3 segments (methyl groups); the chemical formula is thus $CH_3(CH_2)_8CH_3$. Functional groups are complexes of atoms within molecules that determine the chemical characteristics of these molecules, because a functional group will show similar reactivity no matter the size of the molecule it is part of. Decane can therefore be considered as representative for the whole group of n-alkanes $CH_3(CH_2)_nCH_3$ with the chain length $n+2$ the only significant difference. From a theoretical point of view, it suggests itself to consider functional groups as one pseudo-atom. The resulting model is of course a somewhat less accurate picture of reality than to treat each hydrogen and carbon atom individually. But it also reduces considerably the number of interaction sites, and accordingly, the computational effort for numerical simulations, while still allowing to fairly reproduce the liquids properties [87, 69, 46]. We thus adapt to common practice to use such a united atom model, the popular optimized potentials for liquid simulations (OPLS) [46], for our investigation of liquid/solid friction for decane in carbon nanotubes. The CH_2 and CH_3 complexes are each represented by one neutral point mass. Bond length as well as angles are fixed at 1.53 Åand 112°, respectively. An intramolecular rotational potential (dihedral potential) for groups of four directly linked functional groups limits torsion of the middle bond. Pseudo-atoms of different molecules interact as Lennard-Jones particles with different LJ parameters for methyl and methylene groups.

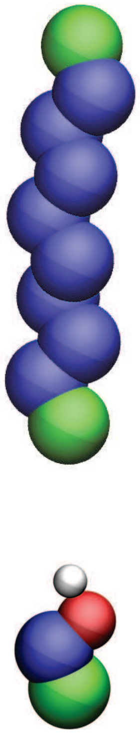

Figure 41: Sketch of decane (*upper*) and ethanol (*lower*) molecule

Ethanol is an alcohol. An ethanol molecule is a chain of one methyl, one methylene and one hydroxyl group (CH_3CH_2OH). Consistently, we used the OPLS potential for liquid alcohols [45]. The CH_3 and CH_2 complexes are again united to one pseudo-atom each. The hydroxyl group, however, is modeled with two distinct interaction sites which is necessary to come up to a realistic charge distribution. Point charges are assigned to the H, O and CH_2 sites, resulting in a dipole moment 2.2 D. Bonds and angles are again fixed and all four masses are linked by a dihedral potential.

Octamethylcyclotetrasiloxane (OMCTS) is a cyclic molecule where four silicon and four oxygen atoms form an inner ring. To every Si atom two methyl groups are bonded. These eight CH_3 groups build the outer 'shell' of the molecule whose dipole moment is small. The overall shape of an OMCTS particle is often described as almost spherical, but somewhat compressed in one dimension. Its molecular radius $\sim 0.9\,\mathrm{nm}$ is three times larger than water. Due to its relatively large size and near-spherical shape, OMCTS is considered as a good large-scale model of a simple Lennard-Jones liquid. It was used to study confinement effects on liquids at system sizes comparable to the molecular diameter, but still experimentally controllable [55, 4, 18]. In the same spirit, first approaches to simulate liquid OMCTS consisted of a super-unified model where the whole molecule is reduced to one large Lennard-Jones particle or even to a hard sphere [70]. However, this simplification loses sight of the intramolecular structure. Keeping in mind that our investigation of water/graphite systems just revealed liquid structure to play a crucial role for the amount of liquid/solid friction, this view does not appear suitable for our purpose.

A more sophisticated force field was proposed only in 2010 by Matsubara *et al.* [70]. It is modeled as a rigid body (fixed bond length and angles) of 16 point masses: the inner ring of 4 silicon and 4 oxygen atoms and the outer shell of 8 methylen groups. To reduce the computational charge, molecules interact with each other only via the outer methylene groups. The optimized Lennard-Jones parameters for the CH_3 pseudo-atoms therefore implicitly include interactions with the inner oxygen and silicon atoms. Not surprisingly, the resulting effective potential is different from the CH_3 potential in the OPLS model.

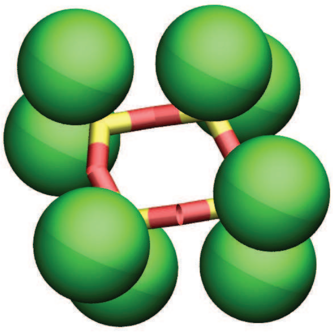

Figure 42: Sketch of OMCTS molecule

Finally, the interaction of the various atom types (O, CH_2 and CH_3) that are present in one or more of the considered liquids, with the carbon wall has to be defined. Since graphene and CNT solely consists of sp^2 hybridized carbon atoms and OPLS also offers a force field for this atom type, this is the logical choice for decane and ethanol. Furthermore, lacking a distinct modeling of the CH_3/C-potential to match the OMCTS/graphite interface properties, we also fall back to

		σ (Å)	ϵ (kcal/mol)	q (e)
decane	CH_3	3.905	0.175	0.0
	CH_2	3.905	0.118	0.0
ethanol	CH_3	3.905	0.175	0.0
	CH_2	3.905	0.118	0.265
	O	3.07	0.170	−0.700
	H	0.0	0.0	0.435
OMCTS	CH_3	3.54	0.39	0.0

Table 5: Interaction parameters for the intermolecular potentials of all (pseudo)atoms figuring in one ore more of the considered liquids.

X	σ_{XC} (Å)	ϵ_{XC} (kcal/mol)
CH_3	3.828	0.136
CH_2	3.828	0.111
O	3.41	0.134
H	0.0	0.0

Table 6: Lennard-Jones parameters for the liquid-wall interaction potentials for all atom types.

the OPLS parameters in case of OMCTS.

Values for the intermolecular interaction potentials for decane, ethanol and OMCTS are given in Tab. 13.1 and for the dihedral potential of ethanol and decane in Appendix C. Parameters for the Lennard Jones interaction with the carbon wall are given in Tab. 13.1.

13.2 Considered systems and their equilibrium density profiles

To study liquid/solid friction for the liquids introduced above, CNT with radii $R = 0.54, 0.68, 1.36$ and 2.71 nm as well as graphene slabs between roughly 1 and 7 nm were considered. The procedure for system equilibration of the filled tubes/slabs was identical to the one used for water. All systems were kept at 300 K and 1 atm. OMCTS did not enter in CNT with radii smaller than ~ 0.6 nm, which is easily understandable given its large molecular diameter. Keeping in mind the importance of the interface morphology for the amount of friction, the characteristics of the liquid boundary region are going to be discussed for the various liquids. In the following, we concentrate first on the layering effect and we describe qualitatively the spatial arrangement of the molecules in the interface layer(s). Later on, a more quantitative analysis follows – the interface structure factor will be presented in connection with an evaluation of the static rms force.

Decane, ethanol and OMCTS exhibit all three a wetting behavior and a pro-

Radial density profiles

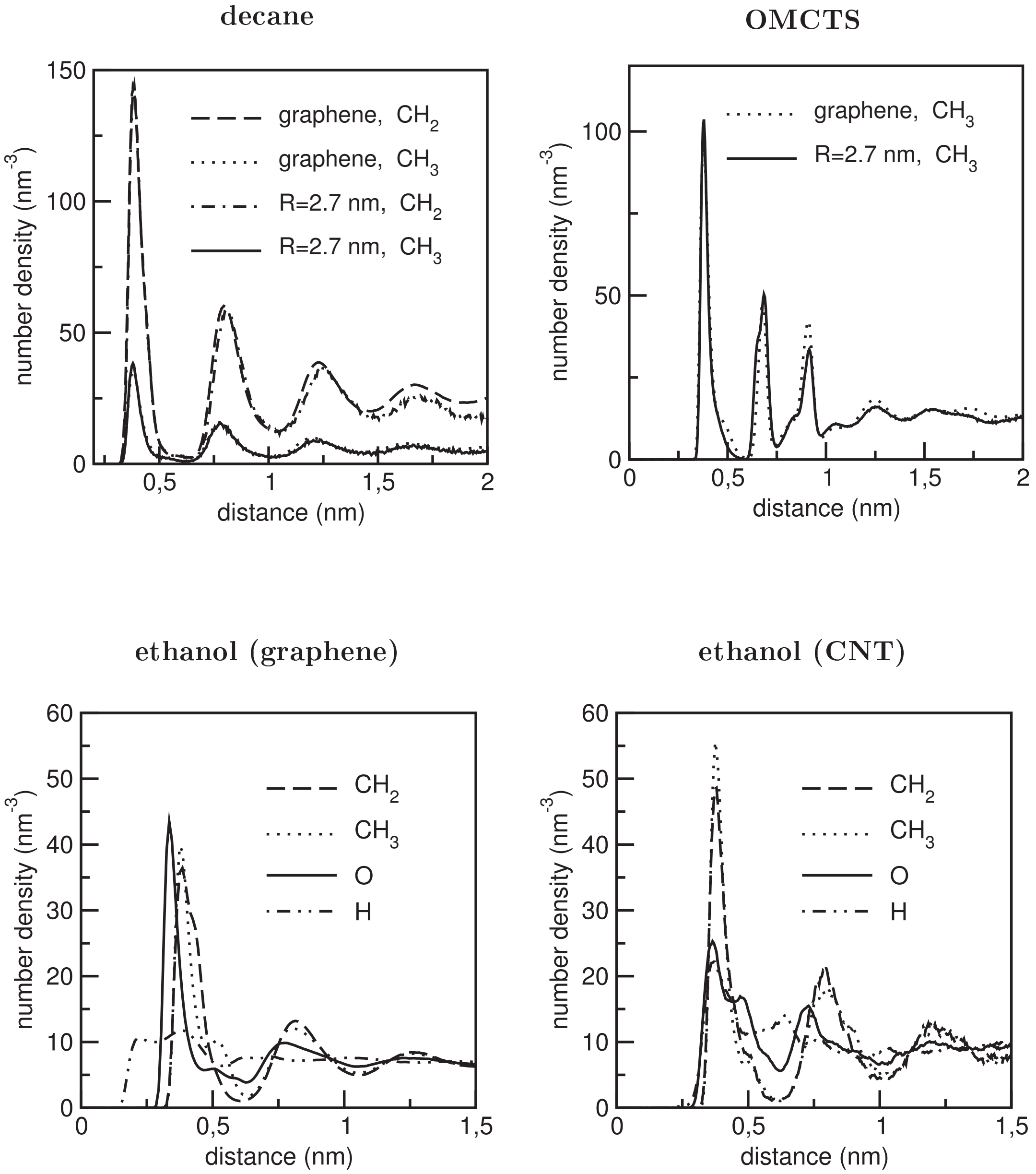

Figure 43: Density profiles for the three considered liquids in the graphene slab geometry and in CNT with radius $R = 2.7\,\mathrm{nm}$: decane (*upper left*), OMCTS (*upper right*) and ethanol (*lower left* graphene, *lower right* CNT)

nounced layering on the graphitic surfaces. Looking at the equilibrium density profiles shown in Fig. 43, we want to attract attention to several points. At first, note that Fig. 43 displays the time averaged radial density distributions separately for all point masses of different type. Silica and oxygen of OMCTS are not shown, since they do not interact anyway, and are therefore not of direct interest for the friction force measurement.

First, the two liquids interacting solely via carbon functional groups with the carbon wall, decane and OMCTS, are considered. In this case, the first density peak is quite prominent. This 'first layer' is very well defined in the sense that the width of the peak is narrow and it is followed by a zone of depletion, where the density is effectively zero, before the 'second layer' follows. The reason for this zero density zone, however, is different for decane and OMCTS. It is a direct consequence of the different molecular morphologies (linear or spheric) and the way the molecules are organized. For decane, the first and second layer do rarely share atoms from a single molecule at the same time. That means a decane molecule which is part of the first layer is usually *completely* situated in the first layer. The same is true – to a somewhat lesser extend – for the second layer. Contrarily, in the case of OMCTS, all three interface layers of the CH_3 density profile in Fig. 43 correspond to only *one* layer of OMCTS molecules. A molecule in the first layer usually has one of two possible well defined orientations: The inner Si-O-ring can be oriented parallel or perpendicular to the carbon wall. Either way, four CH_3 lie in the first layer. If the ring is in parallel, these are four functional groups positioned at one side of the inner ring and bonded each to another Si atom. The four functional groups on the opposite side of the ring lie in the second layer. If the molecule is oriented perpendicular, four CH_3 of two neighboring Si atoms are part of the first layer and the other four CH_3 lie in the third layer.

Concerning ethanol, the layering is not as clear cut as for decane and OMCTS. This can be seen in the radial density profiles for the individual constituents: methyl, methylene, oxygen and hydrogen (Fig. 43, lower plots). Like for water, first and second ethanol layer are not separated by a region of zero density. In addition, some peaks exhibit more than one maximum, evidence of a more complicated self assembly of the ethanol molecules. Furthermore, a high sensitivity of the molecular organization to curvature is observed: Density distributions next to a plane graphene sheet and next to a CNT differ significantly, even for a radius as large as 2.7 nm. For all other liquids considered so far, low wall curvature induced only small density changes in proximity to the wall.

To sum up the static equilibrium properties of confined decane, ethanol and OMCTS in comparison to water, we find globally a similar behavior: the liquid/wall interaction leads to an accumulation of liquid in proximity of the wall. With increasing distance from the wall, this dense liquid layer of molecular thickness is followed by a zone of depletion, and then eventually by a second molecular layer passing into the bulk region. But there are also subtle differences caused by the variations of molecular size and shape of the considered liquids. For example, one layer of OMCTS molecules is equivalent to three layers of CH_3 pseudo-atoms. Additionally to the static properties, we also noted differences in the dynamic behavior: A simple visual observation of the time evolution of the molecule positions (with the standard visualization software VMD [42]) reveals that the exchange rates of interface and bulk molecules for decane and OMCTS is dramatically smaller than for water. We did not perform a more quantitative evaluation of the particle dynamics, since the effect we are mainly interested in, namely the *curvature dependent friction* is predominantly set by static properties, i.e. the rms force.

13.3 Liquid/graphite friction for larger molecules

We measured the liquid/solid friction coefficient for decane, ethanol and OMCTS inside armchair CNT and in graphene slabs. To this end, we performed mostly equilibrium simulations using the same technique as before for water – namely, linking the friction via Green-Kubo formula to the equilibrium force fluctuations. For ethanol and decane in CNT, the friction coefficient was also measured in flow simulations to verify that the liquid structure was not affected by the flow.

In the following, results for the equilibrium measurement of the friction coefficient will be presented and discussed on the basis of our newly gained understanding for the water/ graphite friction. First, the interest lies on the influence of confinement and curvature on friction, and then the relation between friction and rms force is considered. Finally, the theoretical estimation Eq. (35) of the rms force is adapted to molecules made of more than one atom type.

13.3.1 Curvature dependent friction

In the considered systems, all three liquids show the same qualitative behavior as water: the friction coefficient is curvature dependent; it decreases with the tube radius (compare Fig. 44). For ethanol and decane, results for the friction coefficient are even lower than for water. The value we find for friction on graphene at large confinements, is about 30% smaller for ethanol and over 50% smaller for decane. Contrarily, the result for OMCTS is about a factor 4 higher. But the significance of this quantitative comparison is limited by the accuracy of the applied liquid models, which remain unknown as long as there is no quantitative experimental data available. That is why we keep the focus on a qualitative comparison and understanding. The first key result of these simulations is, that CNT act as fast transporters not only for water, but also of other liquids like alcanes, alcohol, ...

Although the general behavior is the same as for water, we also note some liquid-specific characteristics. For decane, the friction coefficient exhibits a certain dependence on confinement which become eminent in the graphene slab simulations with slab size $H < 3\,\mathrm{nm}$. This is not the case for ethanol and OMCTS (and water). Furthermore, for decane and OMCTS, we find a surprisingly large discrepancy between the results for graphene and CNT even for tube radii as large as $3-5\,\mathrm{nm}$.

In the following, the same theoretical analysis of the friction coefficient and the rms force that was discussed in detail for water in the above sections, will be applied to the other liquids.

Curvature dependence of the friction coefficient

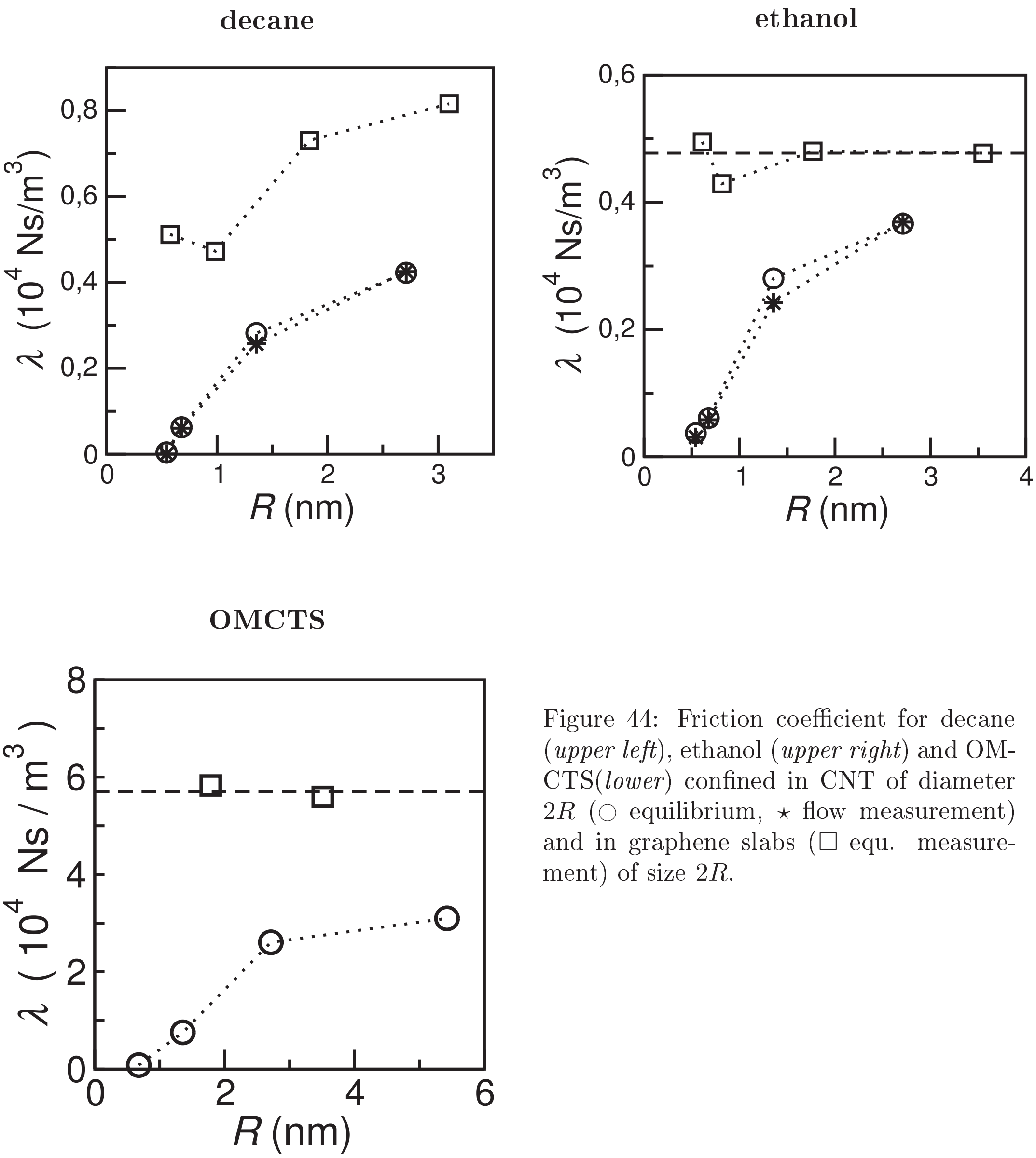

Figure 44: Friction coefficient for decane (*upper left*), ethanol (*upper right*) and OMCTS(*lower*) confined in CNT of diameter $2R$ (○ equilibrium, ⋆ flow measurement) and in graphene slabs (□ equ. measurement) of size $2R$.

13.3.2 Application of the theory for the rms force to organic liquids

First the relation $\lambda \propto \langle F^2 \rangle / \mathcal{A}$ is tested. The positive correlation between friction coefficient and the rms force is still valid (compare left plots of Fig. 45), but changes of the correlation time play a more important role than for water (deviations from dashed line through origin). At this point, we mention that changes in τ are not necessarily systematically connected to confinement, since the proportionality of friction and rms force works best for decane where an influence of confinement on the friction was observed. This means that, in this case and contrarily to our findings for water, the confinement changes the rms force, but not the decorrelation time. On the other hand, for ethanol and OMCTS that have a confinement independent interface friction on graphene, τ seems to change and influence friction. As to the reason for the different decorrelation time, no explanation can be given without studying the confined liquid dynamics. The following paragraphs are focused on the static analysis of the rms force.

One more complication enters the theoretical analysis: contrary to water and OMCTS, where only one atom type (CH_3 being treated as one functional group) interacts with the carbon wall, several distinct atom types contribute to the liquid-wall force in the case of decane and ethanol. The force thus has to be resolved into the contributions of the various atom types i: $F = \sum_i F^{(i)}$. The auto correlation function reads

$$\langle F(t)F(0)\rangle = \sum_i \left\langle F^{(i)}(t)F^{(i)}(0)\right\rangle + \sum_{i\neq j} \left\langle F^{(i)}(t)F^{(j)}(0)\right\rangle \tag{48}$$

It turns out that the mixed parts $\langle F^{(i)}(t)F^{(j)}(0)\rangle$ are negligible compared to the first sum. We can therefore conveniently write the friction coefficient as the sum

$$\lambda = \beta \sum_i \tau^{(i)} \frac{\left\langle (F^{(i)})^2 \right\rangle}{\mathcal{A}^{(i)}} \approx \beta \sum_i \tau^{(i)} \frac{N_1^{(i)}}{\mathcal{A}^{(i)}} (f_{q_{||}}^{(i)})^2 S^{(i)}(q_{||}) \tag{49}$$

Calculating independently the contact density $N_1/\mathcal{A}$, the force field amplitude $f_{q_{||}}$ and the static structure factor of the first layer $S(q)$ for each atom type allows estimating the rms force for liquids with a more complicated molecular structure. In Fig. 45 (right plots), we compare left and right hand side of Eq. (49) for the considered liquids and we find that the estimation qualitatively reproduces the results for the rms force also for polyatomic molecules. Furthermore, the quantitative agreement is also reasonable: For decane, ethanol and OMCTS in CNT, the approximation $\sum_i \tau^{(i)} N_1^{(i)} (f_{q_{||}}^{(i)})^2 S^{(i)}(q_{||})$ underestimates the rms force $\langle F^2 \rangle$ roughly by a factor of 4, 2, and 10, respectively. This is the same or a better degree of quantitative agreement as it was found for water. However, we also note a discrepancy for graphene and CNT results in case of ethanol. The rms force for ethanol on graphene seems not to be predicted well, in comparison to the CNT results. The data points for graphene deviate clearly from the line through origin defined by the CNT data points. A plausible explanation for this lies in the different density profiles for graphene and CNT, and the fact that the theoretical expression assumes an infinitely thin layer

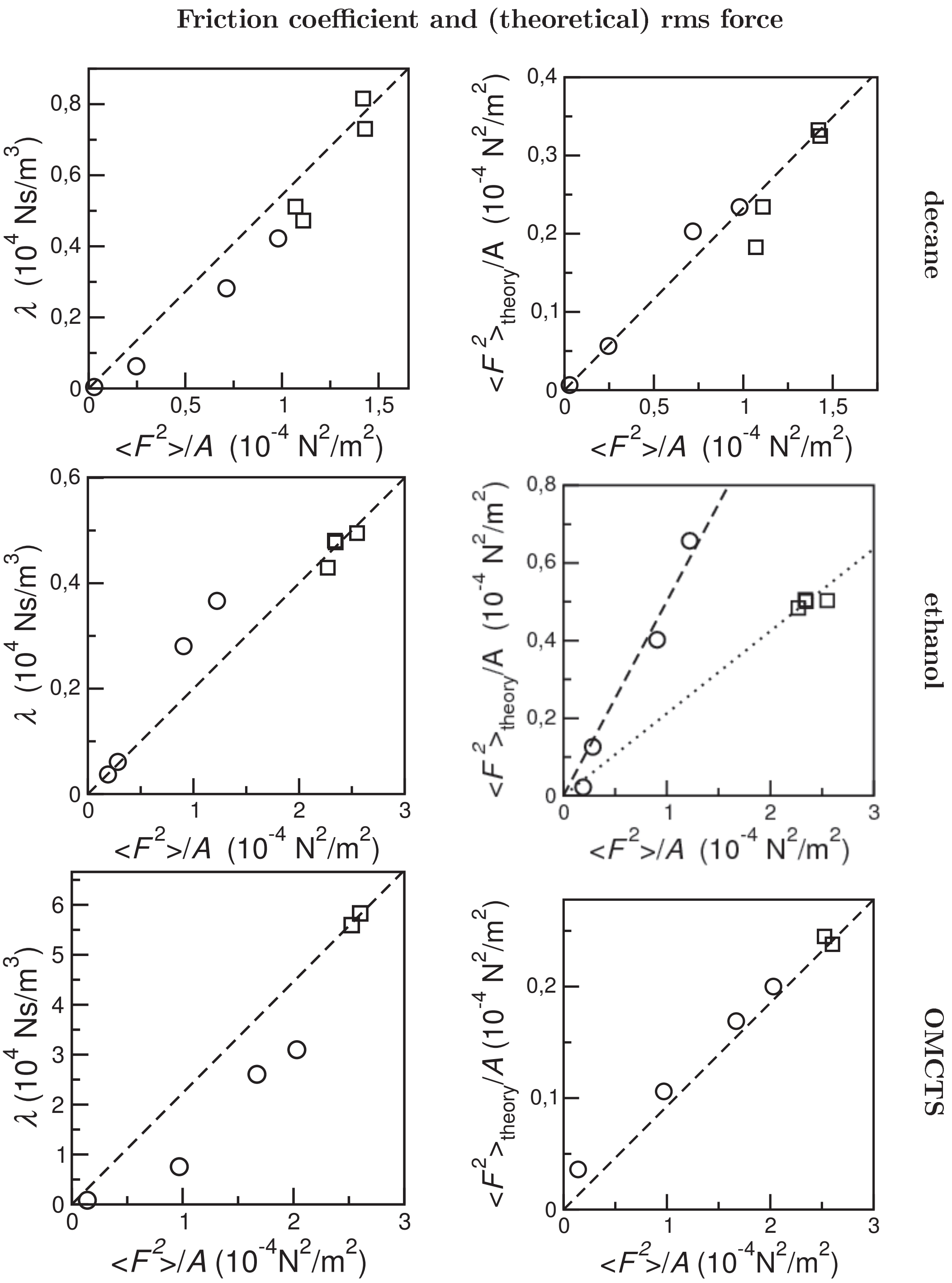

Figure 45: Friction coefficient versus static rms force (*left*) and the theoretical expression Eq. (49) versus the measured rms force (*right*) for decane (*upper*), ethanol (*middle*) and OMCTS (*lower*); ○ CNT, □ graphene

at distance σ of the wall. Deviations between the rms force and its approximation are mainly due to this projection (section 10), because a fluid particle that is closer to the wall feels an exponentially higher roughness. The exact form of the density distribution at the interface is thus responsible for the quantitative differences between the rms force and the approximate expression. Since the interface layer of ethanol in proximity of graphene takes a different form than in CNT, the quality of the approximation is also not the same. This is why in Fig. 35, we observe different slops for the ethanol/graphene and ethanol/CNT results of the rms force.

Overall, the theoretical framework for liquid/solid friction, whose development was based on the water/graphite simulation results, also offers a pertinent description of liquid/graphite friction for other liquids than water. In the following, we benefit from this fact to examine closely the interface properties determining the rms force. The aim of this considerations is to check if the curvature dependence of the friction coefficient is due to the same physical effects that have been identified in case of water, namely smoothing of the potential roughness and structural incommensurability.

13.3.3 Microscopic effects that influence liquid/graphite friction

Three interface characteristics fix the amount of friction according to Eq. (49): contact density $\frac{N_1}{\mathcal{A}}$, static structure factor $S(q_\parallel)$ and force field Fourier coefficient $f_{q_\parallel}$. For molecular liquids built of more than one atom type i, each type adds independently to the rms force $\langle F^2 \rangle \approx \sum_i \langle (F^{(i)})^2 \rangle$ and hence, the three contributions are evaluated individually for each atom type. For water in armchair CNT, the curvature dependence of the friction coefficient was found to stem mainly from an interplay of two effects. Firstly, incommensurability between the lateral structure of the interfacial water and the CNT structure play a crucial role. It is in large parts responsible for the decreasing friction in armchair CNT of diameters $> 1\,\text{nm}$. Secondly, curvature induces a smoothing of the lateral potential felt by the water molecules in proximity to the wall inside the tube. In particular, (almost) vanishing potential roughness leads to quasi-frictionless motion of single file water in $(5,5)$ and $(6,6)$ armchair CNT. In the following, the mentioned three contributions are evaluated for decane, ethanol and OMCTS, and compared to the findings for water, in order to establish which effect(s) lie at the origin of the curvature dependent friction in the case of these liquids. A graphical representation of the curvature dependence of all contributions for each liquid and atom type can be found in Appendix D.

Contact density The curvature dependence of the contact densities is similar for all atom types figuring in the considered liquids. For a detailed discussion of the curvature dependence of the contact density, we refer to the comparison of the results for water in armchair and zigzag CNT in section 9.

Static structure factor For water inside and outside armchair CNT, the lateral two dimensional structure of the first water layer was found to be isotropic and independent of the tube radius in low confinement. Changes of the (in)commensurability, quantified by the structural contribution $S(q_{\|})$, were due to the curvature induced deformation of the lateral oxygen potential and hence of the wave vector $q_{\|}$. Now, not only is the molecular size of decane, ethanol and OMCTS bigger than the one of water, but they also have different shapes. As already described in the course of the discussion of the density profiles, decane and OMCTS exhibit preferential orientations with respect to the graphene wall. On graphene, the molecular axes of the relatively stiff rod-like decane molecules lie parallel to the wall for the first decane layer. Similarly, the plane defined by the inner silicon-oxygen ring of one OMCTS molecule lies either parallel or perpendicular to the graphene wall.

Decane molecules, in particular, also tend to self organize. Domains of parallel aligned decane molecules can extend over several nanometers and can be stable for $\sim 10^{-10}\,\mathrm{s}$, a consequent fraction of the total simulation time. Snapshots of the interface decane layer on graphene show that some directions given by the hexagonal graphene grid seem to be favored for this alignment. This leads to anisotropies in the static structure factor $S(\mathbf{q})$. However, we have to mention that the measured anisotropy might also be a consequence of insufficient statistics: Due to size and stability of the self organized domains, we suspect that spatial and temporal averages have been too short to sample the complete configuration space.

Contrary to the other liquids, we observed an influence of confinement on the friction for decane in a graphene slab. In fact, the friction coefficient measured for slab sizes 1.15 and 1.97 nm is smaller compared to lower confinements. The effect is well captured with the approximate rms force (see Fig. 45). The reason for this friction decrease in small graphene slabs is an ordering throughout the whole slab height that changes the decane interface structure factor and thus the decane/graphene commensurability $S(q_{\|})$. In fact, the bulk region disappears and decane arranges in layers (2 layers for $H = 1.15\,\mathrm{nm}$; 4 for $H = 1.97\,\mathrm{nm}$) that influence each other: In this case, the mentioned domains of parallel aligned molecules occurred not only within one layer, but extended over all layers, which increases their stability and changes the decane structure factor at the interface.

In CNT, the tube geometry introduces a preferential direction for the decane molecules – they tend to orientate parallel to the tube axis. Contrarily to water, the decane interface structure is radius dependent. For higher curvature, more and more molecules reorientate themselves to evade bending that the wall curvature imposes in angular direction. This observation is in agreement with simulation results for decane structure in CNT from Supple and Quirke [94]. Consequently, two effects add to the curvature dependence of the structure contribution $S(\mathbf{q}_{\pm})$. Firstly, the wave vectors $\mathbf{q}_{\pm}$ change in length and direction. We are already familiar with this mechanism from the water study. Although for water, we only cared for the changing length of the wave vector, its direction being irrelevant for isotropic $S(q)$. And secondly, the form of the structure factor itself is influenced by the CNT size, in fact, it becomes more and more anisotropic for decreasing diameter. The interplay of both effects – changing decane structure and changing wave vector $q_{\|}$ – results in an non-systematic curvature dependence of the contribution $S(q_{\|})$.

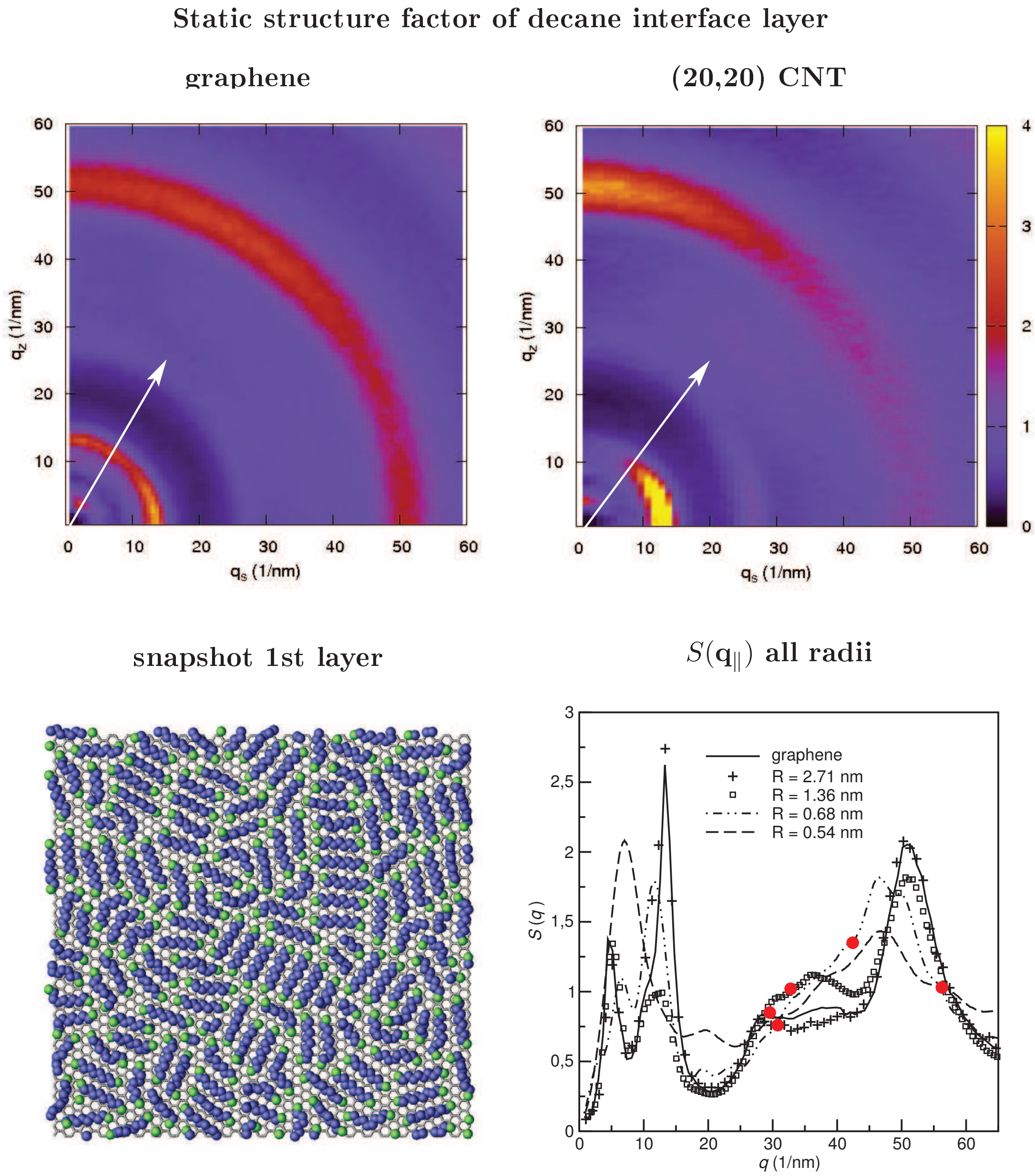

Static structure factor of decane interface layer

graphene

(20,20) CNT

snapshot 1st layer

$S(\mathbf{q}_{\|})$ all radii

Figure 46: First liquid layer for decane/graphite interfaces. *Lower left*: The rod-like decane molecules adhere parallel to the wall and build a liquid layer of molecular thickness. *Upper*: 2-dimensional static structure factor of the interface decane layer on graphene (*upper left*) and in a CNT with radius 1.36 nm (*upper right*). For decreasing tube diameter, the decane molecules align more and more in the direction of the tube axis, and the structure factor gets anisotropic. *Lower right*: Static structure factor of all considered decane/graphite systems in direction of the wave vector $\mathbf{q}_{\|}$ determining the periodic liquid/wall potential. Due to the developing anisotropy, $S(\mathbf{q})$ changes drastically with the radius. Furthermore, length and direction of $\mathbf{q}_{\|}$ are radius-dependent (white vectors). This leads to an unsystematic curvature dependence of the commensurability factor $S(\mathbf{q}_{\|})$ (marked with the red dots). Note that the displayed structure factors are the ones for the CH_2-pseudo-atoms (blue blobs in the snapshot); two characteristic lengths appear in the SF, the intramolecular bond length, and the distance between two parallel aligned decane molecules.

Here, we focused on decane because its simple shape makes its structural rearrangement at curved walls easily understandable. But anisotropic and/or curvature dependent structure factors were also found for OMCTS and ethanol. No specific incommensurability with the armchair CNT structure was observed for any of these liquids.

Potential roughness The Fourier coefficient $f_{q_\|}$ which is a a good measure for the roughness (= amplitude) of the force field depends only on the Lennard-Jones parameters for the interaction between liquid and wall atoms. Given that σ for the various liquid atom types are all similar, it is not surprising to find qualitatively the same radius dependence of $f_{q_\|}$ as for water. The roughness inside armchair CNT is decreasing with increasing curvature.

13.4 Summary and outlook

Our simulation results suggest that a variety of fluids, like water, alcohols and hydrocarbons exhibit all a very similar flow behavior in graphitic nano systems like graphene slabs or carbon nanotubes: Flow rates lie far above what could be expected from the hydrodynamic no-slip boundary condition, due to extremely low friction on the carbon wall. This leads to plug flow instead of the parabolic velocity profiles found without slippage. Furthermore, in the CNT systems we studied so far (armchair CNT for decane, ethanol, OMCTS and water; zigzag CNT for water), the friction coefficient is decreasing further for increasing curvature, favoring fast fluid transport even for CNT with very small cross sections (diameter comparable to the molecular size). This curvature induced decrease of the friction coefficient can be understood within the theory presented in part III. Changes in the friction coefficient are directly related to changes in the equilibrium rms force between liquid and carbon wall. The rms force, in turn, is determined by three interfacial properties: liquid contact density, wall roughness and (in)commensurability of wall structure and the structure of the liquid interface layer. This description works very well for all considered liquids.

One step further: prediction for zigzag CNT/decane However, an evaluation of the various contributions to the static rms force reveals a striking difference between water and the liquids considered in this part: for the latter incommensurability does *not* play a role for the small friction coefficient and its curvature dependence. On the contrary, the structure factor $S(q_\|)$ is mostly larger then one and if any change with curvature was observed it was increasing by trend. For decane, ethanol and OMCTS, a systematic decrease with curvature is only observed for the contact density and the potential roughness. Although this results still in the same overall trend for the friction coefficient in *armchair* CNT, it might well be very different in *zigzag* CNT. Remember that contrarily to armchair CNT, the roughness of the force field inside zigzag CNT is *increasing* for small radii. If in parallel to a higher roughness, the structure contribution changes unpredictably because the liquid adapts to the wall curvature, the behavior of the friction coefficient is equally unforeseeable. If no incommensurability occurs to counter the higher roughness in zigzag CNT, a much higher friction is expected compared to an armchair CNT of similar (small) radius. We checked this for decane in a (0,14) CNT ($R = 0.55$nm) and we found indeed a friction coefficient $\lambda \approx 1.2 \times 10^4 \, \frac{\mathrm{Ns}}{\mathrm{m}^3}$ – a value that is 300 times higher than in the (8,8) CNT ($R = 0.54\,\mathrm{nm}$).

Conclusion and outlook

At last, the important aspects of the presented work are again briefly summarized, before we conclude with an outlook on perspective future work.

Aim of this study This work was motivated by the astonishing results of other groups that previously performed experimental measurements of carbon nanotube (CNT) membrane permeabilities. They reported exceptionally high liquid throughput due to ultra fast fluid transport in CNT. The measured flow rates exceeded the expectation from the classical hydrodynamics description with no-slip boundary conditions by several orders of magnitude. These flow rates imply slip length from several hundred nanometers up to micrometers. This is far above the expectation for atomically smooth non-wetting liquid/solid interfaces. Previous measurements on other interfaces of this type resulted in slip length of only a few nanometers. Such a low-friction transport of liquids in nanopores is otherwise only known from biological systems like, for example, cell membrane pores (aquaporines). Carbon nanotube membranes that reproduce the efficiency of these biological filters would offer promising perspectives for applications like, for example, water desalination by reverse osmosis. But up to now, the reason for the large slippage in CNT was unclear, leaving the experimental results unconfirmed by any theory.

The aim of this study was therefore to reassess the occurrence of fast fluid transport in carbon nanotubes as it was previously measured experimentally with molecular dynamics simulations. Furthermore, we wanted to give a theoretical description of liquid/solid friction on graphitic surfaces in order to identify the underlying mechanisms controlling friction.

Molecular dynamics measurement of the liquid/solid friction coefficient The liquid/solid friction occurring for laminar fluid flow in graphitic nanopores was investigated with molecular dynamics simulations. More precisely, the friction coefficient λ that characterizes the linear response $F = -\lambda \mathcal{A} v_{\text{slip}}$ between friction force and slip velocity, was measured for different liquids, geometries and confinements: The considered geometries were 'liquid inside' or 'outside of carbon nanotube' and 'liquid in graphene slab'. The confinement was varied by changing the tube radius and the slab size. The friction coefficient was measured in two independent ways for four different liquids, namely water, ethanol, decane and OMCTS. One method consisted of directly measuring friction force and slip velocity in flow simulations. The second method made use of a Green-Kubo relation for the friction coefficient which allowed to determine λ in equilibrium simulations.

Our simulation results show that the friction coefficient is independent of confinement, but strongly dependent on curvature: While results in the graphene slab geometry were constant for changing slab size, the friction coefficient in CNT decreases considerably with the tube radius. In the smallest armchair CNT, water arranged in single file flowed almost frictionless. The simulation results confirm experimentally measured flow rate enhancements up to 10^3.

Theoretical description of the low friction We presented a theoretical description of liquid/solid friction based on the Green-Kubo relation $\lambda = \beta\tau_F\langle F^2\rangle/\mathcal{A}$ with $\tau_F = \int_0^\infty \mathrm{d}t\langle F(t)F(0)\rangle/\langle F^2\rangle$ the decorrelation time of the force autocorrelation function. It turned out that the curvature dependence is almost exclusively due to a changing rms force $\langle F^2\rangle$. Only in high confinement where the liquid structure is affected by the confinement, changes in the dynamical properties of the liquid add to the curvature dependence of the friction coefficient. Subsequently, the derivation of an approximate expression for the rms force revealed that it is directly linked to three interface properties (of the first layer of liquid molecules adhering to the wall and of the wall itself). These properties are the liquid surface density, the roughness of the wall potential felt by the liquid molecules in the first layer and a commensurability factor measuring the amount of (mis)match between the structure of the potential and of the liquid. In the low confinement regime $R > 1\,\mathrm{nm}$, these three quantities determine the behavior of the friction coefficient. The wall structure plays a particularly important role since it determines the wall roughness and enters also into the commensurability factor. For example, armchair CNT get smoother with decreasing radius, while the roughness of zigzag CNT increases. Remarkably, for water, the friction coefficient decreases in both cases, albeit less in zigzag CNT. This is not necessarily the case for all liquids as a test with decane demonstrated: For a comparable radius about 5Å, the friction coefficient was two orders of magnitude larger for zigzag than for armchair chirality. Altogether, the proposed theoretical description explains the curvature dependence of the friction coefficient in armchair CNT for all considered liquids. Furthermore, it also catches the dependence of the friction coefficient on the CNT chirality that was observed for water in armchair and zigzag CNT. We have thus achieved our objective in obtaining a good understanding of the physical origin of fast fluid transport in carbon nanotubes. Partly, these results have been published in Ref. [22] (results for water).

Perspectives Based on the presented theory it is now possible to make predictions for flow rates in different systems. Since our results suggest that the structure of the wall and the liquid are a crucial factor, further investigations of the influence of the CNT chirality might permit to find liquid/nanotube combinations with particularly low friction. For this, the high confinement regime is especially interesting since it favores strong ordering of the liquid molecules, like single file water, for example. In principle, such crystalline structures offer the possibility of frictionless sliding due to complete incommensurability (zero liquid structure factor at the characteristic wave length of the potential). Therefore, it would also be very interesting to investigat the transport of larger molecules, like DNA or other bio-polymeres, where the breakdown of the hydrodynamic theory which marks the onset of high confinement, occures at larger system sizes. Lowering the temperature or increasing the pressure is a further possibility to influence the liquid structure inside CNT: For water, ice-like structures in CNT under different p, T-conditions than for bulk water were found experimentally and in simulations [52, 53]. Another option for polar liquids might be to induce or change a preferred orientation with an external electric field, to use charged CNT [39], or to add ions to the liquid. In particular, transport properties of aqueous salt solutions are a very relevant topic concerning the mentioned applications, *e.g.* energy conversion. To pursue all these ideas, further MD investigations would be useful.

Above all, however, a direct comparison to experimental results would be needed to validate the proposed molecular theory for liquid/solid friction and the liquid models that were applied in the simulations. The results of the presented study are in agreement with the mentioned flow experiments with 2 nm-CNT membranes [38]. On the other hand, results for flow rates in 7 nm-CNT were far higher than our predictions [67]. A possible reason for this is an underestimation of the available flow cross section in this experiment since the production and characterization of CNT-membranes is a delicate task. Accordingly, no systematic experimental investigation exists so far to check the influence of CNT radius and chirality. The ultimate goal for such a study would be the flow rate measurement through a single CNT with well defined geometric and structural properties. Performing such measurements is certainly a very challenging problem. First steps in this direction have recently been successfully taken from a collaboration led by the group 'Liquids and Interfaces' in the LPMCN (University Lyon 1): Silicon nitride membranes perforated by a single carbon or boron nitride nanotube have been manufactured. Others have made advances in separating CNT with different conducting properties which are directly linked to chirality [62]. But important obstacles still have to be overcome to conduct a significant flow measurement as well as to largely control the CNT properties. However, keeping in mind our theoretical predictions and their prospective applications, it seems certainly worth the effort to pursue this challenging road.

Appendix

A Structure factor of a one dimensional bead-spring chain

The structure of single file water in a rigid CNT of sub-nanometer diameter can be quite accurately described with a simple bead-spring model. The structure factor of such a system has been found to match the simulated system very well. In the following, we calculate the form of the structure factor.

The density of a N-particle chain is given by

$$\rho(z) = \sum_{i=1}^{N} \delta(z_i - z) \tag{50}$$

and the potential energy of the system is

$$V = \sum_{j} \frac{\kappa}{2} y_j^2 \ . \tag{51}$$

where y_j is the elongation of spring j between particles $j-1$ and j. The structure factor can be expressed as a function of the spring elongations:

$$\begin{aligned} S(q) &= \frac{1}{N} \int_{-\infty}^{\infty} \int_{-\infty}^{\infty} \mathrm{d}z \mathrm{d}z' \ \mathrm{e}^{\mathrm{i}q(z-z')} \left\langle \rho(z) \rho(z') \right\rangle \\ &= 1 + \frac{1}{N} \sum_{j=1}^{N-2} \sum_{l=j+1}^{N-1} \left\langle \prod_{m=j+1}^{l} \mathrm{e}^{\mathrm{i}q(y_m + z_0)} + \prod_{m=j+1}^{l} \mathrm{e}^{-\mathrm{i}q(y_m + z_0)} \right\rangle . \end{aligned} \tag{52}$$

With the canonical ensemble average

$$\left\langle \prod_{m=j+1}^{l} \mathrm{e}^{\pm \mathrm{i}q(y_m + z_0)} \right\rangle = \mathrm{e}^{(l-j)\left(-\frac{q^2}{2\beta\kappa} \pm \mathrm{i}qz_0\right)} \tag{53}$$

where $\beta = 1/k_{\mathrm{B}}T$, and with the thermodynamic limit $N \rightarrow \infty$, the structure factor reads

$$S(q) = \frac{1 - \mathrm{e}^{\frac{-q^2}{\beta\kappa}}}{1 - 2\mathrm{e}^{\frac{-q^2}{2\beta\kappa}} \cos(qz_0) + \mathrm{e}^{\frac{-q^2}{\beta\kappa}}} . \tag{54}$$

B Lateral force field for different oxygen-to-wall distances

In section 10, the dependence of the force field amplitude on the distance to the wall was presented. An exponential decay with increasing distance was observed. Additionally, we note that the form of the potential is qualitatively the same over the whole position of the first water. The form changes rather abruptly in the region between the first and the second water layer, around 1.5σ (compare also Fig. 38).

Normalized lateral force field in z-direction acting on a water molecule at distance D from a CNT $R = 1.36\,\mathrm{nm}$

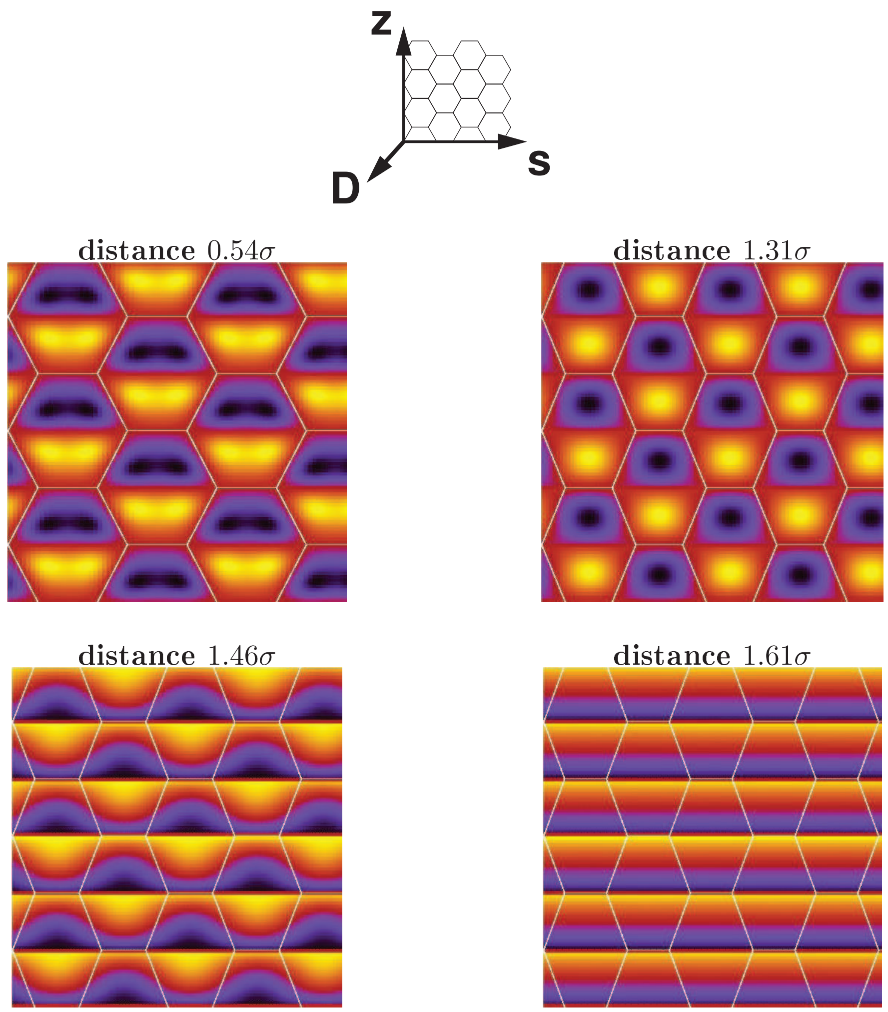

Figure 47: Force in z-direction that is exerted on one oxygen atom at a certain distance D to the wall (armchair CNT with $R = 1.36$), depending on its lateral position ($s = r\theta$,z). The force is normalized to the interval -1 (black) to 1 (yellow). The white lines correspond to the CNT structure, projected on the radial position $r = R - D$ of the water molecule.

C Geometry and dihedral potential for ethanol and decane

Decane and ethanol are modeled with the optimized potential for liquid simulations (OPLS). Bond length and angles are fixed. The geometry as well as the position of charges in case of ethanol, is sketched below. Torsion of bonds is possible, but limited by the dihedral potential

$$V(\Phi) = \frac{1}{2}V_1(1 + \cos\ \Phi) + \frac{1}{2}V_2(1 - \cos\ 2\Phi) + \frac{1}{2}V_3(1 + \cos\ 3\Phi) \tag{55}$$

with the dihedral angle Φ as defined in Fig. 48 and the following coefficients V_1, V_2 and V_3:

	V_1	V_2	V_3 (kcal/mol)
decane (C-C-C-C)	1.411	−0.271	3.145
ethanol (C-C-O-H)	0.834	−0.116	0.747

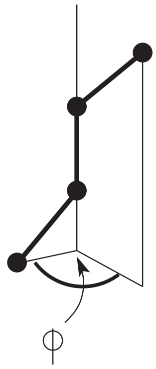

Figure 48: dihedral angle

Additionally to these model parameters for the intramolecular interactions, Lennard Jones and Coulomb potential determine intermolecular interactions. The LJ parameters and charges are given in the main text (section 13.1, Tab.13.1 on page 99).

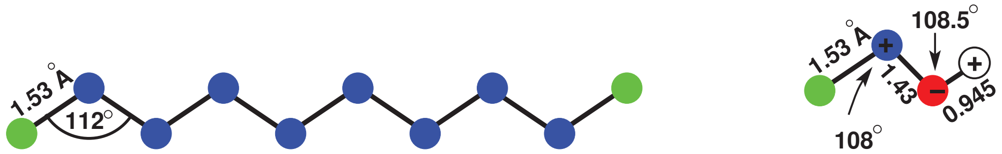

Figure 49: Geometry of decane (*left*) and ethanol molecule (*right*).
CH_2 pseudo-atoms are colored blue, CH_3 green, O red and charged H white.

D Contributions to rms force for OMCTS, decane, ethanol

Surface density, potential roughness and structure factor for OMCTS, decane ethanol

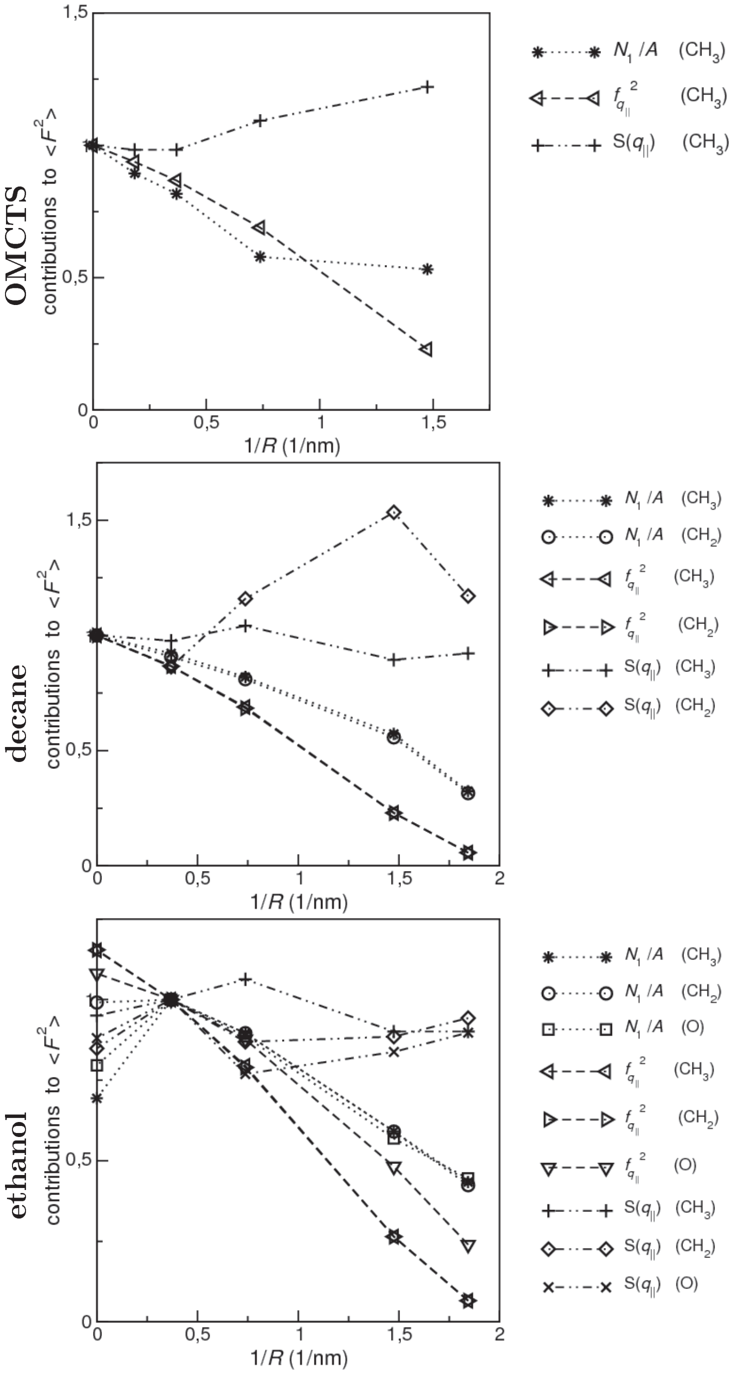

Figure 50: Curvature dependence of the different contributions to the rms force of all constituent (pseudo)atom types for OMCTS, decane and ethanol. For OMCTS and decane, all values are normalized to the respective values for the graphene slab geometry (zero curvature). For ethanol, normalization was performed on the values of the largest considered CNT, because of the discrepany between the result for the approximate rms for graphene and for CNT (see Fig. 45).

References

[1] Alessio Alexiadis and Stavros Kassinos. Molecular simulation of water in carbon nanotubes. *Chemical Reviews*, 108(12):5014–5034, 2008.

[2] J. L. Barrat and L. Bocquet. Influence of wetting properties on hydrodynamic boundary conditions at a fluid/solid interface. *Faraday Discussions*, 112(112):119–127, 1999.

[3] J. L. Barrat and L. Bocquet. Large slip effect at a nonwetting fluid-solid interface. *Physical Review Letters*, 82(23):4671–4674, 1999.

[4] Thomas Becker and Frieder Mugele. Nanofluidics: Viscous dissipation in layered liquid films. *Phys. Rev. Lett.*, 91(16):166104–, October 2003.

[5] Alexander Berezhkovskii and Gerhard Hummer. Single-file transport of water molecules through a carbon nanotube. *Phys. Rev. Lett.*, 89(6):064503–, July 2002.

[6] L. Bocquet and J. L. Barrat. Hydrodynamic boundary-conditions, correlation-functions, and kubo relations for confined fluids. *Physical Review E*, 49(4):3079–3092, 1994.

[7] L. Bocquet and J. L. Barrat. Flow boundary conditions from nano- to micro-scales. *Soft Matter*, 3(6):685–693, 2007.

[8] Lyderic Bocquet and Elisabeth Charlaix. Nanofluidics, from bulk to interfaces. *Chem. Soc. Rev.*, 39(3):1073–1095, 2010.

[9] P A Bonnaud, B Coasne, and R J-M Pellenq. Molecular simulation of water confined in nanoporous silica. *Journal of Physics: Condensed Matter*, 22(28):284110, 2010.

[10] D. J. Bonthuis, K. Falk, C. N. Kaplan, D. Horinek, A. N. Berker, L. Bocquet, and R. R. Netz. Comment on "pumping of confined water in carbon nanotubes by rotation-translation coupling". *Phys. Rev. Lett.*, 105(20):209401–, November 2010.

[11] Donald W. Brenner. Empirical potential for hydrocarbons for use in simulating the chemical vapor deposition of diamond films. *Phys. Rev. B*, 42(15):9458–, November 1990.

[12] Bing-Yang Cao, Jun Sun, Min Chen, and Zeng-Yuan Guo. Molecular momentum transport at fluid-solid interfaces in mems/nems: A review. *International Journal of Molecular Sciences*, 10(11):4638–4706, 2009.

[13] Antoine Carre, Ludovic Berthier, Jurgen Horbach, Simona Ispas, and Walter Kob. Amorphous silica modeled with truncated and screened coulomb interactions: A molecular dynamics simulation study. *The Journal of Chemical Physics*, 127(11):114512, 2007.

[14] D. Y. C. Chan and R. G. Horn. The drainage of thin liquid films between solid surfaces. *J. Chem. Phys.*, 83(10):5311–5324, November 1985.

[15] Wendy D. Cornell, Piotr Cieplak, Christopher I. Bayly, Ian R. Gould, Kenneth M. Merz, David M. Ferguson, David C. Spellmeyer, Thomas Fox, James W. Caldwell, and Peter A. Kollman. A second generation force field for the simulation of proteins, nucleic acids, and organic molecules. *Journal of the American Chemical Society*, 117(19):5179–5197, 1995.

[16] C. Cottin-Bizonne, B. Cross, A. Steinberger, and E. Charlaix. Boundary slip on smooth hydrophobic surfaces: Intrinsic effects and possible artifacts. *Phys. Rev. Lett.*, 94(5):056102–, February 2005.

[17] Eduardo R. Cruz-Chu, Aleksei Aksimentiev, and Klaus Schulten. Water-silica force field for simulating nanodevices. *The Journal of Physical Chemistry B*, 110(43):21497–21508, November 2006.

[18] Sissi de Beer, Dirk van den Ende, and Frieder Mugele. Confinement-dependent damping in a layered liquid. *Journal of Physics: Condensed Matter*, 23(11):112206, 2011.

[19] P. G. de Gennes. On fluid/wall slippage. *Langmuir*, 18(9):3413–3414, April 2002.

[20] Jan C. T. Eijkel and Albert van den Berg. Nanofluidics: what is it and what can we expect from it? *Microfluidics and Nanofluidics*, 1(3):249–267, 2005.

[21] Pep Espanol and Ignacio Zuniga. Force autocorrelation function in brownian motion theory. *The Journal of Chemical Physics*, 98(1):574–580, 1993.

[22] K. Falk, F. Sedlmeier, L. Joly, R. R. Netz, and L. Bocquet. Molecular origin of fast water transport in carbon nanotube membranes: Superlubricity versus curvature dependent friction. *Nano Letters*, 10(10):4067–4073, 2010.

[23] John L. Finney. The water molecule and its interactions: the interaction between theory, modelling, and experiment. *Journal of Molecular Liquids*, 90(1-3):303–312, February 2001.

[24] Frederick M. Fowkes and William D. Harkins. The state of monolayers adsorbed at the interface solid—aqueous solution. *Journal of the American Chemical Society*, 62(12):3377–3386, 1940.

[25] Daan Frenkel and Berend Smit. *Understanding Molecular Simulation, Second Edition: From Algorithms to Applications (Computational Science Series, Vol 1).* Academic Press, 2nd ed. edition, 2001.

[26] J. M. Georges, S. Millot, J. L. Loubet, and A. Tonck. Drainage of thin liquid films between relatively smooth surfaces. *The Journal of Chemical Physics*, 98(9):7345–7360, 1993.

[27] Nicolas Giovambattista, Peter J. Rossky, and Pablo G. Debenedetti. Effect of pressure on the phase behavior and structure of water confined between nanoscale hydrophobic and hydrophilic plates. *Phys. Rev. E*, 73(4):041604–, April 2006.

[28] Yury Gogotsi, Joseph A. Libera, Almila Guvenc-Yazicioglu, and Constantine M. Megaridis. In situ multiphase fluid experiments in hydrothermal carbon nanotubes. *Appl. Phys. Lett.*, 79(7):1021–1023, August 2001.

[29] Xiaojing Gong, Jingyuan Li, He Zhang, Rongzheng Wan, Hangjun Lu, Shen Wang, and Haiping Fang. Enhancement of water permeation across a nanochannel by the structure outside the channel. *Phys. Rev. Lett.*, 101(25):257801–, December 2008.

[30] Miguel Angel Gonzalez and Jose L. F. Abascal. The shear viscosity of rigid water models. *J. Chem. Phys.*, 132(9):096101–2, March 2010.

[31] Simon Gruener, Tommy Hofmann, Dirk Wallacher, Andriy V. Kityk, and Patrick Huber. Capillary rise of water in hydrophilic nanopores. *Phys. Rev. E*, 79(6):067301–, June 2009.

[32] Simon Gruener and Patrick Huber. Spontaneous imbibition dynamics of an n-alkane in nanopores: Evidence of meniscus freezing and monolayer sticking. *Phys. Rev. Lett.*, 103(17):174501–, October 2009.

[33] Bertrand Guillot. A reappraisal of what we have learnt during three decades of computer simulations on water. *Journal of Molecular Liquids*, 101(1-3):219–260, November 2002.

[34] I. Hanasaki and A. Nakatani. Flow structure of water in carbon nanotubes: Poiseuille type or plug-like? *Journal Of Chemical Physics*, 124(14), 2006.

[35] Jean-Pierre Hansen and I. R. McDonald. *Theory of Simple Liquids, Third Edition.* Academic Press, 3rd edition, 2006.

[36] Jean-Pierre Hansen and Loup Verlet. Phase transitions of the lennard-jones system. *Phys. Rev.*, 184(1):151–, August 1969.

[37] Bruce J. Hinds, Nitin Chopra, Terry Rantell, Rodney Andrews, Vasilis Gavalas, and Leonidas G. Bachas. Aligned multiwalled carbon nanotube membranes. *Science*, 303(5654):62–65, January 2004.

[38] Jason K. Holt, Hyung Gyu Park, Yinmin Wang, Michael Stadermann, Alexander B. Artyukhin, Costas P. Grigoropoulos, Aleksandr Noy, and Olgica Bakajin. Fast mass transport through sub-2-nanometer carbon nanotubes. *Science*, 312(5776):1034–1037, May 2006.

[39] Boda Huang, Yueyuan Xia, Mingwen Zhao, Feng Li, Xiangdong Liu, Yanju Ji, and Chen Song. Distribution patterns and controllable transport of water inside and outside charged single-walled carbon nanotubes. *The Journal of Chemical Physics*, 122(8):084708, 2005.

[40] David M. Huang, Christian Sendner, Dominik Horinek, Roland R. Netz, and Lydéric Bocquet. Water slippage versus contact angle: A quasiuniversal relationship. *Phys. Rev. Lett.*, 101(22):226101–, November 2008.

[41] G. Hummer, J. C. Rasaiah, and J. P. Noworyta. Water conduction through the hydrophobic channel of a carbon nanotube. *Nature*, 414(6860):188–190, November 2001.

[42] William Humphrey, Andrew Dalke, and Klaus Schulten. Vmd: Visual molecular dynamics. *Journal of Molecular Graphics*, 14(1):33–38, February 1996.

[43] Sumio Iijima. Helical microtubules of graphitic carbon. *Nature*, 354(6348):56–58, November 1991.

[44] Richard L. Jaffe, Pedro Gonnet, Thomas Werder, Jens H. Walther, and Petros Koumoutsakos. Water–carbon interactions 2: Calibration of potentials using contact angle data for different interaction models. *Molecular Simulation*, 30(4):205–216, 2004.

[45] William L. Jorgensen. Optimized intermolecular potential functions for liquid alcohols. *The Journal of Physical Chemistry*, 90(7):1276–1284, 1986.

[46] William L. Jorgensen, Jeffry D. Madura, and Carol J. Swenson. Optimized intermolecular potential functions for liquid hydrocarbons. *Journal of the American Chemical Society*, 106(22):6638–6646, 1984.

[47] P. Joseph, C. Cottin-Bizonne, J.-M. Benoit, C. Ybert, C. Journet, P. Tabeling, and L. Bocquet. Slippage of water past superhydrophobic carbon nanotube forests in microchannels. *Phys. Rev. Lett.*, 97(15):156104–, October 2006.

[48] S. Joseph and N. R. Aluru. Why are carbon nanotubes fast transporters of water? *Nano Letters*, 8(2):452–458, 2008.

[49] Amrit Kalra, Shekhar Garde, and Gerhard Hummer. Osmotic water transport through carbon nanotube membranes. *Proceedings of the National Academy of Sciences*, 100(18):10175–10180, 2003.

[50] S. C. Kassinos, J. H. Walther, E. M. Kotsalis, and P. Koumoutsakos. Flow of aqueous solutions in carbon nanotubes. In S. Attinger and P. Koumoutsakos, editors, *Multiscale Modelling and Simulation*, Lecture Notes in Computational Science and Engineering. Springer New York, 2004.

[51] Martin Knudsen. Die gesetze der molekularströmung und der inneren reibungsströmung der gase durch röhren. *Ann. Phys.*, 333(1):75–130, 1909.

[52] Kenichiro Koga, G. T. Gao, Hideki Tanaka, and X. C. Zeng. Formation of ordered ice nanotubes inside carbon nanotubes. *Nature*, 412(6849):802–805, August 2001.

[53] Alexander I. Kolesnikov, Jean-Marc Zanotti, Chun-Keung Loong, Pappannan Thiyagarajan, Alexander P. Moravsky, Raouf O. Loutfy, and Christian J. Burnham. Anomalously soft dynamics of water in a nanotube: A revelation of nanoscale confinement. *Phys. Rev. Lett.*, 93(3):035503–, July 2004.

[54] E. M. Kotsalis, J. H. Walther, and P. Koumoutsakos. Multiphase water flow inside carbon nanotubes. *International Journal of Multiphase Flow*, 30(7-8):995–1010, July 2004.

[55] Eugenia Kumacheva and Jacob Klein. Simple liquids confined to molecularly thin layers. ii. shear and frictional behavior of solidified films. *J. Chem. Phys.*, 108(16):7010–7022, April 1998.

[56] E. Lauga, M.P. Brenner, and H.A. Stone. Microfluidcs: The no-slip boundary condition. In C. Tropea, A. Yarin, and J.F. Foss, editors, *Hanndbook of Experimental Fluid Mechanics*. Springer New York, 2007.

[57] Eric Lauga and Todd M. Squires. Brownian motion near a partial-slip boundary: A local probe of the no-slip condition. *Physics of Fluids*, 17(10):103102, 2005.

[58] Choongyeop Lee, Chang-Hwan Choi, and Chang-Jin "CJ" Kim. Structured surfaces for a giant liquid slip. *Phys. Rev. Lett.*, 101(6):064501–, August 2008.

[59] Yongsheng Leng and Peter T. Cummings. Fluidity of hydration layers nanoconfined between mica surfaces. *Phys. Rev. Lett.*, 94(2):026101–, January 2005.

[60] Tai-De Li, Jianping Gao, Robert Szoszkiewicz, Uzi Landman, and Elisa Riedo. Structured and viscous water in subnanometer gaps. *Phys. Rev. B*, 75(11):115415–, March 2007.

[61] Ying-Chun Liu, Jia-Wei Shen, Keith E. Gubbins, Joshua D. Moore, Tao Wu, and Qi Wang. Diffusion dynamics of water controlled by topology of potential energy surface inside carbon nanotubes. *Phys. Rev. B*, 77(12):125438–, March 2008.

[62] Fushen Lu, Mohammed J. Meziani, Li Cao, and Ya-Ping Sun. Separated metallic and semiconducting single-walled carbon nanotubes: Opportunities in transparent electrodes and beyond. *Langmuir*, 27(8):4339–4350, April 2011.

[63] Richard Lucas. Ueber das Zeitgesetz des kapillaren Aufstiegs von Flüssigkeiten. *Kolloid-Zeitschrift*, 23(1):15, 1918.

[64] Ming D. Ma, Luming Shen, John Sheridan, Jefferson Zhe Liu, Chao Chen, and Quanshui Zheng. Friction of water slipping in carbon nanotubes. *Phys. Rev. E*, 83(3):036316–, March 2011.

[65] Abdelhamid Maali, Touria Cohen-Bouhacina, Gerard Couturier, and Jean-Pierre Aime. Oscillatory dissipation of a simple confined liquid. *Phys. Rev. Lett.*, 96(8):086105–, March 2006.

[66] Michael W. Mahoney and William L. Jorgensen. A five-site model for liquid water and the reproduction of the density anomaly by rigid, nonpolarizable potential functions. *The Journal of Chemical Physics*, 112(20):8910–8922, 2000.

[67] Mainak Majumder, Nitin Chopra, Rodney Andrews, and Bruce J. Hinds. Nanoscale hydrodynamics: Enhanced flow in carbon nanotubes. *Nature*, 438(7064):44–44, November 2005.

[68] Pekka Mark and Lennart Nilsson. Structure and dynamics of the tip3p, spc, and spc/e water models at 298 k. *The Journal of Physical Chemistry A*, 105(43):9954–9960, 2001.

[69] Marcus G. Martin and J. Ilja Siepmann. Transferable potentials for phase equilibria. 1. united-atom description of n-alkanes. *The Journal of Physical Chemistry B*, 102(14):2569–2577, 1998.

[70] Hiroki Matsubara, Fabio Pichierri, and Kazue Kurihara. Design of a versatile force field for the large-scale molecular simulation of solid and liquid omcts. *Journal of Chemical Theory and Computation*, 6(4):1334–1340, 2010.

[71] Davide Mattia and Yury Gogotsi. Review: static and dynamic behavior of liquids inside carbon nanotubes. *Microfluidics and Nanofluidics*, 5(3):289–305, 2008.

[72] Meagan S. Mauter and Menachem Elimelech. Environmental applications of carbon-based nanomaterials. *Environmental Science & Technology*, 42(16):5843–5859, August 2008.

[73] Ikram Morcos. Surface tension of stress-annealed pyrolytic graphite. *The Journal of Chemical Physics*, 57(4):1801–1802, 1972.

[74] Kazuyoshi Murata, Kaoru Mitsuoka, Teruhisa Hirai, Thomas Walz, Peter Agre, J. Bernard Heymann, Andreas Engel, and Yoshinori Fujiyoshi. Structural determinants of water permeation through aquaporin-1. *Nature*, 407(6804):599–605, October 2000.

[75] Tim Myers. Why are slip lengths so large in carbon nanotubes? *Microfluidics and Nanofluidics*, pages 1–5, 2010. 10.1007/s10404-010-0752-7.

[76] Sumita Pennathur, Jan C.T. Eijkel, and Albert van den Berg. Energy conversion in microsystems: is there a role for micro/nanofluidics? *Lab Chip*, 7:1234–1237, 2007.

[77] Steve Plimpton. Fast parallel algorithms for short-range molecular dynamics. *Journal of Computational Physics*, 117(1):1 – 19, 1995.

[78] Steve Plimpton, Roy Pollock, and Mark Stevens. Particle-mesh ewald and rrespa for parallel molecular dynamics simulations. In *Parallel Processing for Scientific Computing*, 1997.

[79] J. Puibasset and R. J.-M. Pellenq. Grand canonical monte carlo simulation study of water adsorption in silicalite at 300 k. *The Journal of Physical Chemistry B*, 112(20):6390–6397, May 2008.

[80] D. C. Rapaport. *The Art of Molecular Dynamics Simulation.* Cambridge University Press, Cambridge, UK, 2nd edition, 2004.

[81] Uri Raviv and Jacob Klein. Fluidity of bound hydration layers. *Science*, 297(5586):1540–1543, 2002.

[82] Yongqiang Ren and Derek Stein. Slip-enhanced electrokinetic energy conversion in nanofluidic channels. *Nanotechnology*, 19(19):195707–, 2008.

[83] J. S. Rowlinson and B. Widom. *Molecular Theory of Capillarity.* Oxford University Press, 1989.

[84] Jean-Paul Ryckaert, Giovanni Ciccotti, and Herman J. C. Berendsen. Numerical integration of the cartesian equations of motion of a system with constraints: molecular dynamics of n-alkanes. *Journal of Computational Physics*, 23(3):327 – 341, 1977.

[85] A. Saugey, L. Joly, C. Ybert, J. L. Barrat, and L. Bocquet. Diffusion in pores and its dependence on boundary conditions. *Journal Of Physics-Condensed Matter*, 17(49):S4075–S4090, 2005.

[86] Christian Sendner, Dominik Horinek, Lyderic Bocquet, and Roland R. Netz. Interfacial water at hydrophobic and hydrophilic surfaces: Slip, viscosity, and diffusion. *Langmuir*, 25(18):10768–10781, September 2009.

[87] Berend Smit, Sami Karaborni, and J. Ilja Siepmann. Computer simulations of vapor–liquid phase equilibria of n-alkanes. *The Journal of Chemical Physics*, 102(5):2126–2140, 1995.

[88] V. P. Sokhan, D. Nicholson, and N. Quirke. Fluid flow in nanopores: An examination of hydrodynamic boundary conditions. *Journal Of Chemical Physics*, 115(8):3878–3887, 2001.

[89] V. P. Sokhan, D. Nicholson, and N. Quirke. Fluid flow in nanopores: Accurate boundary conditions for carbon nanotubes. *Journal Of Chemical Physics*, 117(18):8531–8539, 2002.

[90] W. Sparreboom, A. van den Berg, and J. C. T. Eijkel. Principles and applications of nanofluidic transport. *Nat Nano*, 4(11):713–720, November 2009.

[91] Haixin Sui, Bong-Gyoon Han, John K. Lee, Peter Walian, and Bing K. Jap. Structural basis of water-specific transport through the aqp1 water channel. *Nature*, 414(6866):872–878, December 2001.

[92] S. Supple and N. Quirke. Rapid imbibition of fluids in carbon nanotubes. *Phys. Rev. Lett.*, 90(21):214501–, May 2003.

[93] S. Supple and N. Quirke. Molecular dynamics of transient oil flows in nanopores i: Imbibition speeds for single wall carbon nanotubes. *The Journal of Chemical Physics*, 121(17):8571–8579, 2004.

[94] S. Supple and N. Quirke. Molecular dynamics of transient oil flows in nanopores. ii. density profiles and molecular structure for decane in carbon nanotubes. *The Journal of Chemical Physics*, 122(10):104706, 2005.

[95] Sarah L. Tao and Tejal A. Desai. Microfabricated drug delivery systems: from particles to pores. *Advanced Drug Delivery Reviews*, 55(3):315–328, February 2003.

[96] JonasO. Tegenfeldt, Christelle Prinz, Han Cao, RichardL. Huang, RobertH. Austin, StephenY. Chou, EdwardC. Cox, and JamesC. Sturm. Micro- and nanofluidics for dna analysis. *Analytical and Bioanalytical Chemistry*, 378(7):1678–1692, 2004-04-17.

[97] J. Tersoff. New empirical model for the structural properties of silicon. *Phys. Rev. Lett.*, 56(6):632–, February 1986.

[98] J. A. Thomas and A. J. H. McGaughey. Reassessing fast water transport through carbon nanotubes. *Nano Letters*, 8(9):2788–2793, 2008.

[99] John A. Thomas and Alan J. H. McGaughey. Water flow in carbon nanotubes: Transition to subcontinuum transport. *Phys. Rev. Lett.*, 102(18):184502–, May 2009.

[100] John A. Thomas, Alan J.H. McGaughey, and Ottoleo Kuter-Arnebeck. Pressure-driven water flow through carbon nanotubes: Insights from molecular dynamics simulation. *International Journal of Thermal Sciences*, 49(2):281–289, February 2010.

[101] Erik T. Thostenson, Zhifeng Ren, and Tsu-Wei Chou. Advances in the science and technology of carbon nanotubes and their composites: a review. *Composites Science and Technology*, 61(13):1899–1912, October 2001.

[102] B. W. H. van Beest, G. J. Kramer, and R. A. van Santen. Force fields for silicas and aluminophosphates based on ab initio calculations. *Phys. Rev. Lett.*, 64(16):1955–, April 1990.

[103] David Van Der Spoel, Erik Lindahl, Berk Hess, Gerrit Groenhof, Alan E. Mark, and Herman J. C. Berendsen. Gromacs: Fast, flexible, and free. *Journal of Computational Chemistry*, 26(16):1701–1718, 2005.

[104] C. Vega, J. L. F. Abascal, M. M. Conde, and J. L. Aragones. What ice can teach us about water interactions: a critical comparison of the performance of different water models. *Faraday Discuss.*, 141:251–276, 2009.

[105] Henk Verweij, Melissa C. Schillo, and Ju Li. Fast mass transport through carbon nanotube membranes. *Small*, 3(12):1996–2004, 2007.

[106] Olga I. Vinogradova. Drainage of a thin liquid film confined between hydrophobic surfaces. *Langmuir*, 11(6):2213–2220, June 1995.

[107] Olga I. Vinogradova and Aleksey V. Belyaev. Wetting, roughness and hydrodynamic slip, 2010.

[108] Edward W. Washburn. The dynamics of capillary flow. *Phys. Rev.*, 17(3):273–, March 1921.

[109] T. Werder, J. H. Walther, R. L. Jaffe, T. Halicioglu, and P. Koumoutsakos. On the water-carbon interaction for use in molecular dynamics simulations of graphite and carbon nanotubes. *The Journal of Physical Chemistry B*, 107(6):1345–1352, February 2003.

[110] Max Whitby, Laurent Cagnon, Maya Thanou, and Nick Quirke. Enhanced fluid flow through nanoscale carbon pipes. *Nano Letters*, 8(9):2632–2637, 2008. PMID: 18680352.

[111] Mark L. Zeidel, Soren Nielsen, Barbara L. Smith, Suresh V. Ambudkar, Arvid B. Maunsbach, and Peter Agre. Ultrastructure, pharmacologic inhibition, and transport selectivity of aquaporin chip in proteoliposomes. *Biochemistry*, 33(6):1606–1615, February 1994.

[112] Yingxi Zhu and Steve Granick. Reassessment of solidification in fluids confined between mica sheets. *Langmuir*, 19(20):8148–8151, September 2003.

Within the scope of this thesis, a theoretical study of liquid flow in graphitic nanopores was performed. More precisely, a combination of numerical simulations and analytic approach was used to establish the special properties of carbon nanotubes for fluid transport: Molecular dynamics flow simulations of different liquids in carbon nanotubes exhibited flow velocities that are 1-3 orders of magnitude higher than predicted from the continuum hydrodynamics framework and the no-slip boundary condition. These results support previous experiments performed by several groups reporting exceptionally high flow rates for water in carbon nanotube membranes. The reason for this important flow enhancement with respect to the expectation was so far unclear.

In this work, a careful investigation of the water/graphite friction coefficient which we identified as the crucial parameter for fast liquid transport in the considered systems, was carried out. In simulations, the friction coefficient was found to be very sensitive to wall curvature: friction is independent of confinement for water between flat graphene walls with zero curvature, while it increases with increasing negative curvature (water at the outside of the tube), and it decreases with increasing positive curvature (water inside the tube), eventually leading to quasi frictionless flow for water in a single file configuration in the smallest tubes. A similar behavior was moreover found with several other liquids, such as alcohol, alcane and OMCTS. Furthermore, a theoretical approximate expression for the friction coefficient is presented which predicts qualitatively and semi-quantitatively its curvature dependent behavior. Moreover, a deeper analysis of the simulations according to the proposed theoretical description shed light on the physical mechanisms at the origin of the ultra low liquid/solid friction in carbon nanotubes. In fine, it is due to their perfectly ordered molecular structure and their atomically smooth surface that carbon nanotubes are quasi-perfect liquid conductors compared to other membrane pores like, for example, nanochannels in amorphous silica.

The newly gained understanding constitutes an important validation that carbon nanotubes operate as fast transporters of various liquids which makes them a promising option for different applications like energy conversion or filtration on the molecular level.

keywords: nanofluidics, slippage, liquid/solid friction coefficient, carbon nanotube, molecular dynamics simulation